The Messenger

No. 158 – December 2014

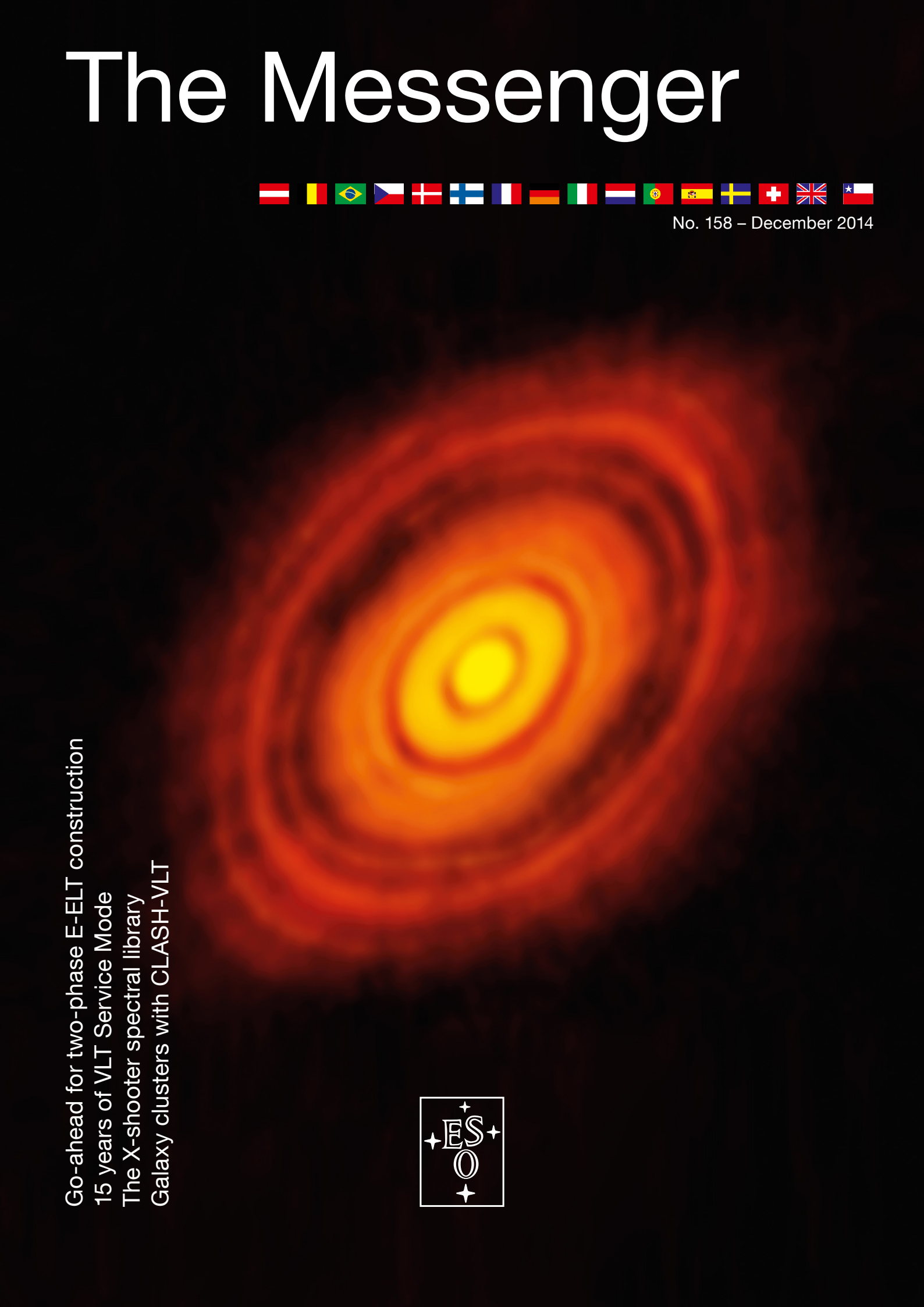

Go-ahead for two-phase E-ELT construction
15 years of VLT Service Mode
The X-shooter spectral library
Galaxy clusters with CLASH-VLT

Signing of ESO–Poland Accession Agreement

An agreement was signed by Professor Lena Kolarska-Bobińska, the Polish Minister of Science and Higher Education, and the ESO Director General Tim de Zeeuw in Warsaw on 28 October 2014 that will lead to the country joining ESO. The signing of the agreement followed its unanimous approval by the ESO Council during an extraordinary meeting on 8 October 2014. Poland will be welcomed as a new Member State, following subsequent ratification of the accession agreement by the Polish Parliament. Tim de Zeeuw's speech at this ceremony is reproduced below.

Figure 1. The signing ceremony of Polish Accession to ESO in Warsaw: Professor Lena Kolarska-Bobińska, the Polish Minister of Science and Higher Education, seated centre, with the ESO Director General Tim de Zeeuw (left) and the Undersecretary of State in the Ministry of Science and Higher Education, Włodzisław Duch (right).

Welcome Speech

Tim de Zeeuw, ESO Director General

Dear Minister Kolarska-Bobińska, Undersecretary Duch, colleagues and friends,

It is a distinct pleasure to say a few words on this important occasion.

Astronomy has a long and proud tradition in Poland, going back to Wojciech z Brudzewa and his most famous pupil Mikołaj Kopernik, who proposed that the Sun and not the Earth is at the centre of our Solar System, and to Jan Heweliusz who is considered to be the father of lunar topography. Wilhelmina Iwanowska and Stefan Piotrowski resurrected Polish astronomy after the Second World War, and guided it into the modern era. This brought forward many outstanding scientists, including Bohdan Paczyński, a brilliant theorist, who also almost single-handedly created the field of microlensing. Paczyński inspired the world-famous Optical Gravitational Lensing Experiment (OGLE), which is led by Andrzej Udalski, and has involved observations at ESO.

With the historical changes in Europe that began in the 1980s, it was natural that Polish scientists would want to strengthen their relationship with colleagues in western Europe and that this collaboration would indeed be warmly welcomed in the West. It was clear that this could, at some stage, also include Polish membership of ESO, Europe's organisation for astronomy that has now grown to be the leading organisation for astronomical research in the world.

The first contacts between ESO and Poland date back to the early 1990s, but the idea clearly needed time to mature. In 2003, ESO put up a major exhibition in Toruń on the occasion of the 80th anniversary of the Polish Astronomical Society. More formal contacts at government level were established in 2006, but it was not until late 2011 that the process, leading to today's signing of the Accession Agreement, really took off.

Many people have contributed during this phase, and I wish to acknowledge some of them today: Kazimierz Stępień, Marek Sarna, Andrzej Udalski, as well as Krzysztof Czart and Agata Karska. A very special thank you is in order for Jacek Gierliński who has guided the process through the official channels with tremendous dedication and skill, working closely with Laura Comendador Frutos and Patrick Geeraert on the ESO side.

For Poland, ESO membership opens new opportunities, not only for the scientists and engineers but also for industry. Polish astronomers will gain access to the world-leading Very Large Telescope on Paranal and the Atacama Large Millimeter/submillimeter Array (ALMA) Observatory at Chajnantor, both in northern Chile. The addition of the Extremely Large Telescope on Armazones will be a further tremendous step forward and Polish industry will be part of the construction effort.

The field of astronomy with its wealth of potential discoveries about the Universe in which we live serves as a source of fascination and inspiration for society at large. ESO Membership will further highlight the importance of science and technology, and help to attract young people to the physical sciences, crucial for the future of our civilisation.

For ESO, the membership of Poland is equally important and, indeed, historic. Poland brings a strong astronomical community, which will add to the expertise across the ESO Member States, for example in time-series astronomy.

All the major countries in Europe which are strongly engaged in astronomy are now members of ESO. At ESO they can meet and interact, can use the observing facilities and jointly develop new ideas and projects, decisively shaping the future of our science.

Welcome Poland!

Constructing the E-ELT

Tim de Zeeuw[1]
Roberto Tamai[1]
Jochen Liske[1]

[1] ESO

At its meeting on 3 and 4 December 2014, the ESO Council gave the green light for the construction of the E-ELT in two phases and authorised spending of up to 1012.5 million euros on Phase 1, which will provide a fully working 39-metre telescope with a suite of powerful instruments. It will allow the initial characterisation of earth-mass exoplanets, studies of the resolved stellar populations in nearby galaxies as well as ultrasensitive observations of the deep Universe. This article provides the context for this momentous decision and describes the two-phase approach.

Background

With its 39-metre primary mirror, the European Extremely Large Telescope (E-ELT) will be the largest optical and infrared telescope in the world. By opening up observational parameter space in several decisive ways, the E-ELT is set to revolutionise many areas of astrophysics and technology. Its timely construction is therefore of the highest priority for ground-based astronomy worldwide.

To set the scene for the recent Council decision, it is useful to cast our minds back to 2012. Following the detailed design phase and successful technical and financial reviews, ESO Council approved the E-ELT construction as a Supplementary Programme in December 2012. This approval was based on a financial model in which the construction cost of the E-ELT is funded by: (i) ESO's current income; (ii) a 2% year-on-year increase of the Member States' annual contributions, on top of normal indexation, for a period of ten years; (iii) a one-time extra contribution by the Member States which can be paid in up to ten annual instalments; and (iv) extra income resulting from Brazil's accession to ESO.

However, since not all Member States were in a position to commit in December 2012, and since Brazil had not yet completed its accession at that time, the approval was subject to the condition that contracts worth more than 2 million euros could not be awarded until 90% of the E-ELT's cost-to-completion of 1083 million euros (in 2012 prices) had been committed. The only exception to this rule was the work required for the preparation of the site. By June 2014, all 14 Member States had joined the E-ELT resulting in 71% of the E-ELT's cost-to-completion being in hand. Poland's accession as an additional Member State to ESO will raise this fraction to 78% in the course of 2015.

Concurrently with the project's approval in December 2012, ESO Council and the Executive began to explore potential options open to ESO in case the ratification of the Brazilian Accession Agreement would not be completed in the foreseen timescale. Fortunately, the ratification process has since progressed well, but at present is not yet completed. The ESO file has passed three commissions within the Brazilian Chamber of Deputies, but still needs to pass a fourth commission and a Plenary Session. The file will then go to the Senate, where the procedure is expected to take around six weeks, followed by the Brazilian President's signature.

Considering the progress of the competing giant telescope projects, the needs of the E-ELT instrument consortia, the dwindling overlap with the foreseen operational period of the James Webb Space Telescope (JWST) to be launched in 2018, and the need to maintain the interest of ESO's industrial partners, it became clear by mid-2014 that the ongoing day-by-day delay was posing an increasing risk to the project and to the scientific aspirations of the ESO community. Finding a way to allow the project to move forward, even in the temporary absence of Brazilian funding, while still respecting Council's "90% rule", thus became a matter of some urgency.

Moving forward

After considering several options to resolve this situation, it became clear from consultation with ESO's governing bodies in the first half of 2014, that the eventual solution would have to: (i) preserve the superb scientific capabilities of the E-ELT as much as possible; (ii) preserve the current baseline first-light date of 2024 as much as possible; and (iii) avoid the need for any long-term loans. As a result Council, in June 2014, asked for the development of a two-phase construction plan for the E-ELT, such that the funding needed for Phase 1 does not require the completion of Brazil's ratification of its Accession Agreement or any additional funds from the current Member States. This is achieved by transferring some 106.5 million euros to Phase 2 and by extending the duration of construction by up to two years, unless additional funds can be identified.

This plan was developed in consultation with ESO's governing bodies through a series of meetings that took place from July 2014 onwards. It was formally recommended by the Scientific and Technical Committee in October 2014 and by the Finance Committee in November 2014. Based on these recommendations, the ESO Council approved the two-phase approach and, most importantly, authorised spending up to 1012.5 million euros on Phase 1 during its meeting on 3–4 December 2014. The decision needed ten positive votes. Three of the 14 votes are so-called *ad referendum* votes, which means that they are to be considered as provisionally positive and subject to confirmation by the authorities in these three Member States before the next Council meeting.

Council remains committed to building the entire E-ELT as originally designed and scheduled. In particular, the two-phase approach only involves the potential deferral of some items but no design changes (with the exception of the telescope's pre-focal stations, see below). Furthermore, future approval of Phase 2 is only contingent on the availability of funding. Individual Phase 2 items will be reinstated (and/or first light brought back to 2024) as soon as the required additional funding becomes available. In particular, as soon as Brazil completes its ratification process, Phase 2 will be reinstated in its entirety. Finally, it is extremely important to note that the procurement schedules of the baseline construction

plan and of the two-phase plan only start to diverge in 2017. This is the earliest time at which any Phase 2 item would have to be deferred. If Brazil completes its ratification process before this time then the two-phase plan is identical to the original baseline. In the unlikely event of Brazil joining later, some delays and extra cost will be accrued, but the full E-ELT will still be built. Effectively, the two-phase plan therefore simply allows ESO to move ahead with the construction, while awaiting the completion of the Brazilian ratification process.

The two-phase approach to E-ELT construction

There are few technical options to reduce the overall cost of the 39-metre E-ELT, as the current design is the result of the delta phase B study, that had, as its main goal, the identification and implementation of such options for the original 42-metre phase B design. A detailed analysis of the baseline plan has been carried out to identify which components are indispensable and lead to first light with a working and competitive telescope (Phase 1), and which components can be moved to Phase 2 to await the availability of additional funds. For this exercise to result in a financially viable Phase 1, a target of ~ 110 million euros had been set for the total scope of the components to be moved to Phase 2. The main items that were identified for transfer to Phase 2, and thus for potential deferral into the future, include infrastructure and telescope components, as well as an adaptive optics module. These are briefly described here.

The baseline plan includes power conditioning to stabilise its quality so that power cuts or surges affect operations as little as possible. Deferring this procurement could somewhat increase the technical downtime, but would not affect the ability to do science or the date of first light. The Chilean government has assisted in enabling the construction of a grid connection to the Paranal–Armazones area. Work started in mid-2014 and will be completed in 2018. It is possible that the quality of the resulting grid power will be sufficient for smooth operations, so that this procurement could be reduced in cost, or might not be necessary at all.

The E-ELT's primary mirror (M1) is composed of six identical sectors of 133 segments each. The 133 segments are different to each other both in shape and optical prescription. The baseline plan foresees the procurement of a seventh sector strictly needed to guarantee the replacement of the segments in a turnaround plan to maintain a constant reflectivity and micro-roughness level. This is achieved by replacing two segments every day (the worst ones in terms of both reflectivity and scattering/micro-roughness) with two mirrors from the (freshly coated) seventh sector. In this way the entire M1 mirror is totally refreshed in approximately 18 months.

It is, however, possible to postpone the procurement of the seventh sector and, for the first few years of operation, either wash the segments *in situ* or periodically leave several segments unfilled for short periods. Paranal experience shows that a proper washing of aluminium-coated mirrors recovers almost 100 % of the condition of a freshly coated mirror. Alternatively, and still without procuring the seventh sector, the segments could be recoated rather than washed, accepting a few missing segments in M1 at any time. The result would have a minor scientific impact, but a higher maintenance workload, provided the most demanding extreme adaptive optics observations are scheduled for times when the mirror is fully populated. Transfer of the seventh sector to Phase 2 also enables the M1 coating plant to be descoped (one plant instead of two).

The procurement of some of the inner rings of segments of M1 has emerged as one of the most important transfers. Analysis has demonstrated that the maximum number of rings that can be moved to Phase 2 is five, representing 210 M1 segments. This will obviously have an impact on collecting area (reduced by 26 %), but the 39-metre annular aperture will preserve the original spatial resolution (loss of ~ 25 % at low–mid spatial frequencies while leaving the higher spatial frequencies almost untouched). The loss in sensitivity can, in most cases, be recovered by increasing the integration time. Removing the sixth inner ring was considered but the risk that this would negatively impact the wavefront control of the telescope was deemed too high.

Since the procurement of M1 is currently on the critical path of the E-ELT, reducing the number of segments in Phase 1 will generate some schedule margin for the project. Fewer rings will also reduce the overall workload for M1 segment procurement and installation, thereby accelerating the Assembly, Integration and Verification (AIV) sequence for the telescope. However, the interfaces of the main support structure will still be installed and aligned, as would be required for the proper installation of the segments, because the mirror cell loading affects the interfaces. Moreover, this will minimise the downtime required for the future installation of the deferred segments. The telescope balance will be maintained by installing dummy masses at the missing M1 interface points.

The instrument optics will be designed for the full M1 aperture. The pupil stop which masks the unfilled area (and which is present in all infrared instruments) will match the partially populated primary and will need to be exchanged for the smaller central obstruction when the full primary is installed.

The E-ELT instrumentation roadmap foresees a total of seven first-generation instruments. Originally, the two first-light instruments, the Multi-AO Imaging Camera for Deep Observations (MICADO) and the single field visible and near-infrared integral field spectrograph HARMONI, including their associated adaptive optics (AO) systems (the multi-conjugate AO [MCAO] module MAORY and a laser tomography AO [LTAO] module, respectively, together with six laser guide stars), as well as two additional instruments, were to be supported from the construction budget. However, the non-indexation of ESO's budget in 2013 led to the removal of one of the latter two instruments from the E-ELT construction budget to the instrumentation development line in the E-ELT operations budget. The current baseline construction plan thus includes three instruments and their associated AO systems, where the Mid-infrared E-ELT Imager and Spectrometer (METIS) has been identified as the third instrument due to its more advanced

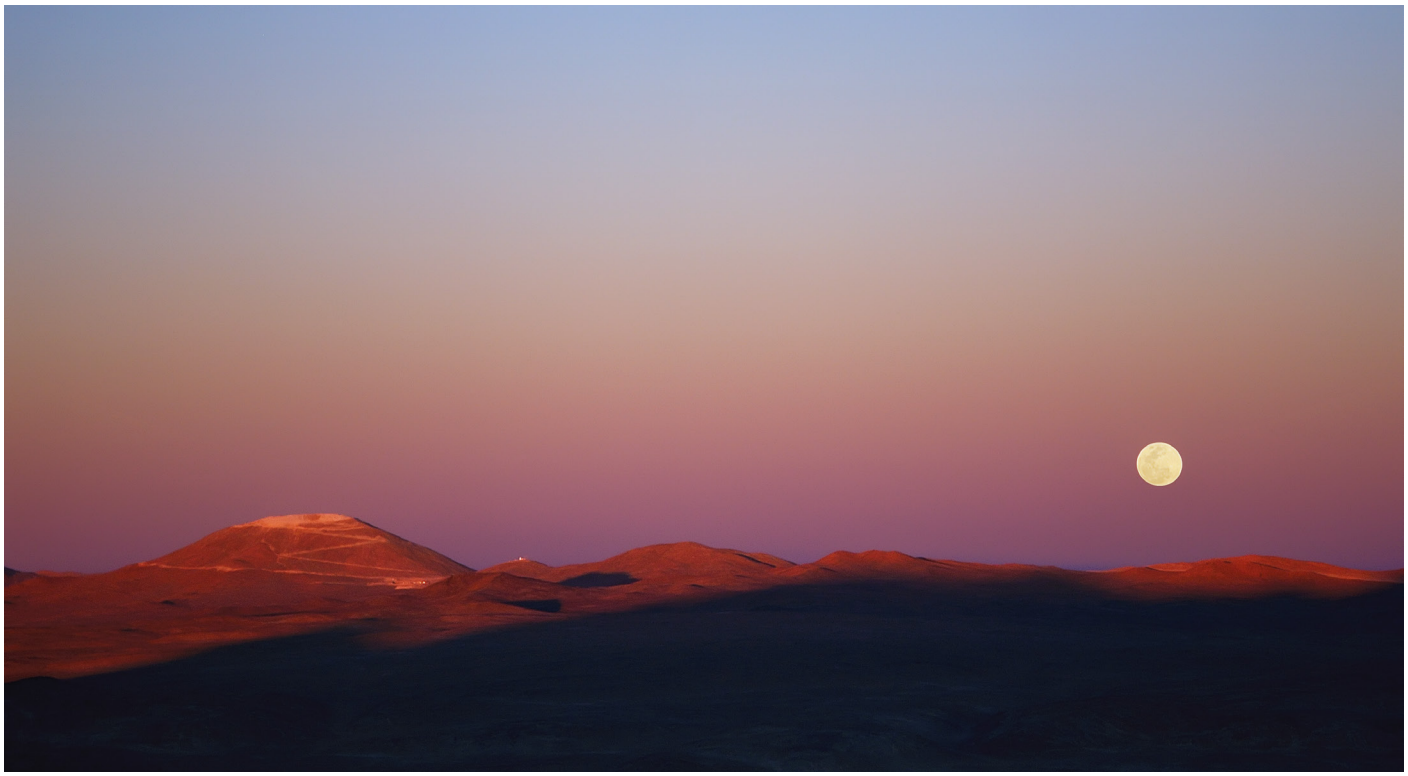

Figure 1. A recent image of the site of the E-ELT on Cerro Armazones, taken from the VLT platform on Cerro Paranal.

technical readiness compared to the other two potential candidates (a multi-object spectrograph [MOS] and a high-resolution spectrograph [HIRES]), each of which requires a competitive Phase A study to be carried out first). Deferring any of these three instruments or some of the AO capabilities would obviously result in a loss of science.

Nevertheless, in order to reach the goal for the total scope of the items to be moved to Phase 2, some transfer in the area of instrumentation was necessary, and so a very difficult decision had to be made. After considering several options it was decided to move two of the six powerful lasers and the LTAO module to Phase 2. The deferral of the LTAO module would severely affect the sky coverage of both HARMONI and METIS, leaving both instruments with single conjugate AO (SCAO) only, but keeping all three instruments as well as MAORY in Phase 1 was deemed important because it maximises the support of the instrument building community and secures the investment already put in place by many of the Member States. In addition, it is estimated that the LTAO system needs only seven years to implement, whereas METIS needs nine. There is therefore more time to secure the Phase 2 funding needed for LTAO and still be ready at first light. LTAO is the highest priority item in Phase 2 and will be implemented as soon as the required funding has been identified. Importantly though, Phase 1 does include funding for the preliminary design of the LTAO system, as well as for MOS and HIRES.

Each of the E-ELT's two Nasmyth platforms is to be equipped with a pre-focal station (PFS). Since all three Phase 1 instruments can be attached to a single PFS, the second PFS can be moved to Phase 2. Its deferral would have no impact on science while only three instruments are in use. In addition, the first PFS can be descoped by utilising a simplified adapter and the existing planned wavefront sensing systems of the instrumentation and the AO systems. This approach requires an evolution of the interface between the telescope and the instruments, requiring a closer collaboration between the activities of the telescope and instrument design teams. The simplified adapter will not provide ground layer AO (GLAO) capability but will be compatible with SCAO, LTAO and MCAO. The design of the descoped PFS will take into consideration a possible future retrofit which would restore the original PFS capability. This is the only design change required by the two-phase approach.

First light of Phase 1

The items described above amount to a total transfer of 106.5 million euros to Phase 2. The funds so far committed to the E-ELT (including the funds expected from Poland's accession to ESO in 2015) therefore represent 86 % of the cost-to-completion of Phase 1 of 997.5 million euros (in 2014 prices). This still leaves a gap of 4 % to meet ESO Council's 90 % rule. Several options are available to close this gap. However, at this time the

Figure 2. The members of the ESO Council and senior ESO staff photographed in the Council Room at ESO Headquarters during the meeting at which the decision to approve the two-phase construction of the E-ELT was made on 3 December 2014.

only safe planning option is to consider a delay of the date of first light for Phase 1 by about two years. The postponement of the start of operations by approximately two years would allow adding much of the E-ELT operations funding, foreseen in the baseline plan for this period, to the Phase 1 construction funding, and would help to create a smoother cash-flow profile. On the other hand, it would also slightly increase the cost of Phase 1. If indeed required, the extension of the construction period would be accomplished by re-scheduling some procurement actions. The contracts themselves would not be stretched and all currently existing contracts will continue as planned. This avoids the need to re-design any subsystem and makes it possible to revert to the original timeline, or close to it, as soon as Brazil completes its ratification process or another new Member State joins.

The main impact of a two-year delay in first light and the start of regular operations would be on scientific competitiveness, especially considering that the first-light date in the baseline plan has already been tracking the delays in the start of construction for some time. The delay would increase the risk of one of the competing projects arriving on sky significantly earlier than the E-ELT and would reduce the chances of any overlap between the operations of the E-ELT and JWST. This would be exacerbated by the potential slower pacing of instrument arrivals.

Conclusions

ESO's Member States are fully committed to building the E-ELT while keeping the La Silla Paranal Observatory as well as the Atacama Large Millimeter/submillimeter Array (ALMA) at the forefront of astronomy. With its decision to adopt the two-phase approach to the construction of the E-ELT, and to authorise spending on Phase 1 for a cost-to-completion of 1012.5 million euros, Council has given the green light to move full-steam ahead with the construction of the world-leading E-ELT on a competitive timescale. This momentous decision marks the end of a period of uncertainty after the programme was formally approved in late 2012 but not all the required funding had been committed.

The Phase 1 E-ELT as described above will be a very powerful science machine, integrated into the Paranal system. It will enable the initial characterisation of earth-mass rocky exoplanets, allow the study of resolved stellar populations in nearby galaxies out to the Virgo Cluster and provide unprecedented sensitivity for studies of the deep Universe. Phase 2 is, however, absolutely required to meet the longer-term scientific aspirations of the community.

It is important to realise that Council's decision does not mean that only the Phase 1 E-ELT will be built. The construction will proceed according to the baseline schedule, aiming for first light in 2024, until at least early 2017. If Brazil has completed the ratification of its Accession Agreement by that time, then the two-phase approach (and this article) will have become entirely irrelevant, except for having prevented further delays.

The signal sent by this decision to the worldwide scientific community, to the E-ELT instrument teams and to industry in the ESO Member States is thus entirely positive: the E-ELT is now becoming a reality.

Acknowledgments

It is a pleasure to thank the members of the Council-appointed E-ELT Working Group and the entire E-ELT team inside ESO for their support in developing the two-phase plan.

ESO/J. Girard

View of the Paranal Observatory, looking south from the VISTA platform. The Large and Small Magellanic Clouds are clearly visible and the laser guide star is being projected from Unit Telescope 4.

Fifteen Years of Service Mode Operations: Closing the Loop with the Community

Francesca Primas[1]
Lowell Tacconi-Garman[1]
Stéphane Marteau[1]
Vincenzo Mainieri[1]
Marina Rejkuba[1]
Sangeeta Mysore[1]
Christophe Dumas[1]
Andreas Kaufer[1]
Ferdinando Patat[1]
Michael Sterzik[1]

[1] ESO

The first Service Mode (SM) observations with the VLT were made by ISAAC in April 1999. Since then, new instruments have become operational and first generation ones replaced, filling the 12 VLT foci and feeding the VLT Interferometer and its four Auxiliary Telescopes. Efficiently operating such a broad range of instruments, installed and available every night of each year, on four 8-metre telescopes offers many challenges. Although it may appear that little has changed since 1999, the underlying VLT operational model has evolved in order to accommodate different requirements from the user community and features of new instruments. As ESO and its Member States approach routine operations with ALMA, and at the same time prepare for the next challenge, the construction of the E-ELT, it seems timely to take a closer look at what SM has brought to the scientific arena, both in terms of science data and support. Did it fulfil its original goal, if so, how well, and what are the lessons learned? A careful analysis of statistics and trends in Phase 1 and Phase 2 are now being conducted in the DOME (Dashboard for Operational Metrics at ESO) project. We summarise the main findings, concentrating on the handling of Service Mode.

Introduction

When ESO's Very Large Telescope (VLT) opened its first dome at the beginning of Period 63 (P63; c.f., Table 1 for a summary of the milestones), it was only the second observatory in the world offering 8-metre-class telescope(s). It was also the first ground-based facility offered to the scientific community at large with both classical (also known as Visitor Mode [VM]) and queue observing. The latter, known as Service Mode observing in ESO terminology, was considered to be the most promising way to ensure the observing flexibility necessary to execute the most demanding scientific programmes under the required, usually very well-defined, conditions.

The official reference to the ESO VLT/Interferometer (VLT/I) operational model is the VLT/VLTI Science Operations document[1] approved by ESO Council (most recent update from 2004). The document touches upon all main areas of the ESO data flow system, from proposal submission, to execution and archiving of the data. It sets guidelines for the SM/VM ratio (at least 50 % in SM in order to achieve an optimal scientific return), describes what types of observing times exist (normal/open time, fraction of time reserved for Large Programmes, Guaranteed Time Observations [GTO], Director's Discretionary Time [DDT], Target of Opportunity [ToO]) and the Service Mode rank classes of the scheduled programmes (A, B and C) as a way to implement the scientific ranking and evaluations delivered by the Observing Programmes Committee [OPC]). Within the current framework, A class runs are the highest priority programmes for which ESO has committed to make all possible efforts to complete (within the requested observing Period or by granting them carryover status to the next useful visibility Period); B and C class runs however are executed only within the requested observing semester. The document mentions the set-up and maintenance of calibration plans, both for scientific and instrument health-checking purposes, as well as how the obtained data will then be distributed to the Principal Investigators (PIs) and later to the community at large. More details can be found in a number of SPIE and *Messenger* articles (e.g., Quinn et al., 2000; Silva et al., 2001; Comerón et al., 2003).

Table 1. Summary of VLT/I milestones.

Period (Start)	Milestone
P63 (April 1999)	VLT UT1 starts operations
P64 (October 1999)	VLT UT2 starts operations
P67 (April 2001)	VLT UT3 and UT4 start operations
P72 (October 2003)	VLTI starts operations

The "front-end" of the ESO data flow system begins when the period-based Calls for Proposals is issued and members of the user community submit their observing proposals. This, together with the scientific evaluation and ranking of the proposals by the OPC, defines the Phase 1 process, which formally ends with the delivery of the schedule for all available telescopes (c.f., Patat & Hussain [2013] for a review of this process). As soon as the time allocations are announced to the community, the Phase 2 process can start, i.e., the preparation of the SM observations by the successful PIs (or their delegates), followed by the verification and optimisation of each programme's observing strategy by the User Support Department (USD). Observing queues are then prepared per instrument and made available to the Observatory.

Night-time observations are carried out by the staff at the Observatory, following a complex ranking optimisation which takes into account the scientific priority set by the OPC, as well as the observability of the programme and the relative priorities within each programme set by the users (c.f., Bierwirth et al. [2010] for a description). If problems arise, the affected parties are informed via a ticketing system (directed to engineers if the problem is of a technical/instrumental nature, support astronomers when it concerns the science). As data are taken, these are transferred to ESO Garching and become available to the PI (and his/her delegate) after they reach the Science Archive. Smooth operations are guaranteed by real-time health checks on the instruments and careful monitoring of their performance (Hanuschik & Silva, 2002).

Despite being new to the SM concept of carrying out astronomical observations (except for the short period during which Service Mode was deployed at the New Technology Telescope [NTT] for trial purposes), the ESO community clearly adapted very quickly to this new mode. Figure 1 shows the relative demand (upper) and time allocations for VM and SM since the start of VLT operations in Period 63. The requested SM fraction consistently exceeds 50 %.

Figure 2 shows the global (i.e., SM and VM combined) oversubscription rates for

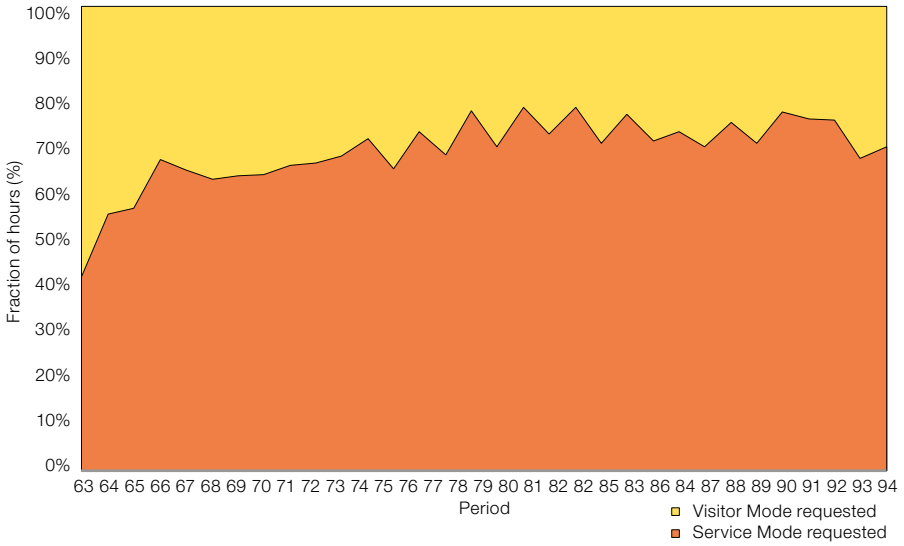

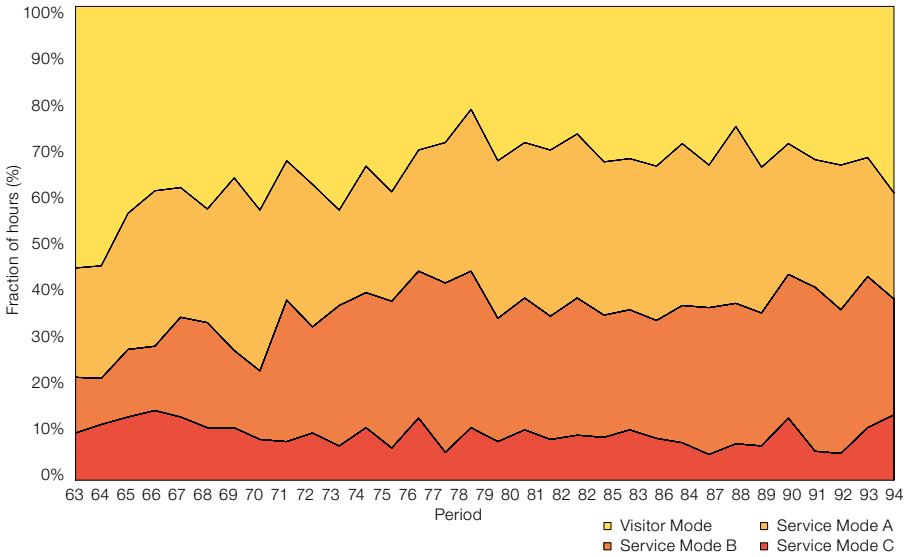

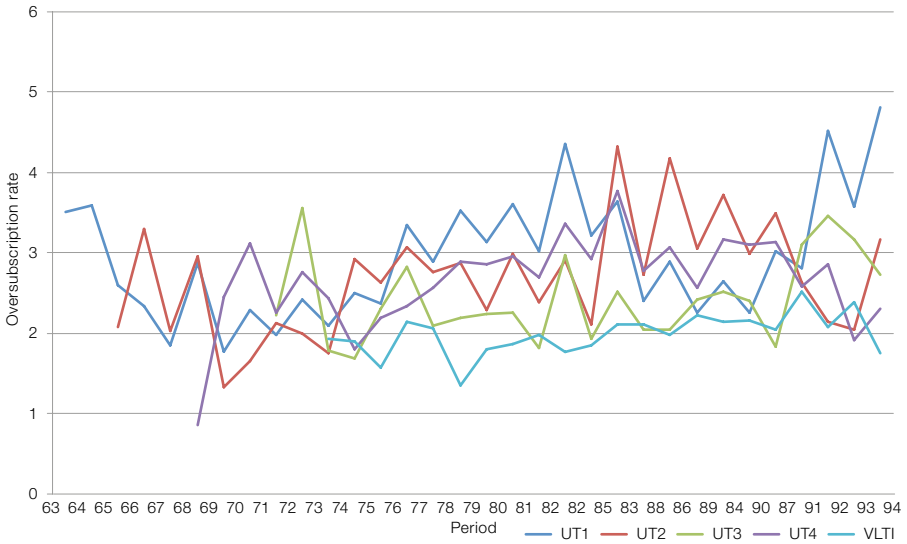

Figure 1. Upper: Relative percentage of the Service *vs*. Visitor Mode hours requested on all VLT/VLTI telescopes for each observing Period. Lower: Percentage of time allocated on all telescopes of the VLT/VLTI over the same time span. The Service Mode area is further split into rank class A, B and C allocations.

each Unit Telescope (UT) and for the VLT Interferometer. These rates are obtained by normalising the time requests to the time allocations. However, since we oversubscribe the time allocations in SM by ~ 10 % in order to ensure short-term scheduling flexibility, the true oversubscription rates would actually end up slightly higher. Moreover, if split between SM and VM, oversubscription rates tend to be slightly larger for Service Mode.

1999–2014: A steady evolution

Despite the fact that the backbone infrastructure of the VLT operational model has been in place since the start of VLT operations (Quinn et al., 2000), operational complexity has increased as new instruments, new operational and instrumental enhancements and new programme types were added. The request for SM (and its consequent allocation) has increased and is now stable at around 70 %, as is evident from Figure 1. The time invested in the Phase 2 verification process of SM observations has proved to be robust, as demonstrated by the very small number of problem reports related to the adequacy of the transmitted Phase 2 material.

The highest level change made to the system was probably the introduction of the User Portal, in November 2007. The goal of this effort was to provide the user community with a system in which account information (username, password, contact information) for all science- and observation-related web-based applications, and standalone software, is unified and can be controlled by the user. This change represented a big challenge, as it required the merging of a number of operational databases into a new one; but the end result makes the user experience with ESO web applications and

Figure 2. Overall (i.e., combining both SM and VM) oversubscription rates by Unit Telescope (UT) and for the VLTI are shown.

other software simpler and more manageable.

From a more observational point of view, the importance of fast follow-up of unexpected astronomical events was fully recognised. These science cases were implemented in the form of the Rapid Response Mode programme type. More recently, longer-term Monitoring of sources (spanning multiple semesters) was enabled through the monitoring programme type. Calibration proposals were also introduced, allowing the design of programmes that deliver products in support of a variety of science goals for the benefit of the entire user community.

The option to request changes with respect to the observations originally proposed in Phase 1 (as far as targets and instrument set-ups are concerned) was better formalised via a web interface to allow for proper tracking and protection of pre-approved targets. More recently, the upgrade of the Night Log Tool allowed users the option to subscribe to a tailored distribution of observing logs for their own programmes. On the operational side, the upgrade of the helpdesk ticketing system gathered all (operations-related) stakeholders under the same system, making the exchange of information easier, faster and more traceable.

Last, but not least, among the changes, the addition of the survey telescopes, the VLT Infrared Survey Telescope for Astronomy (VISTA) and the VLT Survey Telescope (VST), triggered a deep-seated review of the observing tools. The new operational dimension and challenge of carrying out long-term (five-year), massive surveys for which the fulfilment of the observing strategies, although simple, needed to be automated, demanded this change. A new version of the Phase 2 Proposal Preparation tool (known to users as P2PP) and the Observing Tool resulted, introducing the concept of scheduling containers of Observation Blocks (OBs), to better follow time links, concatenations of observations, etc., and a more robust ranking algorithm. The upgrade of the tools was also used to introduce the figure of the delegate into the system. The delegate is the person entrusted by the official programme PI to follow different (or all) phases of the project (Phase 2 and the execution phase and/or data access via the archive interface).

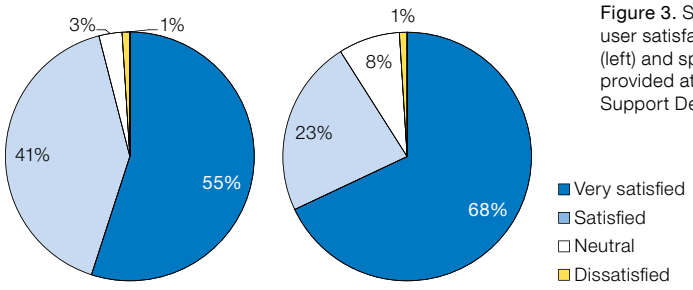

Figure 3. Summary of statistics for user satisfaction with overall support (left) and specific support/advice provided at Phase 2 (right) by the User Support Department.

Overall, the community seems to be appreciative of our system and of the improvements. Feedback from the community is sought regularly via dedicated feedback campaigns and is also received via the Users Committee. Figure 3 summarises the most recent feedback received in March 2014, based on a 31% response rate (out of 502 targeted PIs)[2].

Closing the loop with the community

It is challenging to extract robust metrics from the operational databases, mostly because when the infrastructure was conceived and put in place (almost 20 years ago) operational statistics were obviously not considered as top priority. At that time ESO was operating its only facility, the La Silla Observatory, in Visitor Mode. The re-design and implementation of a completely new data flow system that combined both VM and SM observations was a major challenge in itself, without adding the extra complexity of by-products such as robust operational metrics. Hence, as will be mentioned in the examples below, even the most seemingly obvious number that could be retrieved from a database may be affected by subtle caveats, which we will describe.

This is not to imply that, until now, the operational efficiencies of the Paranal Observatory were never checked, but simply that a limited number of (more technical) benchmarks were used, such as shutter-open time, technical downtime, available science time, etc. All these numbers point to successful management of the Observatory in terms of "time made available to the Community for science observations". Nonetheless, with the occupation of all the VLT foci plus the VLTI, efficiency metrics regarding use of science time were not regularly collected, on account of the much broadened parameter space. At a minimum, having to deal with a very large number of observing programmes, use of three different instruments at the same Unit Telescope, divided into three priority classes (A, B and C) and with an additional division into different programme types, is challenging. At the same time there was an increasing number of requests for a variety of operational statistics used for reporting to various ESO committees. It thus became clear that there was a strong need to determine in a more systematic way how the time available for science observations is used, by identifying a set of robust benchmarks. Therefore the User Support Department has conceived and implemented a system that enables the production of reproducible, reliable queries and their graphical representation, internally called DOME (Dashboard for Operational Metrics at ESO; Primas et al., 2012).

Firstly we tackled the metrics at the front-end of our operational model, Phase 1, but limited consideration to the more operational metrics (pressure, requested *vs.* allocated time, number of unique PIs, etc). A few examples have already been shown (c.f., Figures 1 and 2). More statistics derived from Phase 1 (such as instrument demand, population of constraint space, statistics on users and teams) will be published in a series of dedicated papers.

Granularity is another important aspect of this exercise: most of the metrics can be extracted and displayed per telescope, per instrument, per rank class, per type of programme, etc. For the specific case of Phase 1 metrics, this often comes from simple database queries.

This ease of extraction does not always apply owing to the varied ways in which some information is encapsulated in the database(s). For instance, identifying adaptive optics (AO) assisted observations is complicated by the fact that this information is stored in the databases in different ways for the different instruments with AO capability. Nevertheless, no matter which criteria are used, Service Mode is clearly in high demand, as is evident from Figure 1.

The next, necessarily more complex, area to investigate is Phase 2, i.e., the execution of Service Mode programmes. Here, the two main questions are:

1. How many runs and/or how much scheduled observation time is completed in each rank class?
2. What levels of completion do terminated runs reach?

For A class runs, closer scrutiny of the first question reveals further details about the completion fraction within the first allocated Period, the amount of time needed to complete A class runs and the fraction of A class observations that is carried over into subsequent Periods.

In order to be able to retrieve the corresponding metrics reliably, it was decided to restrict the exercise to VLT/I only. Data from the VST, VISTA and La Silla are thus excluded, mainly because of their current usage (the VST and VISTA are basically survey telescopes; with the exception of a very few ToO cases [see below] La Silla has offered only Visitor Mode since Period 83). Within the VLT/I runs, we looked into the following types of programmes: normal, GTO, DDT, monitoring and calibration. We thus exclude ToO (and Rapid Response Mode) runs and Large Programmes. Exclusion of the former is justified since their completion rates strongly depend on availability of a suitable target for triggered/follow-up observations. This feature distinguishes ToO runs from all other runs, the execution of which depends on the realisation of the requested external conditions, combined with ESO's handling of the observation.

Exclusion of Large Programmes from early consideration is justified since they are a different "species": their completion timescales depend on a variety of factors, some of which are not under ESO's control (e.g., coordinated observations with other facilities and/or dependence on space-based observations). These aspects may affect the progress of a given Large Programme, introducing unavoidable delays that need to be carefully considered when investigating operational efficiencies. In turn, this aspect demands more complex and tailored database queries that can take account of all these different effects.

As is already apparent from the wording of the above two questions, the statistics can be examined in terms of runs (maybe more interesting for the users) and in terms of hours (requested/allocated/executed, possibly more interesting for the Observatory). In the following, we provide both views for some metrics, usually as a function of time (in the form of observing Period, on the *x*-axis).

The primary question is of course about completion fractions. Figure 4 represents the overall completion rates of A, B and C class runs/hours over more than seven years of VLT/I operations. These statistics are provided for Periods P78–P93 because this is the time over which we can guarantee homogeneous treatment of the data. The reason has to do with the insertion of new identifiers (like the run status in P78) so that database queries can extract the same information about these Periods; depending on the type of metrics, other graphs may cover slightly different time ranges. We note however that for the two most recent Periods, P92 and P93, overall completion

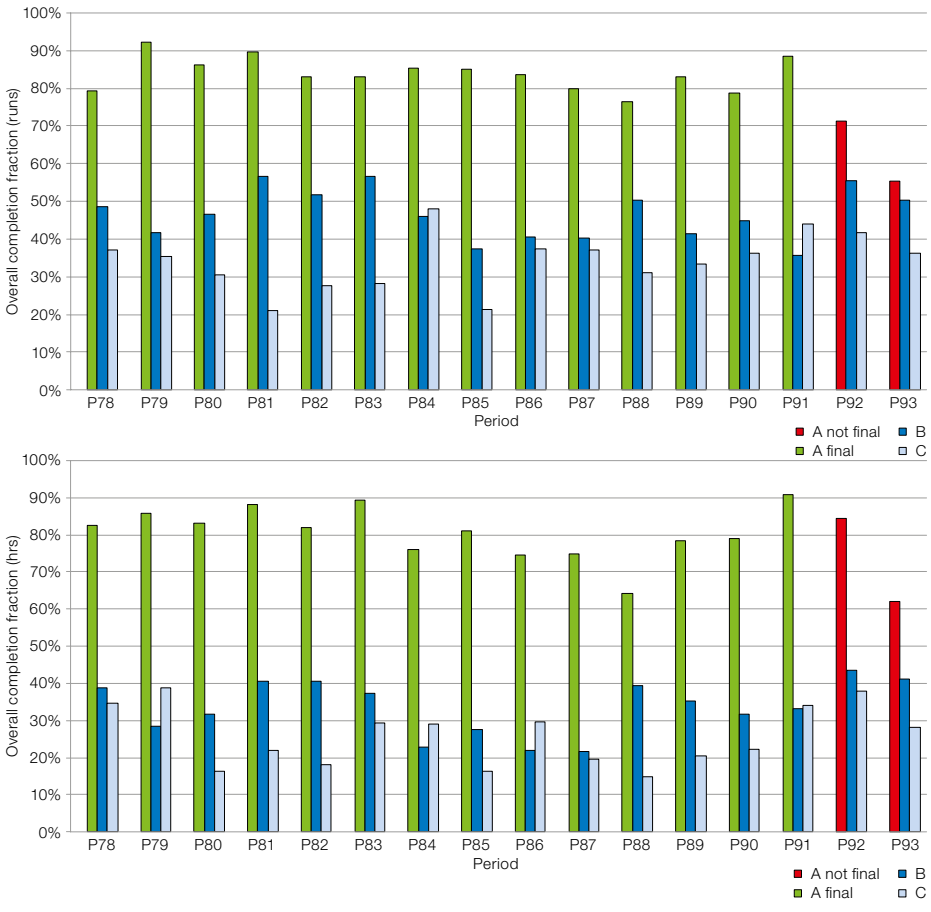

Figure 4. Overall fraction of completed programmes in terms of hours with respect to the total time that was allocated to A, B and C class runs (lower) and the fraction of completed programmes in terms of runs with respect to the total number of runs that were scheduled in A, B and C classes (upper). For the A class category, the fraction completed is irrespective of when the corresponding hours/runs were completed, i.e., hours/runs executed as carryover are included.

statistics are available only for B and C class runs, because some A class runs are still being carried over to future Periods and are not complete. This explains why the corresponding A class bars for P92 and P93 are coloured differently, and marked as "A not final".

Over the past 7–8 years, on average, ~ 80% of all A class runs (and time) could be completed, whereas for B and C class runs this completion rate decreases to 45% and 35% respectively; in terms of time, 34% and 25% of B and C class proposals could be completed, respectively. Of the ~ 20% of A class runs terminated, approximately half reached a ≥ 50% completion fraction. There seems to be no correlation between the terminated A class runs and the requested conditions (i.e., the terminated runs are not among the most demanding ones in terms of seeing/transparency). We note that among the terminated A class runs, there are some approved Director's Discretionary Time programmes, that sometimes have higher chances of not being completed on account of the more challenging/pilot study nature of such programmes. In addition, some time-critical programmes, with one or very few visibility windows, are included among the terminated A class runs.

Figure 5 provides one extra dimension, i.e., the time needed to complete A class runs. It is evident that the red sections (the fraction of runs completed within the first period, defined as the Period in which the runs are first scheduled) dominate the height of the bars, followed by the P + 1 section (i.e., what is approved as carryover and remains visible also in the following semester, shown in green).

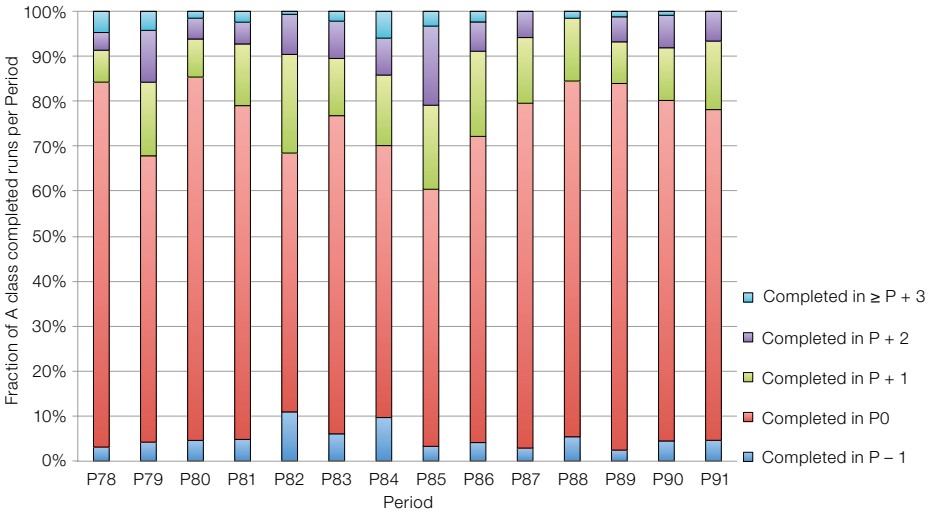

Figure 5. The timeliness of completion of A class runs is shown. This plot refers only to those A class runs that are indeed completed, i.e. the 100% mark on the *y*-axis corresponds to the ~ 80% completion fraction that has emerged from Figure 4. Legend: P0 (red) identifies the first Period in which a given run is scheduled; P – 1 is the preceding Period, during the last months of which some P0 runs may be executed as carryunders; P + 1, P + 2, P + 3, etc. refer to the first, second and third Periods following P0.

The most disappointing finding of this study is the rather low completion rate of B class observations. Irrespective of whether their completion is examined in terms of number of runs or number of hours, the picture remains unsatisfactory. On average, only ~ 30% of the hours allocated to B class runs and ~ 45% of the runs are completed. The difference between the completion rates in [hours] *vs.* [number of runs] indicates that we tend to preferentially complete shorter runs. It is also important to note that B class runs are as demanding – in terms of requested constraints — as A class runs, thus they end up in direct conflict with the higher priority category. Similarly, the distribution of the time allocations per B class run does not differ significantly from that of A class runs.

B class observations thus pay the highest penalty in the current system. This not only causes frustration to individual PIs, but also represents a concern for ESO because currently half of the available SM time is scheduled in the B rank class. For both reasons it is imperative to take a closer look at this rank class. For instance, we can look into the completion fractions of terminated B class runs (c.f., Figure 6).

From Figures 4 (lower panel) and 6 together, we find that, on average, 45% of all B class runs are completed, 45% are started, but terminated at the end of the Period, and 10% do not even get

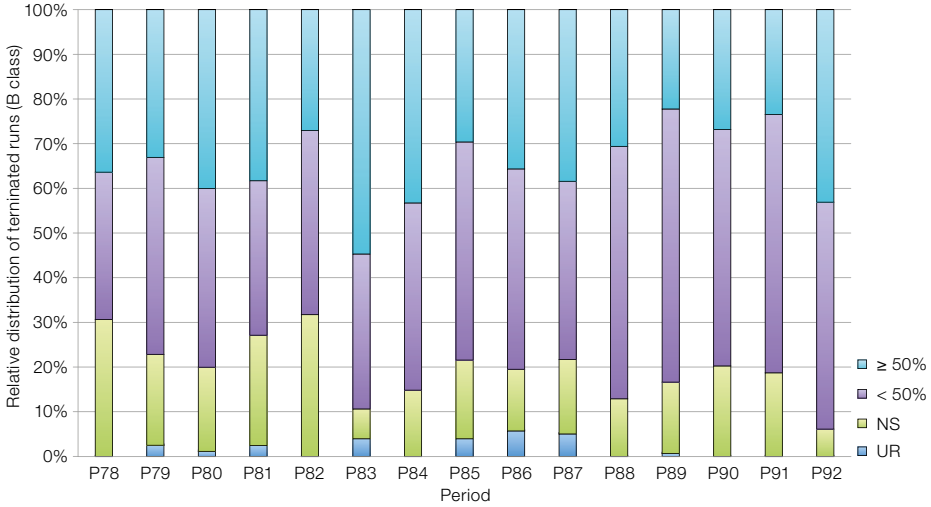

Figure 6. Relative distribution of all terminated B class runs, based on their completion fraction. Legend: NS (runs that were Not Started); ≥ 50% or < 50% refers to the completion fraction at the end of their validity Period. Runs terminated by user request are indicated as "UR".

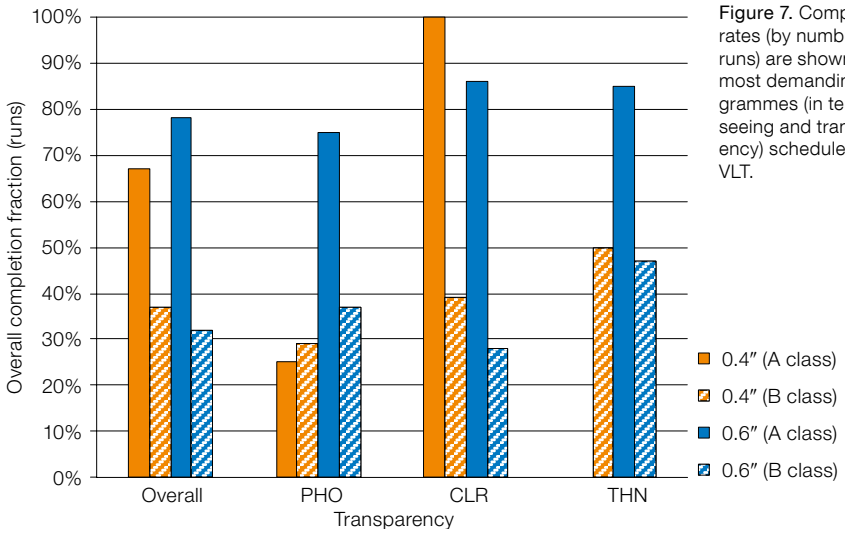

Figure 7. Completion rates (by number of runs) are shown for the most demanding programmes (in terms of seeing and transparency) scheduled at the VLT.

started. From Figure 6 alone, we determine that of the started but terminated runs, 40 % are completed at the level of ≥ 50 %, i.e., 18 % of all B class runs are terminated with completion fractions ≥ 50 %, whereas 27 % are terminated with a completion fraction < 50 %.

Service Mode: The door to very demanding conditions

One of the proclaimed goals for the implementation of a mixed (Visitor + Service Mode) operational model from the very start of VLT/I operations was to enable the successful execution of those programmes requiring very demanding observing conditions. While the definition of demanding observing conditions may include observations of targets widely spread in position, and thus not easy to observe in the few nights of a "classical" VM run, or the need for AO-friendly atmospheric conditions, here we take the seeing constraint as the demanding condition.

By looking at all SM runs that have requested very good seeing conditions (0.4 and 0.6 arcseconds) since P74 (noting, however, that the demand for these conditions has decreased significantly in recent years), we have traced their completion fractions as a whole, according to the requested atmospheric transparency (photometric [PHO], clear [CLR] or thin [THN]) and to their rank class (for this, only A and B rank classes are considered). Figure 7 summarises the results.

Statistics for 0.4-arcsecond seeing runs are very small (37 runs in total, from P74 onwards). After splitting the runs into rank class or transparency bins, the numbers are even smaller. Overall, one finds that approximately half of these runs have been completed, but it should be noted that the large majority of them (27 out of 37) were scheduled in B class (and one even in C class, thus impacting the chance of success from the very start). When runs are split between A and B rank classes, 67 % completion rates for the A class runs and 37 % for the B class runs are found. Within the A class, 25 % of those requesting 0.4 arcseconds + PHO and 100 % of those requesting 0.4 arcseconds + CLR conditions were completed. For the B class runs, the corresponding completion fractions are 29 % and 39 % respectively. Drawing firmer conclusions (e.g., why, under photometric conditions, class B runs achieved slightly higher completions rates than A class runs) requires a closer look at more parameters and/or correlating one parameter against another, e.g., the time of the year for the requested observations and the corresponding weather statistics.

Statistics for 0.6-arcsecond seeing runs are more robust with 559 runs in total. The overall completion fraction does not change much (now at 54 %), but some rates increase when grouping the runs according to their rank class or requested transparency. For A class runs, we reached a completion fraction of 78 %, whereas for the B class runs we remain at around 32 %. Within the A class, we find very satisfactory completion rates of 75 %, 86 % and 85 % for runs requesting PHO/CLR/THN conditions, respectively. For B class runs, as is to be expected, these same rates decrease to 37 %, 28 % and 47 % respectively.

Overall, we find these numbers reassuring because they match the global completion rates for all A and B class runs (c.f., Figure 4 and associated text). In order to determine whether Service Mode has indeed achieved one of its promised targets in completing very demanding programmes by implementing flexible scheduling, one would ideally need to compare them to the success rate of these same runs if they had been scheduled in Visitor Mode. This would have to be simulated, based on the weather statistics available for the past 15 years.

Figure 8 shows the probability of realisation of given sky transparency conditions on Paranal for a scale of seeing values, based on monthly weather loss, sky transparency and seeing statistics compiled between 2008 and 2012. Here we have assumed that the underlying seeing cumulative distribution applies equally to all months. From this figure, the probability of achieving photometrically clear conditions with a particular seeing value can be read off, e.g., for 0.6 arcseconds this is ~ 20–30 % in March and November. It is reassuring to see that these values are low, when compared to the completion rates obtained in SM (~ 50 % overall, ~ 67–78 % for A class runs only). This provides strong support for the ESO mixed SM–VM model, but admittedly our SM completion rates span more than one Period for the highest priority runs.

We note that among the top 20 most-cited scientific articles based on ESO data, 30 % of their respective SM runs requested and received photometric conditions. Among these same 20 articles, of those that involve a component of Service Mode, there are at least six SM runs that required 0.6-arcsecond seeing, ten that required 0.8 arcseconds and another six required 1-arcsecond seeing.

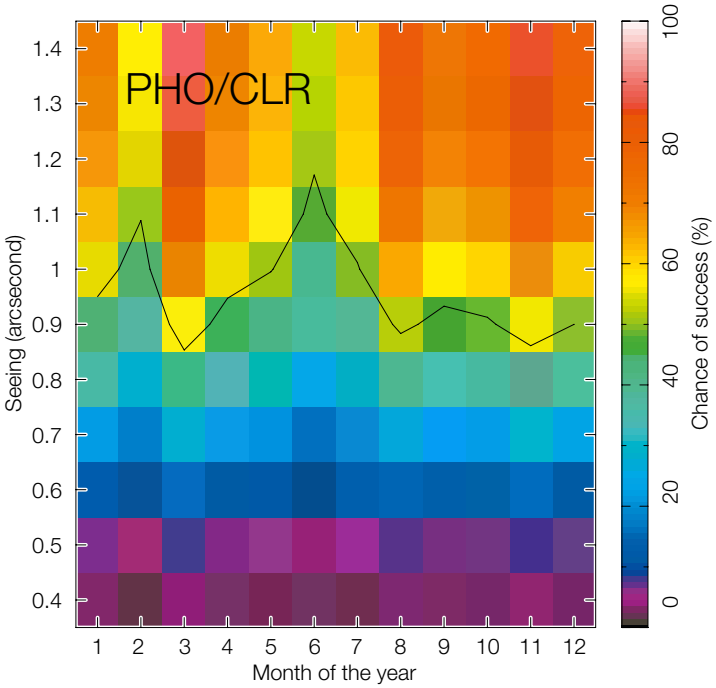

Figure 8. Percentage chance of success in the realisation of photometric/clear (PHO/CLR) conditions and different (Shack–Hartmann) seeing values, across the year at Paranal. The black line through the middle represents the 50% chance of success.

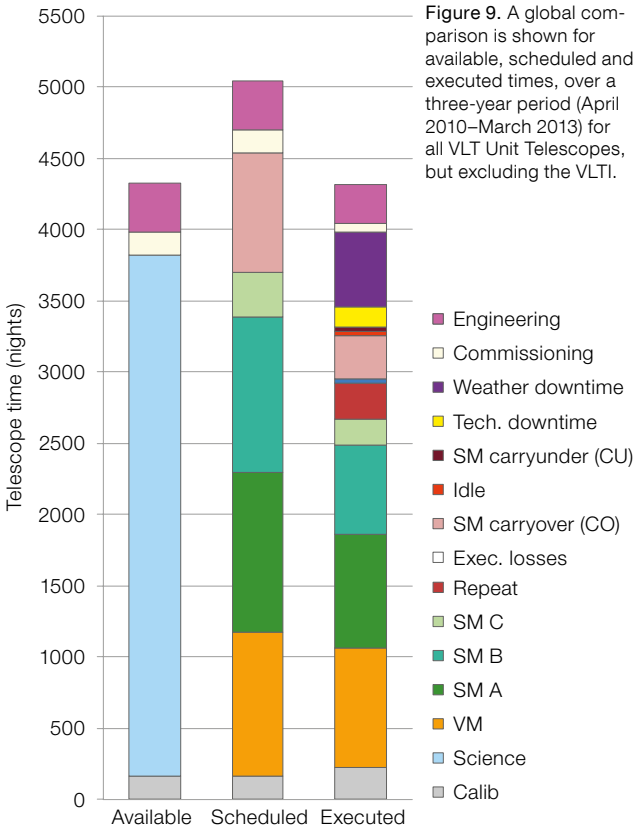

Figure 9. A global comparison is shown for available, scheduled and executed times, over a three-year period (April 2010–March 2013) for all VLT Unit Telescopes, but excluding the VLTI.

Putting it all together: The overall picture

Ideally, all this information could be captured in a single graph that takes all the relevant numbers into account. We have attempted this in Figure 9. Starting from the time available for scheduling, we looked at how this time was then scheduled and turned into successful execution. One can do this exercise per Period, but for the purposes of this article we decided to collapse all Periods between P85 and P90 into one graph — this possibly has the disadvantage of missing some details pertaining to specific Periods, but it clearly has the advantage of providing a global view over a recent three-year timespan. Figure 9 includes data for the four VLT Unit Telescopes, but omits statistics for the VLTI on account of its special features (e.g., block scheduling).

For a global perspective, one also needs to account for Visitor Mode; this appears under the only assumption that can be made, i.e., that everything scheduled was indeed executed, except for weather and technical losses. This downtime was proportionally distributed across the Periods, affecting the time assigned to SM and VM according to their allocation percentages. The result is apparent, for instance, in the orange strip of the second and third columns of Figure 9: the VM execution strip is indeed slightly shorter than the one that was scheduled, on account of this weather and technical downtime.

Figure 9 displays considerable granularity, especially in the two rightmost bars, corresponding respectively to the scheduled and executed times. Here "executed times" refer to what was executed within the available time; the numbers corresponding to Calib, SM A/B/C/CU/CO (carryunder/carryover) refer however to successfully executed observations. Before each OPC meeting, the Observatory releases a technical time schedule (shown in the first column). This includes the time reserved for technical activities in the next semester, split into engineering (shown in fuchsia in Figure 9) and commissioning (creamy-white) slots, as well as the time known (from previous Periods) likely to be invested for night-time calibrations (shown by the grey region at the bottom). The time remaining in Figure 9 is labelled as Science (shown as light blue) in the first column. This is the amount of time available for science observations and that needs to be filled by the schedulers (second column). VM slots are usually reserved first. What remains can be used for SM observations and is split evenly between A and B class runs. C class runs (sometimes referred to as fillers, because they typically have more relaxed observing constraints) come on top of the already 100% full schedule, thus representing the protective buffer against idle time and/or bad weather conditions.

As is apparent from the third column of Figure 9, weather downtime can be significant in some Periods, making a 10% provision insufficient, thus affecting completion efficiencies and creating larger carryovers. Looking then at the bar of the execution (third column), granularity increases because carryunders, carryovers, idle time, execution losses (time lost because of operational issues), repeats (i.e., time invested in SM obser-

vations that did not fulfil the requested conditions) can all be traced. It is only at this stage that we can properly close the loop on all the technical activities (i.e., the time that was truly invested in engineering and commissioning activities) and downtime (both weather and technical).

It should be noted that, until recently, no provision was made for weather downtime during scheduling, which had a major impact in some Periods. For example the weather downtime (purple area of the rightmost bar of Figure 9) is unusually large and dominated by the significant weather loss recorded for Period 85 — close to 20% of the available science time — and for P86–89 — close to 15%. Similarly, the time already committed to carryover runs was accounted for only in part, as becomes evident from the much longer bar in the second column.

From the Executed column in Figure 9, it also becomes apparent that: *i)* the UTs suffer from quite negligible idle time and very little execution loss; *ii)* carryovers and repeats (observations outside user constraints) instead have a large impact on the overall efficiency. The graph also confirms that B class runs are the most affected in terms of completion rates. As already mentioned, this is not really surprising: B class runs are usually highly demanding in terms of constraints (comparable, in fact, to A class runs) but in competition with higher priority (A class) runs.

The categories carryover and repeat, however, touch upon two different aspects of the ESO operational model: carryovers are the result of too aggressive or sub-optimal scheduling; the number of instances of repeats can in principle be reduced, but the reason(s) for them must first be properly understood. All OBs are started within constraints, but atmospheric conditions can change even within the first hour (the average OB length). From preliminary investigations, it appears that approximately 40% of repeated observations are due to varying seeing conditions and another 20% due to other variable meteorological conditions. This finding could indicate that the seeing stability that we assume at the time of scheduling is not realistic and/or that the first data quality evaluations (QC0) are too strict. The number of repeated observations varies strongly with instrument and correlates with operational complexity and sensitivity to good conditions (e.g., AO instruments tend to have larger numbers of repeated observations).

What's next

The Very Large Telescope (and Interferometer) is a complex facility. It is unique in the fact that it provides four 8-metre-class telescopes to its community 365 nights per year (except for VLTI with the Unit Telescopes, which has so far only been available in fixed time slots). Fifteen years after the start of VLT/I operations, all foci remain occupied with a suite of forefront instrumentation that allows a variety of scientific questions to be tackled. The facility remains in high demand, as seen by the number of new (unique) PIs who are attracted every Period (approximately 40% of the total).

But on account of this breadth and variety, the operation of the facility is challenging. Community feedback is generally very positive, the support interfaces are functioning well and highly valued. However, from the ESO side, it is also important to back up this positive attitude with facts and solid numbers. The effort invested so far in the DOME project is just starting to provide the baseline metrics required to analyse operational efficiency in a systematic way. Some of the graphs shown in this report seem to indicate areas that require closer scrutiny and that, if confirmed, may trigger optimisation processes.

Some actions have already been taken, such as more realistic provision for carryover and weather downtime at the time of scheduling, as well as an update in the scheduling tool for the underlying characterisation of the Paranal site in terms of seeing (distribution and stability), transparency conditions and photometric stability. On the side of operational procedures and/or science policies, ESO will now look into the low completion rates of B class runs, into the repeat category, into a renewed definition of filler programmes and ultimately into the scheduling tool, in order to make it more dynamic and able to react on shorter timescales.

In terms of the DOME project, none of the numbers and figures shown here include Large Programmes. They represent up to 15% of the total available time, secure large datasets and aim to tackle the top scientific questions of the day; thus it is definitely worthwhile to take a closer look at them. Similarly, in the near future, metrics will be further broken down (per instrument, per programme type, etc.) or the efficiency of the most complex observing modes (e.g., AO-assisted) may be examined. Part of the DOME project also consists of the monitoring of the metrics that have been extracted so far, in order to be able to uncover the trends and spot changes as quickly as possible.

Our final goal is to increase the scientific return and impact of the Observatory by optimising operations and its associated implementation. For this, we need to be able to retrieve a detailed view of parameters that measure the status and health of VLT/I operations, at any time, and be able to answer questions such as: is the current SM/VM ratio satisfactory; can any further optimisation help in improving our efficiencies and the satisfaction of the user community? The scientific return is very high, but there is clearly room for improvement. ESO will continue to look into means to improve the handling and execution of your programmes.

References

Bierwirth, T. et al. 2010, Proc. SPIE, 7737, 77370W
Comerón, F. E. et al. 2003, The Messenger, 113, 32
Hanuschik, R. & Silva, D. 2002, The Messenger, 108, 4
Patat, F. & Hussain, G. 2013, in *Organizations, People and Strategies in Astronomy 2* (OPSA 2), ed. Heck, A., 231
Primas, F. et al. 2012, Proc. SPIE, 8448, 84480L
Quinn, P. et al. 2000, Proc. SPIE, 4010, 56
Silva, D. 2001, The Messenger, 105, 18

Links

[1] VLT/VLTI Science Operations document: http://www.eso.org/sci/observing/policies/Cou996-rev.pdf
[2] Full report on the 2014 User Feedback campaign: http://www.eso.org/sci/observing/phase2/other-Info/UserFeedback.html

Flux Calibration of Medium Resolution Spectra from 300 nm to 2500 nm — Model Reference Spectra and Telluric Correction

Sabine Moehler[1]
Andrea Modigliani[1]
Wolfram Freudling[1]
Noemi Giammichele[2]
Alexandros Gianninas[3]
Anais Gonneau[4]
Wolfgang Kausch[5]
Ariane Lançon[4]
Stefan Noll[5]
Thomas Rauch[6]
Jakob Vinther[1]

[1] ESO
[2] Département de Physique, Université de Montréal, Canada
[3] Homer L. Dodge Department of Physics and Astronomy, University of Oklahoma, USA
[4] Observatoire astronomique de Strasbourg, Université de Strasbourg, CNRS, France
[5] Institut für Astro-und Teilchenphysik, Universität Innsbruck, Austria
[6] Institute for Astronomy and Astrophysics, Kepler Center for Astro and Particle Physics, Eberhard Karls University, Tübingen, Germany

A procedure to obtain reference spectra for flux standard stars from stellar model atmospheres is described. This procedure allows users to derive instrument response curves from 300 nm to 2500 nm. The technique was developed using X-shooter spectra, but is general and can also be applied to higher resolution spectra. In addition an automatic method has been defined to correct for moderate telluric absorption using telluric model spectra with very high spectral resolution that can easily be adapted to observed data.

Introduction

Accurate flux calibration of astronomical spectra requires flux calibrators with known absolute fluxes that are accessible with the same spectrograph used for the science targets. With the arrival of new generations of spectrographs that cover wide wavelength ranges and produce relatively high resolution spectra (e.g., X-shooter on the Very Large Telescope [VLT]), known and well-tested spectrophotometric standard star catalogues (e.g., Hamuy et al., 1992; 1994) are no longer adequate for spectral flux calibration. These catalogues do not extend to the near-infrared (NIR) and/or are too coarsely sampled to permit the flux calibration of medium to high resolution spectra.

In this article, we describe a procedure to obtain calibrated model spectra for flux standard stars covering the wavelength range from 300 nm to 2500 nm. These spectra are useful for deriving consistent instrumental response curves over this wide range of wavelengths with a spectral resolving power of up to 40 000, and possibly more. They may also be useful for spectrographs delivering lower resolution data (e.g., FORS2), in order to calibrate small-scale variations of the detector response.

In order to compute response curves for an instrument from observed and model spectra, the effect of the Earth's atmosphere must be removed from the observed spectra. A method for fast and efficient removal of telluric absorption features is described. This method is suffciently accurate for the intended purpose of deriving response curves and can be adapted for any other instrument, provided that the spectra are of sufficient resolution between 600 nm and 2500 nm and the positions of the stellar lines are known.

More details of the flux calibration procedure and the correction for telluric absorption can be found in Moehler et al. (2014).

Sample selection

Spectral flux calibration utilises as reference either well-calibrated observations or a spectral model of a standard star. The advantage of using a model is that it is noiseless, and does not include features imposed by the terrestrial atmosphere. Flux calibration requires the ratio of an observed spectrum and the reference spectrum and such a ratio is less sensitive to errors in the wavelength scale if the spectrum is smooth and featureless. Therefore, the ideal star to be used as a spectral flux standard has a smooth and featureless spectrum that can be accurately modelled with a minimum number of parameters. The (photometrically uncalibrated) model spectrum of a star can be used to derive the shape of the response curve of an instrument and can therefore be used to test and improve the model spectra of other stars. If an absolute flux calibration is intended, the spectral models must be accompanied by accurate absolutely calibrated (spectro-)photometric observations at some wavelengths within the wavelength range covered by the model spectrum.

For the current work, we therefore searched for stars fulfilling the following criteria:
- hot white dwarfs and hot subdwarfs in order to be able to model their spectra;
- located in the southern hemisphere;
- available flux information;
- available X-shooter spectra taken with a wide (5-arcsecond) slit to minimise slit losses.

This selection resulted in six standard stars, namely EG 274, GD 71, GD 153, LTT 3218, LTT 7987 (all hot DA white dwarfs), and Feige110 (a hot subdwarf), which also have photometric information in the near-infrared wavelength range (Vernet et al., 2008; Bohlin et al., 2001). To verify the possible influence of mismatched stellar features we also selected a star that has a spectrum free of absorption lines between 300 nm and 2500 nm, namely L97-3 (a DC white dwarf).

Identifying the best model spectra

The spectra of our standard stars include strong hydrogen lines (and in the case of Feige 110 also helium lines) that need to be properly modelled in order to sample the response of an instrument on scales of some nanometres.

For the past 20 years the physical parameters of hot white dwarfs and other hot, high-gravity stars have been determined by fitting the profiles of the hydrogen (and/or helium) absorption lines in their optical spectra (Bergeron et al., 1992; see Figure 1, left panel, for an example). This method has the advantage that it is sensitive to changes in temperature and surface gravity at high effective temperatures, when optical and near-infrared photometry become insensitive to

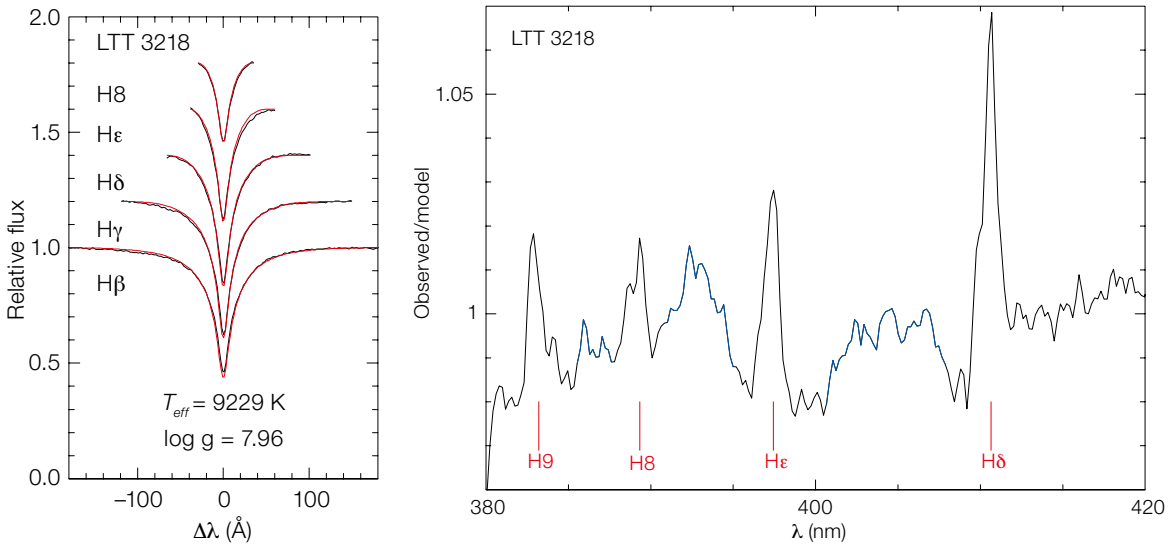

Figure 1. Left: Model fit for LTT 3218 from Giammichele et al. (2012) for individual H lines only (black lines mark observed spectrum; red lines the model). Right: Ratio between the observation and model spectrum, clearly showing residuals in the line cores (labelled) and also some bumps between the lines (marked in blue).

changes in these parameters. In consequence, this means that model spectra with an incorrect effective temperature or surface gravity will not correctly describe the strong hydrogen and/or helium absorption lines in the spectra of these stars. Such a mismatch is most severe at the blue end of the wavelength range studied in this paper, namely between 380 nm and 420 nm, where the lines may overlap with each other.

An example of such a mismatch can be seen in the right-hand panel of Figure 1, which shows the ratio of the observed to the fitted model spectrum for LTT 3218. The bumps at 390–395 nm and 400–410 nm are caused by an imperfect description of the line overlap region between the Balmer lines H8 (389 nm), Hε (397 nm) and Hδ (410 nm). Compared to the line depths of about 50 %, the effects are small (about 2 %), but sufficient to introduce noticeable artefacts in the resulting response curves. To ensure that no such mismatches exist in the finally selected reference spectra, however, the true response of the instrument with which the spectra were observed must be known.

This was the primary motivation to include the standard L97–3, whose featureless spectrum can easily be modelled in the wavelength range discussed here. This is illustrated in Figure 2, which shows the ratio of the observed spectrum to model spectrum for L97-3 for the regions containing strong lines in the spectra of the flux standard stars discussed here. As reference data for this star, a stellar model spectrum (Koester 2010) calculated for the parameters reported by Giammichele et al. (2012) was employed. This model spectrum was adjusted to the published photometry of the star. The resulting response curve, shown in Figure 2, is rather smooth without significant structure on nanometre scales (as opposed to Figure 1).

X-shooter observations of the six standard stars were used to verify the quality of the various model spectra available for them by comparing instrumental response curves from different standard stars. We concentrated first on the wavelength range 380 nm to 440 nm for the reasons discussed above. Once an acceptable description of the blue range had been achieved, its suitability for the redder wavelength ranges was verified as well. One-dimensional extracted and merged X-shooter spectra of the flux standard stars, produced with the Reflex workflow[1] (Freudling et al., 2013), were used for this analysis. These spectra were then

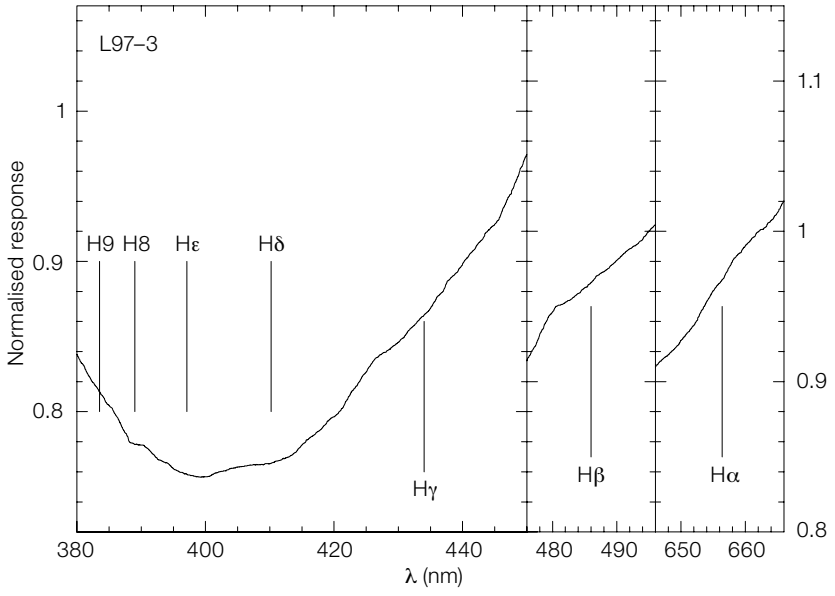

Figure 2. The average ratio of observed and shifted reference spectrum is shown for L97–3, for the same wavelength ranges as in Figure 3.

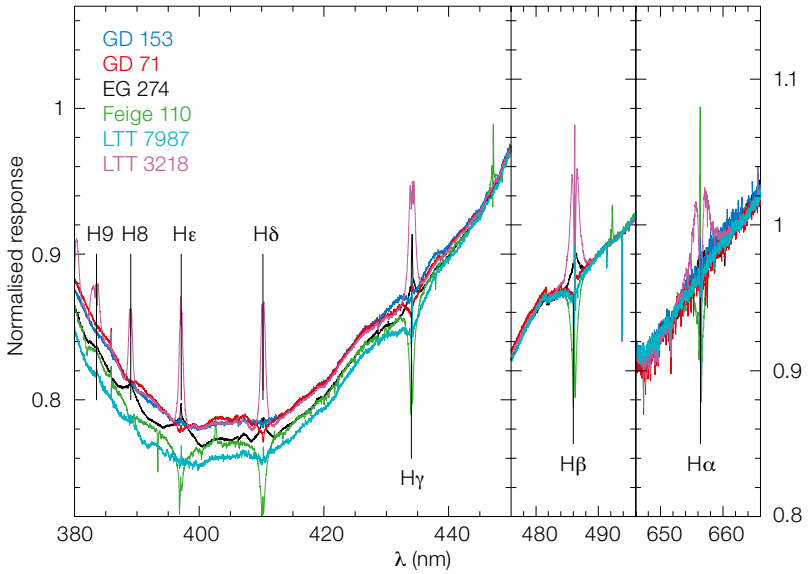

Figure 3. The average ratios of observed standard star spectrum (corrected for atmospheric extinction) and shifted reference spectrum, using the bump-corrected model spectra, are displayed. The curves have been normalised at 456 nm, 495 nm and 662.1 nm, respectively, and are offset in steps of 0.02 for better visibility. The positions of the Balmer lines are marked. Feige 110 in addition has helium lines and interstellar Ca II lines in its spectrum.

corrected for atmospheric extinction using the Paranal extinction curve and normalised by exposure time.

The model spectrum for a given star was aligned to the same radial velocity as the observed spectrum to avoid the introduction of pseudo-P Cygni profiles in the response. Each observed standard star spectrum was then divided by the shifted reference star spectrum. Finally the ratios were averaged per star to achieve a better signal-to-noise ratio. This provided raw, i.e., unsmoothed, response curves that allowed us to look for systematic discrepancies between the observed and the model spectra. Any feature in these ratios that does not appear for all standard stars points strongly towards deficiencies in the reference spectra, since instrumental effects should not depend on which standard star is used. We selected, as the best description of the stellar spectrum, those model spectra that showed the smallest star-specific bumps in the averaged ratio spectra between 380 nm and 440 nm.

In order to correct the remaining mismatches between observed and model spectra that cause bumps like those seen in Figure 1, the average raw response of each star was divided by the smoothed response curve derived from L97-3 in order to remove instrument specific variations. The products of this procedure are expected to be equal to 1.0 in an ideal case, but differences in atmospheric conditions result in residual slopes. For every star the shape of this ratio spectrum was fitted by a low-order polynomial to remove the large-scale variations, the result smoothed and the remaining bumpy regions fitted. The fitted result was then applied to the model spectrum to provide the reference spectrum.

The bump corrections were smallest for GD 71, GD 153, and Feige 110, while EG 274, LTT 7987 and LTT 3218 had significant corrections (increasing in that order). This is expected as the last three stars have the strongest and widest lines and thus present the biggest challenge in the correct treatment of overlapping lines. Since the mismatches in the line cores were not corrected (they vary with spectral resolution), some masking is still required when fitting a response (see below). We also verified that, in the spectral range 440 nm to 2500 nm, the only residuals seen in the response curves are those in the line cores of hydrogen and/or helium lines.

Photometric calibration

We have now defined a set of model spectra which adequately reproduce the observed X-shooter spectra of the six flux standard stars, with residuals (outside the line cores which are affected by resolution effects) well below 2%. To allow for a proper flux calibration we have to verify that the overall flux distribution of these model spectra reproduces the independently observed (spectro-)photometric data. To do so the model spectra for EG 274, Feige 110, LTT 3218, and LTT 7987 between 300 nm and 1000 nm were convolved to a resolution of 1.6 nm and then binned into 5 nm steps to reproduce the tabulated data (Hamuy et al., 1992; 1994). For the NIR region, the model spectra were convolved to a resolving power of 2000 (*J*-band) and 1500 (*H*- and *K*-bands) and then integrated over the wavelength ranges given in Vernet et al. (2008). These flux values were then aligned to the respective (spectro-)photometric data by a constant factor across the full wavelength range. For GD 71 and GD 153 our new model spectra could also be aligned by a constant factor to the Hubble Space Telescope model spectra (Bohlin et al., 2001). Figure 3 shows the average ratios of the observed and reference spectra for the new model spectra.

Correction of telluric absorption

We have now defined reference spectra that describe the observed spectra of the flux standard stars very well. In order to derive a response curve, the effects of the Earth's atmosphere have to be removed from the observed spectra, otherwise the response curve will contain a mixture of instrumental and atmospheric effects. The atmospheric effects consist of two major parts: atmospheric extinction (small variation with time in the case of Paranal due to the low aerosol content, which governs the extinction variability); and telluric absorption (strong variation with time in the case of water vapour). The former affects mostly the wavelength range 300 nm to 1000 nm and is described by the Paranal extinction curve. The second is important for wavelengths above 600 nm and may vary on very short timescales.

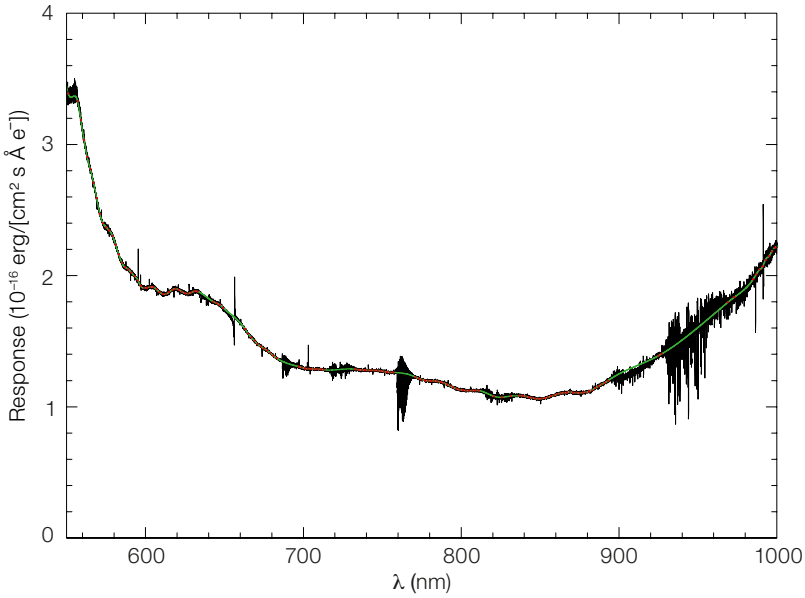

Figure 4. X-shooter response curve derived for EG 274 (VIS arm). The red dots mark the fit points and the green line the fit through these points.

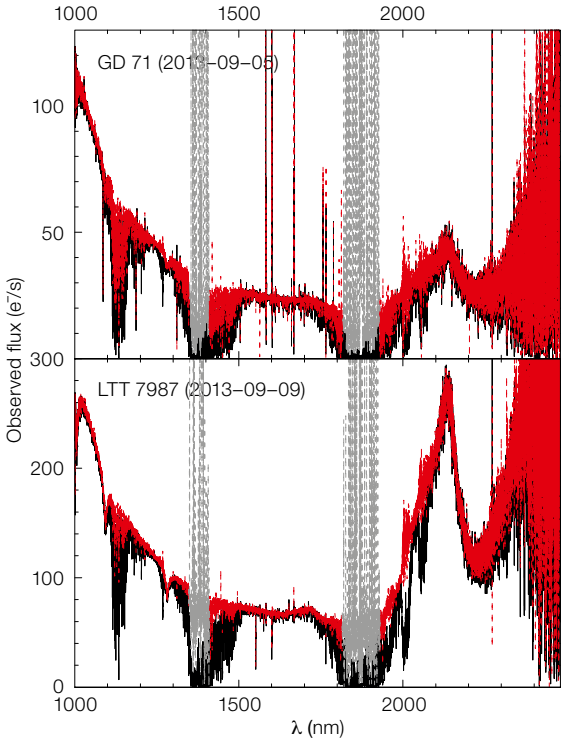

Figure 5. Results of the telluric correction (red) for a bad case (upper) and a good case (lower) are shown. Regions of extremely high telluric absorption have extremely high noise in the corrected data and are therefore omitted (1348–1410 nm, 1815–1930 nm). The lines at 1093.5 nm and 1281.4 nm are stellar lines and the variable peak at about 2100 nm is caused by variations in the flux level and spectral energy distribution of the flat field lamp.

Unless at least those parts of the spectrum that contain low-to-medium strength telluric absorption features are corrected, the response has to be interpolated across very wide wavelength ranges, resulting in large systematic uncertainties for the resulting flux calibration. Traditionally such corrections use telluric standard stars, i.e., stars with either no features or extremely well-known features in the regions of telluric absorption, which allow the user to determine the intrinsic telluric absorption spectrum. This method relies on the assumption that the conditions governing telluric absorption have not changed between the observation of the science target and the observation of the standard star. Since this assumption is often not fulfilled, it was decided instead to use a catalogue of telluric model spectra (Noll et al., 2012) in order to correct the telluric absorption lines.

High resolution atmospheric transmission spectra (R = 60 000) were calculated for the wavelength range from 300 nm to 30 µm using the line-by-line radiative transfer model code (LBLRTM; Clough et al., 2005), the HIgh resolution TRANmission molecular line database (HITRAN; Rothmann et al., 2009), and different average atmospheric profiles (pressure, temperature and molecular abundances) appropriate for Cerro Paranal.

To identify the telluric model spectrum best suited to correct a given observation, the telluric model spectra first have to be aligned to the observed spectrum in both resolution and wavelength. Then the telluric model spectrum with the smallest residuals with respect to the observation has to be identified. The following procedure was employed. Firstly the wavelength scale (in nm) of the model and observed spectra were converted to natural logarithm, because X-shooter has a constant resolving power. (For instruments with a constant full half width at half maximum with wavelength [FWHM], the procedure described below should be done in linear wavelength space.) An appropriate wavelength range of the telluric model spectra and observed spectra was then cross-correlated to determine the shift in wavelength and the difference in resolution. The telluric model spectrum was shifted and convolved with a Gaussian with the measured FWHM of the correlation peak. (Since the resolution of the observed spectra is about a factor of ten lower than the resolution of the telluric model spectra, it is assumed here that the resolution of the model spectra is infinite.) Finally, the shifted and convolved telluric model spectrum was converted back to linear wavelength space. The observed spectrum was then divided by the adjusted telluric model spectrum and normalised by a cubic spline fit using predefined continuum points (avoiding regions of strong telluric absorption as well as known lines of the observed star).

The best-suited telluric model spectrum was chosen as the one for which the average residuals computed over regions of moderate telluric absorption in the normalised telluric-corrected stellar spectrum are minimal. Figure 5 shows examples of good telluric correction (lower) and of undercorrection (upper).The telluric-corrected spectrum of the flux standard star is then compared to the stellar model spectrum to determine the response.

Users who wish to employ the telluric model spectra to correct their data can find information about the Cerro Paranal sky model (Noll et al., 2012) on the skytools webpage[2] together with pre-calculated libraries[3]. The spectra are provided with resolutions of 60 000 and 300 000 and do not include Rayleigh scattering. The SkyCalc web application[4] can always be used to produce sky radiance and transmission spectra with more specific parameters, including Rayleigh scattering.

Fitting of the response

The ratio of the observed spectrum to the shifted reference spectrum usually shows residuals at the positions of the line cores (see Figure 3), but may also show variations on intermediate wavelength scales that need to be fitted by the response curve because they are instrumental features. In the case of X-shooter we found that the best solution was a spline fit to a list of wavelengths per star, where the median of the raw response across a pre-defined window is determined at each listed wavelength (see Figure 4 for an example). Also the quality of the telluric correction has to be kept in mind when fitting a response, as regions with remaining absorption or overcorrected features may distort the fit. For this reason we finally decided to mask certain regions affected by telluric absorption when fitting a response curve, in order to avoid potential telluric residuals (see Moehler et al. [2014] for details). We would like to emphasise that even with this masking far less of the spectrum is rejected than would be necessary if no telluric correction had been applied.

Final remarks

To illustrate the quality that can be achieved with the methods and model spectra described in this paper, we show in Figure 6 an example for a standard star (LTT 7987). The spectrum was flux-calibrated with the response curve determined from a different star observed on the same night, namely EG 274. Part of the response curve used for this calibration is shown in Figure 4.

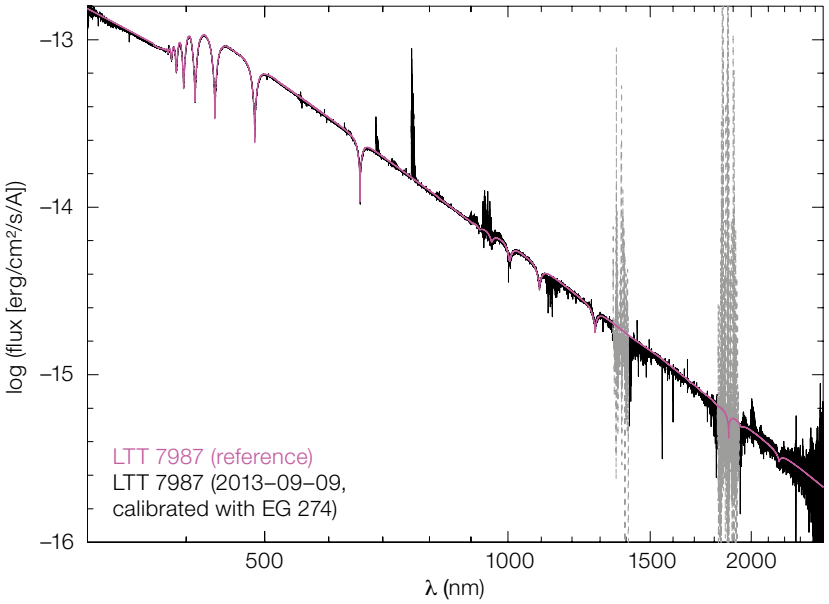

Figure 6. Spectrum of LTT 7987, corrected for telluric absorption and flux-calibrated with a response curve derived from observations of EG 274. The magenta curve is the reference spectrum for LTT 7987. Regions of very high telluric absorption are omitted (1348–1410 nm, 1815–1930 nm).

While the set of standard stars is adequate to flux calibrate spectra observed in the southern hemisphere, additional standards would be useful both to enlarge the number of potential calibrators in the south, and to provide a similar set of standards in the northern hemisphere. The methodology described here can be used to derive such a set of model spectra. Necessary ingredients for such an endeavour are accurate model spectra, availability of flux information, and observed uncalibrated spectra for both the new calibrators and at least one of the standard stars discussed here to correct for instrumental features. For hot (pre-) white dwarfs, like the flux standard stars discussed here, and many others, a good starting point for model spectra would be the TMAP spectral energy distribution available from the registered Virtual Observatory service TheoSSA[5] provided by the German Astrophysical Virtual Observatory[6].

Acknowledgements

This research made use of the NASA Astrophysics Data System Bibliographic Services and the SIMBAD database, operated at CDS, Strasbourg, France. We thank D. Koester for making his model spectra available to us. We are grateful to J. Vernet, V. Mainieri, and F. Kerber for sharing their SINFONI results with us. We also thank F. Patat, R. Lallement and W. Reis for their help with the improvements of the X-shooter response.

References

Bergeron, P., Saffer, R. A. & Liebert, J. 1992, ApJ, 394, 228
Bohlin, R. C., Dickinson, M. E. & Calzetti, D. 2001, AJ, 122, 2118
Clough, S. A. et al. 2005, J. Quant. Spectrosc. Radiat. Transfer, 91, 233
Freudling, W. et al. 2013, A&A, 559, A96
Giammichele, N., Bergeron, P. & Dufour, P. 2012, ApJS, 199, 29
Hamuy, M. et al. 1992, PASP, 104, 533
Hamuy, M. et al. 1994, PASP, 106, 566
Koester, D. 2010, MmSAI, 81, 921
Moehler, S. et al. 2014, A&A, 568, A9
Noll, S. et al. 2012, A&A, 543, A92
Rothman, L. S. et al. 2009, J. Quant. Spectrosc. Radiat. Transfer, 110, 533
Vernet, J. et al. 2008, SPIE, 7016, 70161G

Links

[1] Reflex X-shooter workflow: http://www.eso.org/sci/software/pipelines/
[2] Cerro Paranal sky model: http://www.eso.org/sci/software/pipelines/skytools/
[3] Library for calculation of model sky: ftp://ftp.eso.org/pub/dfs/pipelines/skytools/telluric_libs
[4] SkyCalc web application: http://www.eso.org/observing/etc/skycalc/skycalc.htm
[5] TMAP spectral energy distributions: http://dc.g-vo.org/theossa
[6] GAVO: http://www.g-vo.org

The GIRAFFE Archive: Reduced Spectra and Datacubes from the VLT FLAMES GIRAFFE Spectrograph

Frédéric Royer[1]
Isabelle Jégouzo[1]
Régis Haigron[1]
Françoise Tajahmady[1]
Fabien Plassard[1]

[1] GEPI, CNRS/UMR 8111, Observatoire de Paris, Université Paris Denis Diderot, Meudon, France

Since 2003, the intermediate- and high-resolution multi-fibre spectrograph GIRAFFE, part of the FLAMES facility, has been producing 1D spectra in its multi-object configuration and 3D spectra using its integral field unit configurations. Raw data are available in the ESO archive. The GIRAFFE archive (http://giraffe-archive.obspm.fr) offers the community, via a web interface and the Virtual Observatory (VO), access to reduced scientific data. The web interface to the database allows the use of a large range of selection criteria, including individual target positions, magnitudes and signal-to-noise ratios, together with an interactive quick look at the reduced data. Two collections are available in the VO: the 1D spectra (summed in the case of integral field observations) and the 3D field observations.

FLAMES/GIRAFFE

The GIRAFFE spectrograph is part of the FLAMES facility (Pasquini et al., 2002) and combines high-resolution spectroscopy and multiplex capabilities with the Very Large Telescope (VLT) Unit Telescope 2. As a result of these properties, the scientific applications of GIRAFFE cover a wide range of topics, from stellar to Galactic and extragalactic studies. Since it started operations in spring 2003, GIRAFFE has been producing scientific data at the average rate of about 140 multi-object observations per month.

The multiplex capability of GIRAFFE relies on three different fibre systems that can be used to feed the instrument. These consist of a set of "Buttons" and are:

– Medusa (MED), where the 135 Buttons are composed of individual fibres, with a circular 1.2-arcsecond aperture on the sky that can be deployed in the 25-arcminute diameter field of view (FoV);
– Integral field unit (IFU), where the set of Buttons is composed of 15 separate 4 by 6 micro-lens arrays (2 by 3 arcseconds), also deployable in the FoV;
– Argus (ARG), a single central array (22 by 14 micro-lenses), with two available spatial scales giving a sampling of 0.52 and 0.3 arcseconds per micro-lens.

When data-mining multi-object observations, two different search levels are needed: a high level to retrieve full observational datasets and a low level to directly access individual object data. Raw data produced by GIRAFFE are distributed by ESO and are searchable in the ESO archive at the high level. The motivation of the GIRAFFE archive[1] is to provide advanced data products, searchable at both levels: high (Field) and low (Button).

Data processing

The data stored in the GIRAFFE archive are the result of automatic processing. Once publicly available, raw data are retrieved from the ESO archive and are reduced with the standard ESO pipeline. The calibration and science products are created according to the following steps:

– Using the reduction recipe gimasterbias, a master bias frame is produced for each night where the required number of raw bias frames are available;
– The reduction recipe gimasterdark is used to process raw dark frames, taken on an approximately monthly basis. Dark subtraction is applied only in the scientific reduction;
– Before using gimasterflat, raw flat-field frames are analysed to automatically detect broken fibres. The output fibre list is used as a parameter when running the recipe gimasterflat. The localisation and extracted flat fields are built for each set-up and slit for each night. In Medusa mode, the optimal extraction method is used for extracting these spectra;
– Using giwavecalibration, the slit geometry and wavelength solution are built for each set-up and slit, in two different runs of the recipe, for each night;
– Using giscience, each raw science exposure is reduced individually using the aforementioned calibration products. In Medusa mode, optimal extraction is used. For IFU and Argus data, the chosen output format for the datacubes is ESO3D (Kuntschner et al., 2012). The standard stars are processed as regular scientific frames. No flux calibration is performed on GIRAFFE data;
– The signal-to-noise ratios (SNR) are derived for the scientific spectra using the DER_SNR algorithm (Stoehr et al., 2008);
– In addition to the science products, sky subtraction is performed to compute the median sky from the dedicated fibres and subtract it from the spectra of all the fibres.

Only products from the science reduction are stored in the GIRAFFE archive. These products are:

– a FITS file in native format consisting of an image, where each column is an extracted calibrated spectrum;
– the errors on the flux, in FITS native format;
– the sky-subtracted flux, in FITS native format, when sky subtraction was possible;
– the concatenated reduction log (full calibration cascade);
– in the case of IFU and Argus modes, the ESO3D FITS datacube, containing 3D images of fluxes and errors for all the observed buttons.

Data pass through quality control prior to ingestion into the archive. The check is based on the statistics of the reduced spectra, the ambient temperature difference between the scientific observations and their matching calibration products, and the velocity dispersion of the wavelength solution. Only compliant reductions are ingested into the archive.

Web interface[1] and data mining

Different snapshots of the web interface illustrate this paper. For clarity, the specific parts of the figures, uniquely labelled with circled numbers, are referred to in the text and captions by bold numbers in parentheses.

Search interface

The form displayed in Figure 1 is a snapshot of the search interface. There are two search levels in the archive: Field, corresponding to full observations and Button, which corresponds to individual objects. Specifying this search criterion (1) is mandatory. The other search criteria are organised in five panels related to the object information, the exposure parameters, the fibre configurations, the instrumental set-up and the spectral characteristics. The criteria related to the objects are matched against information taken from the observations themselves: the celestial coordinates, object names and magnitudes stored in the archive are the ones provided by the original observer. The Target criterion (2) is optional and can be either a name, which will be automatically resolved into a position using Simbad, or right ascension and declination directly.

When Field is selected, the search is performed on the global parameters of each target: cone search on field centre positions, range of magnitudes, range of SNR, etc; however if Button is selected, the search is performed on the individual parameters of each MED spectrum: cone search on target positions, individual magnitudes and SNR.

The fibre buttons allocated to sky positions are not searchable in the database, provided that they were correctly flagged during the observation preparation. They are nonetheless part of the Field-related products. When the tick box specifying sky-subtracted data is checked (3), this criterion will propagate through the resulting pages and the related data products. This propagated information is indicated by a label on the corresponding pages, e.g., on Figure 5, (17).

Figure 2 shows a sketch of the browsing steps in the web interface, proceeding from the search form. The six coloured boxes in the flowchart stand for the different types of web pages in the interface and arrows represent the hyperlinks through which they can be browsed. Left and right columns respectively correspond to the Field and Button search levels. The three types of web page, from top to bottom, are:

– the query results, where all matching data are listed in a paginated table;

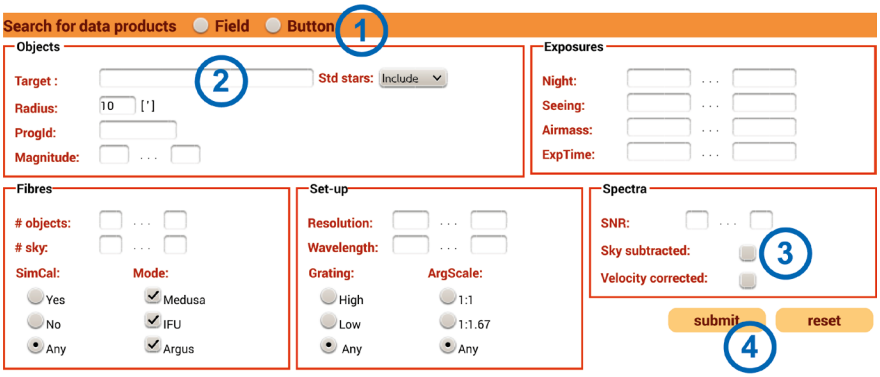

Figure 1. The GIRAFFE archive search interface is shown. The mandatory criterion Field/Button (1) must be specified. The other criteria are organised in five panels related to object information, exposure parameters, fibre configurations, instrumental set-up and spectral characteristics. See text for details.

– the data product pages, which give details for individual data products (Field or Button);
– a dedicated visualisation tool which allows the user to explore both spatially and spectrally the content of the data (see section on SCubOX).

Query results

Once the desired criteria are given and the query is submitted (4), the list of matching data is displayed. The relevant parameters are listed in the different columns (Figure 3). On each row, the Observation ID can be clicked to access Field data product pages. In Button queries, the content of the Object column links to the Button data product. The columns Observation ID, Magnitude and SNR can be sorted. Rows can be selected using tick boxes (5). The selection can be retrieved as a VOTable list (6) or the different files can be downloaded (7).

Download options

Data products can be downloaded from the web interface as shown in Figure 2, at different levels. Multiple download of selected products is possible from the query result lists (labels a and b in Figure 2), and files related to individual observations are available from the data product pages (c and d). The content of these downloads is the following:

(a) The selection of rows in the Field query results allows the user to download the corresponding Field FITS files, in native format — see (7) in Figure 3.

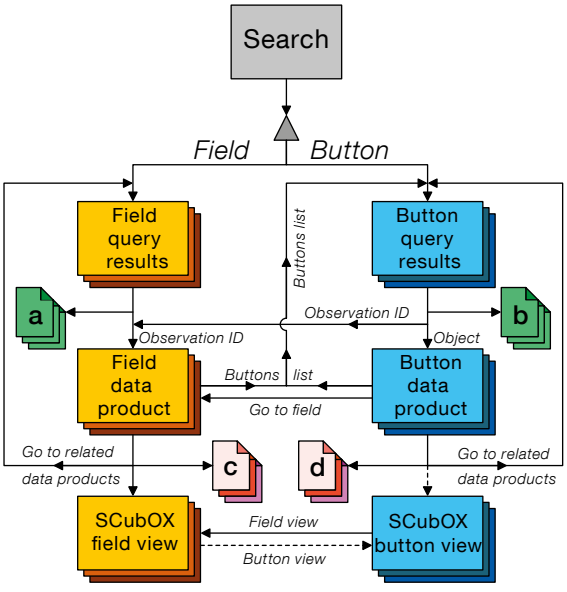

Figure 2. A flowchart of the browsing process in the web interface is shown. Horizontal boxes represent web pages and file icons stand for downloads. The different download options are detailed in the text. Labelled arrows represent hyperlinks, conditional when shown dotted.

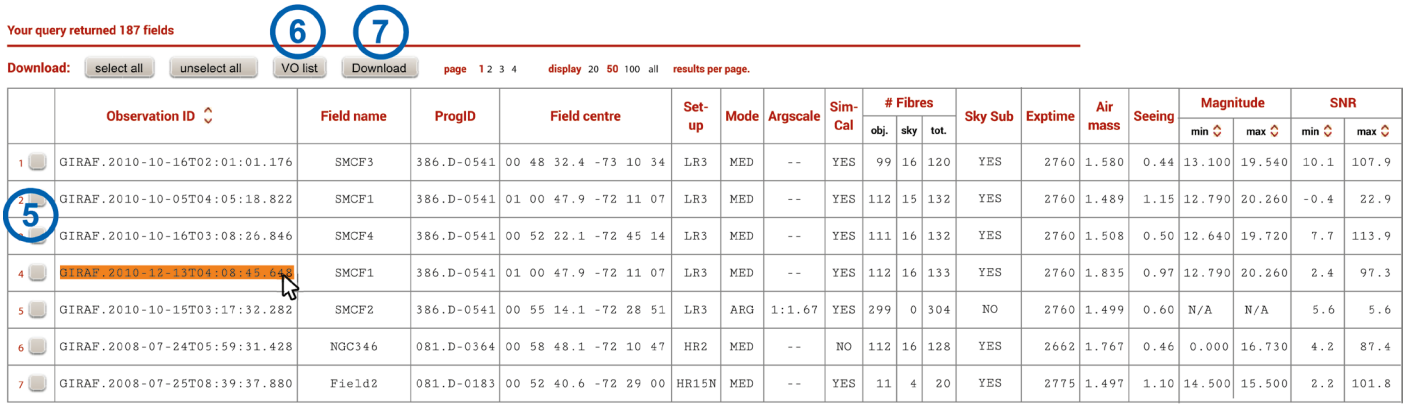

	Observation ID	Field name	ProgID	Field centre	Set-up	Mode	Argscale	Sim-Cal	# Fibres obj.	# Fibres sky	# Fibres tot.	Sky Sub	Exptime	Air mass	Seeing	Magnitude min	Magnitude max	SNR min	SNR max
1	GIRAF.2010-10-16T02:01:01.176	SMCF3	386.D-0541	00 48 32.4 -73 10 34	LR3	MED	--	YES	99	16	120	YES	2760	1.580	0.44	13.100	19.540	10.1	107.9
2	GIRAF.2010-10-05T04:05:18.822	SMCF1	386.D-0541	01 00 47.9 -72 11 07	LR3	MED	--	YES	112	15	132	YES	2760	1.489	1.15	12.790	20.260	-0.4	22.9
3	GIRAF.2010-10-16T03:08:26.846	SMCF4	386.D-0541	00 52 22.1 -72 45 14	LR3	MED	--	YES	111	16	132	YES	2760	1.508	0.50	12.640	19.720	7.7	113.9
4	GIRAF.2010-12-13T04:08:45.648	SMCF1	386.D-0541	01 00 47.9 -72 11 07	LR3	MED	--	YES	112	16	133	YES	2760	1.835	0.97	12.790	20.260	2.4	97.3
5	GIRAF.2010-10-15T03:17:32.282	SMCF2	386.D-0541	00 55 14.1 -72 28 51	LR3	ARG	1:1.67	YES	299	0	304	NO	2760	1.499	0.60	N/A	N/A	5.6	5.6
6	GIRAF.2008-07-24T05:59:31.428	NGC346	081.D-0364	00 58 48.1 -72 10 47	HR2	MED	--	NO	112	16	128	YES	2662	1.767	0.46	0.000	16.730	4.2	87.4
7	GIRAF.2008-07-25T08:39:37.880	Field2	081.D-0183	00 52 40.6 -72 29 00	HR15N	MED	--	YES	11	4	20	YES	2775	1.497	1.10	14.500	15.500	2.2	101.8

Figure 3. An example of a Field query result list is shown; only the first few rows are displayed. The Observation IDs in the first column, as shown by the cursor over the identifier, are links to the corresponding Field data product pages (see Figure 4). See text for details.

(b) The selection of rows in the Button query results gives access to the individual 1D spectra (reformatted into standard 1D FITS images).

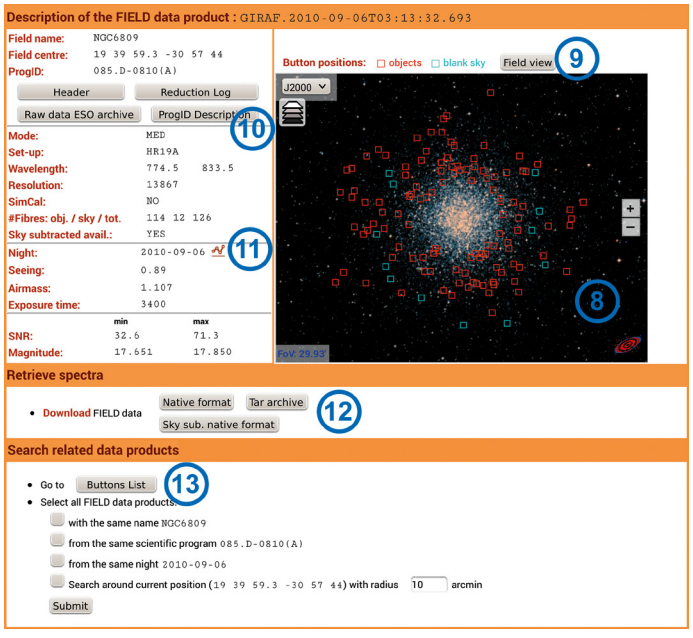

(c) From a Field data product page, the user can download several files: the reduced spectra in native format, the ESO3D cube if relevant, and their sky-subtracted version if available. The user can also download a tarball containing the reduced spectra and their corresponding error frames, an additional file containing the individual SNR, the full reduction log, the ESO3D datacube and the reconstructed images when relevant — see (12) in Figure 4.

(d) From a Button data product page, the user can download 1D spectra, with and without sky subtraction, and individual ESO3D cubes when relevant — see (18) in Figure 5.

Figure 4. An example of a Field data product page is displayed for the region around the globular cluster M55. Information related to the full observation is displayed and shows the fibre configuration (8) overplotted on the sky image using the Aladin Lite viewer: red squares represent object positions and blue squares stand for fibres allocated to blank sky positions. More details are given in the text.

Field data products

As shown in Figure 4, a Field data product page displays the fibre configuration in an Aladin Lite viewer (Boch & Fernique, 2014), distinguishing target-allocated buttons (red) from sky-allocated fibres, in blue (8). The interactive view can be zoomed and panned. Further interaction is available through the link Field view (9), further detailed in the section on SCubOX. This page also links to information available on the ESO website: the

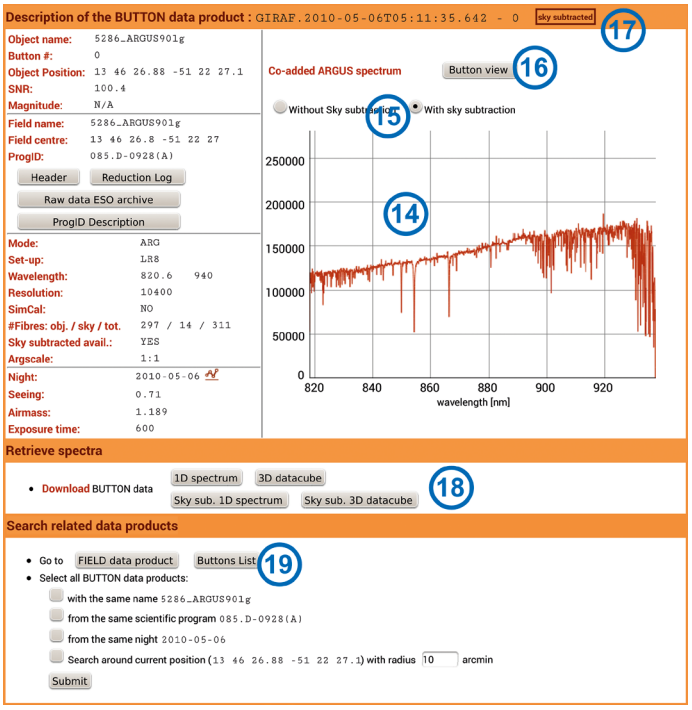

Figure 5. Example of a Button data product page, for an Argus observation of NGC 5286 is shown. The spectrum (14) summed over the Argus array is displayed. In this example, sky-subtracted data were queried (17). See the text for more detail.

description of the observing programme (10) and the environmental conditions of the night (11). The link Buttons list (13) gives the content of the observation in terms of objects and allows the user to go to specific targets. The latter can also be accessed by clicking directly on their positions in the Aladin Lite viewer.

Button data products

The data related to individual targets are displayed in the Button data product pages (Figure 5). The 1D spectrum and its error bar are plotted in a dygraphs chart (14) and the user can zoom and pan to explore the spectrum. If sky-subtracted data are available, the plot can be switched from non sky-subtracted to sky-subtracted (15). In the case of IFU and Argus mode, where the button is composed of several fibres, the 1D spectrum is the sum over the different fibres. The details of the button spaxels (spatial pixels) can be explored with the Button view link (16), detailed in the next section. Two links (19) allow the user to go back to the Field level of the observation or explore the other Buttons.

Virtual Observatory access

The data are available in the Virtual Observatory in two collections, via the simple spectrum access (SSA) services, hosted by the VO-Paris Data Centre:
– GIRAFFE-1D: the 1D Button spectra (co-added in case of IFU and Argus);
– GIRAFFE-3D: the full Field reduced spectra.

The SSA services can be queried through VO tools or the VO-Paris Data Centre portal[2].

Exploring data products with SCubOX

A visualisation client, SCubOX (Spectral Cube Online eXplorer), is being developed to display spatial and spectral data via a web service. It has both Field and Button views.

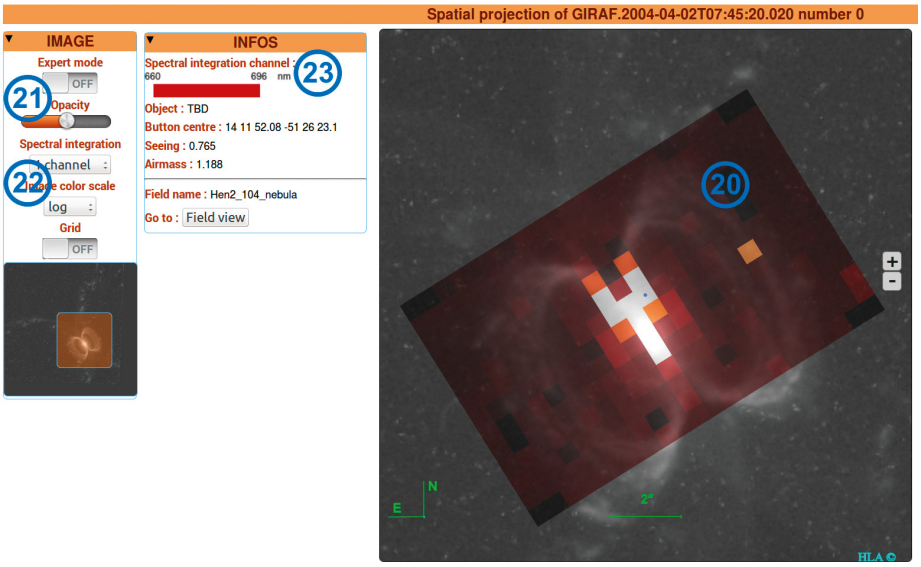

Figure 6. Example of a ScubOX Button view for an Argus observation of the Henize 2-104 planetary nebula. The cube is projected on the sky image and the different spaxels are displayed with a colour map based on the flux integrated over the wavelength axis (20).

Field view

The Field view combines the graphical displays of Field and Button data product pages in a single interface. Selecting targets in the Aladin Lite viewer loads their spectrum in the 1D dygraphs chart.

When buttons are composed of several spaxels, a link to the Button view is available.

Button view

This interface (Figure 6) plots the spatial projection of the datacube (20) over an image fetched from an online archive. The Hubble Legacy Archive is preferably checked (the source of the image is displayed in the lower-right corner). The opacity level of the projection can also be tuned (21). The spectral flux of the cube is integrated to produce the projected image: this integration can be done either on the full spectral range to produce a monochromatic image or the flux can be integrated on three equal spectral channels to produce a trichromatic red–green–blue image (22). The spectral channels are indicated in the INFOS box (23). An expert mode, allowing the display of the different spaxel spectra, is in progress.

Future developments

Several major capabilities as well as technical features will be implemented in the near future. The next objectives are the following:
– Use skycorr (Noll et al., 2014) to subtract the sky contribution;
– Offer the possibility to export the results of a query as a catalogue;
– Finalise the expert mode for SCubOX Button views allowing more versatility;
– Broaden the use of SCubOX and allow input 3D datacubes from different instruments to be accepted.

References

Boch, T. & Fernique, P. 2014, in ADASS XXIII, ASP Conf. Series, 485, 277
Kuntschner, H. et al. 2012, The Messenger, 150, 30
Noll, S. et al. 2014, A&A, 567, A25
Pasquini, L. et al. 2002, The Messenger, 110, 1
Stoehr, F. et al. 2008, in ADASS XVII, ASP Conf. Series, 394, 505

Links

[1] GIRAFFE archive: http://giraffe-archive.obspm.fr
[2] VO–Paris Data Centre portal: http://voparis-srv.obspm.fr/portal

MPG/ESO 2.2-metre and Wide Field Imager colour composite of the Galactic star cluster NGC 3532 formed from exposures in *B, V, I* and Hα filters. NGC 3532 is a rich, intermediate age (~ 300 Myr), open cluster at a distance of about 500 pc. See Release eso1489 for more details.

ESO/G. Beccari

The Eta Carinae Homunculus in Full 3D with X-shooter and Shape

Wolfgang Steffen[1]
Mairan Teodoro[2]
Thomas I. Madura[2]
José H. Groh[3]
Theodore R. Gull[2]
Andrea Mehner[4]
Michael F. Corcoran[2]
Augusto Damineli[5]
Kenji Hamaguchi[6]

[1] Instituto de Astronomía, UNAM, Ensenada, Mexico
[2] Goddard Space Flight Center, Greenbelt, USA
[3] Geneva Observatory, Geneva University, Sauverny, Switzerland
[4] ESO
[5] Instituto de Astronomía, Geofísica e Ciências Atmosféricas, Universidade de São Paulo, Brazil
[6] Department of Physics, University of Maryland, Baltimore, USA

Massive stars like Eta Carinae are extremely rare in comparison to stars such as the Sun, and currently we know of only a handful of stars with masses of more than 100 $M_{\odot}$ in the Milky Way. Such massive stars were much more frequent in the early history of the Universe and had a huge impact on its evolution. Even among this elite club, η Car is outstanding, in particular because of its giant eruption around 1840 that produced the beautiful bipolar nebula now known as the Homunculus. In this study, we used detailed spatio-kinematic information obtained from X-shooter spectra to reconstruct the 3D structure of the Homunculus. The small-scale features suggest that the central massive binary played a significant role in shaping the Homunculus.

Introduction

In August 2014 the stars of the η Car binary system were at their closest approach. The observable changes in the weeks around periastron are rather dramatic, because of the highly eccentric orbit. Therefore, many groups had been preparing to observe η Car, looking for changes that might help us learn more about this complex system of high-mass stars and interacting stellar winds, and its effect on the surrounding gas and dust, including the famous Homunculus Nebula. A comprehensive overall review by many authors on different aspects of η Car and its surroundings can be found in Davidson & Humphreys (2012).

In recent work (Steffen et al., 2014), based on spectroscopic observations with X-shooter on the Very Large Telescope (VLT), we found the first strong evidence for a direct impact of the binary system on the structure of the bipolar Homunculus Nebula that was ejected in the giant eruption around 1840. Here we briefly describe the motivation, observations and results of this work. It is particularly interesting how the rather simple geometric results connect to sophisticated theoretical simulations of the interacting winds of the central binary (Madura et al., 2013).

Owing to the large difference in brightness and closeness to the primary, the existence of the secondary can only be inferred indirectly, mainly through the 5.5-year periodicity in the X-ray band and spectroscopic changes in the ultraviolet, optical and infrared bands (Damineli et al., 2008). Finding direct evidence of the binary interaction in the Homunculus Nebula would therefore shed some light on the eruption process itself and would help to further constrain the orientation of the highly elongated orbits. The fact that there are two nebulae, the Little Homunculus (Ishibashi et al., 2003) located within the Homunculus, and the fast-moving ejecta outside the Homunculus, both exhibiting the same elongated shape, provides hints that the binary system played a role in shaping the eruptions.

To achieve these goals, the structure of the Homunculus needed to be derived in more detail than that provided by the available axi-symmetric models. Spatially resolved kinematic data with full coverage were needed in the infrared, since in the visible spectrum the Homunculus is optically thick, greatly obscuring the far sides of the bipolar lobes.

Observations

The X-shooter spectrograph mounted on the VLT's Kueyen Unit Telescope (UT2) is ideally suited for mapping the Homunculus. The 0.4 by 11 arcsecond slit provided seeing-limited spatial resolution with spectral resolving power of 11 300, which is well matched to the approximately ten-arcsecond-wide bipolar structure. Since the structure expands at velocities up to 650 km s^{-1} along the line of sight, image slices with 50 km s^{-1} separation provided detailed maps of the structure along the line of sight. While the spectral range of the data extended from 2999 Å to 24 790 Å, for this particular work we focussed on a single emission line of molecular hydrogen, the v = 1-0 S(1) line at 2.12125 μm.

The Homunculus was mapped with a total of 92 dithered positions orienting the slit perpendicular to the projected bipolar axis (position angle [PA] = −41 degrees). To provide a suitable dynamic range for each slit position, the exposure times ranged from 30 seconds in the outer regions to 0.067 seconds over the central star. Multiple images at each position were then combined to yield a total exposure time from 30 seconds in the central region to 150 seconds in the outer lobes.

After standard processing for individual spectra, a datacube was generated on a regular position–velocity (P–V) grid interpolating between actual slit positions. Figure 1 shows an optical Hubble Space Telescope (HST) image of the Homunculus with the observed slit positions in grey and the interpolated slit positions for modelling in red. For the 3D modelling process, 16 slit positions were selected from the combined datacube based on significant structural changes. These 16 P–V images are displayed in Figure 2 together with P–V images synthesised from the model.

3D modelling

The 3D modelling was done with the virtual astrophysical modelling laboratory Shape (version 5, Steffen et al., 2011)[1]. The general assumption for the reconstruction of the position information along the line of sight is that the nebular material was ejected in a short interval of time in the relatively distant past and is expanding homologously (i.e., the position vector of each volume element

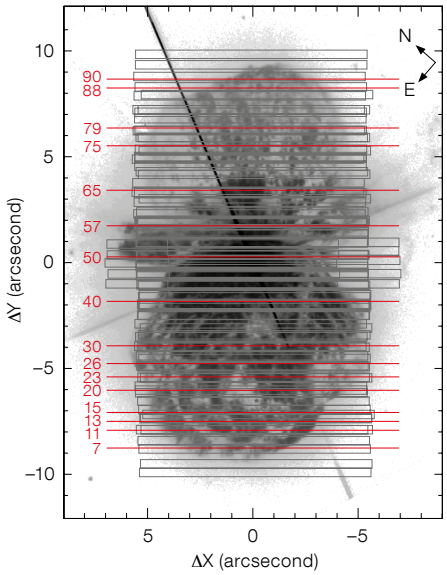

Figure 1. Observed X-shooter slit positions (horizontal rectangles) superimposed on an optical Hubble Space Telescope image of the Homunculus Nebula. The spectra were combined to generate a continuous datacube. The red horizontal lines show the positions at which position–velocity images were extracted from the datacube for modelling (see Steffen et al. [2014] for more detail).

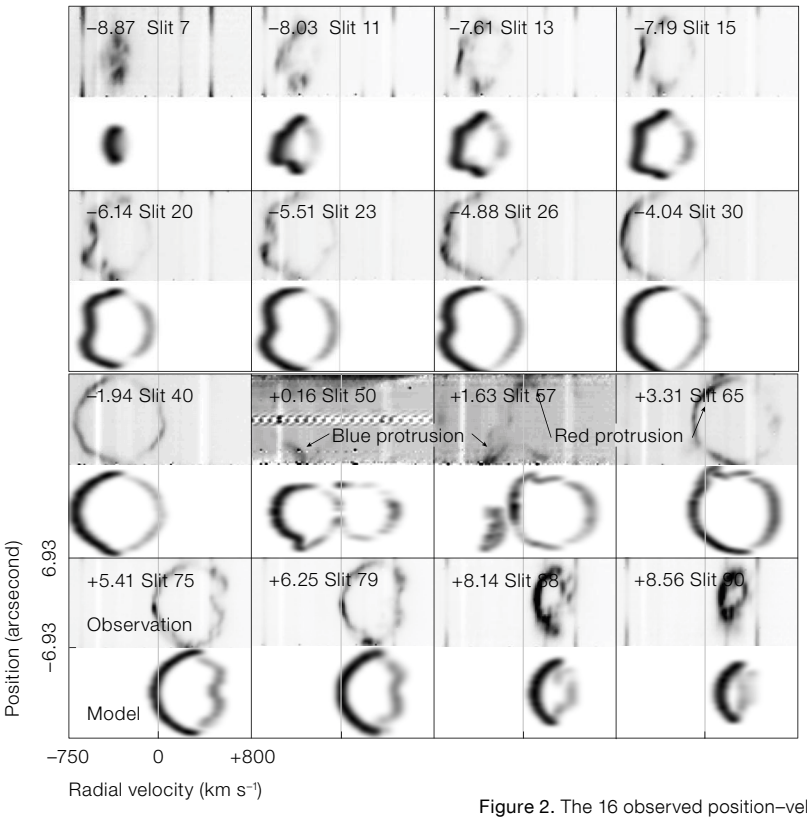

Figure 2. The 16 observed position–velocity images that have been used for 3D modelling are shown (rows 1, 3, 5, 7), together with the corresponding model position–velocity images (rows 2, 4, 6 and 8) beneath (from Steffen et al., 2014). The slit numbers and offset along the Homunculus long axis (Figure 1) are indicated.

is proportional to its velocity vector). Physically, such an expansion pattern is expected from an explosion or eruption in which the gas is accelerated very quickly and then expands with constant speed radially outwards. Furthermore, the process of ejection must be short compared to the time that has elapsed between the eruption and the observation in order to allow the matter to sort itself out according to its velocity.

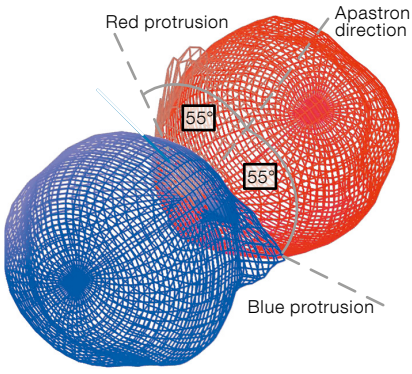

Figure 3. The 3D model mesh of the Homunculus as seen from Earth. The direction of binary apastron and its angular relation to the newly discovered protrusions are marked with dashed lines (adapted from Steffen et al., 2014).

If the expansion can be assumed to be homologous and there is a good degree of axial symmetry, then an accurate mapping can be derived between position and observed velocity along the line of sight. The massive, dense eruption that produced the Homunculus is expected to expand nearly homologously because of its high density compared to the local circumstellar environment, which is probably a hollow cavity blown out by the earlier stellar winds. Previous work and our reconstruction are consistent with only very minor deviations from large-scale homologous expansion.

The reconstruction was done in the Shape software´s interactive mesh reconstruction mode. The general procedure for such reconstructions is to interactively generate a 3D mesh shell that represents the observed gas shell volume (Figure 3). The detailed structure of this mesh is obtained by deforming an initially spherical object using a variety of “modifier” tools. An emissivity distribution and a velocity field are then defined. Finally, the software computes spatial and position–velocity images for the synthetic slit positions that correspond to the observations. The results can then be compared directly with the observations. The differences between the observations and model output are then iteratively corrected until the result satisfactorily reproduces the observations. In Figure 2, observed and synthetic position–velocity images are shown together, which allows an estimate of the precision of the reconstructed geometry.

Results

The resultant 3D mesh structure, shown in Figure 3, provides significant details of the well-known bipolar structure seen at optical wavelengths, as imaged in Figure 1. At the poles of each lobe are holes, previously found by Teodoro et

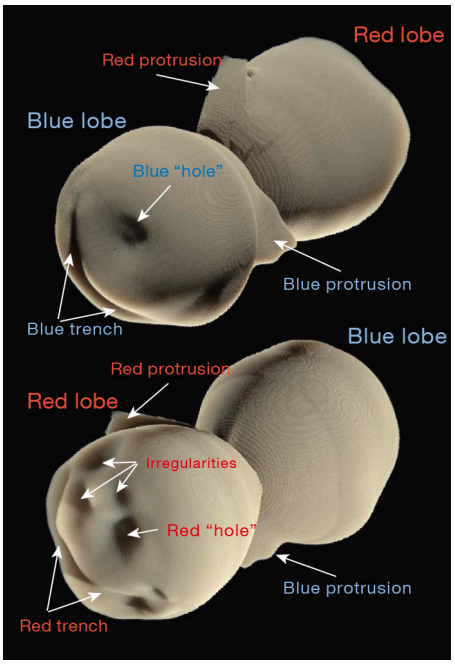

Figure 4. Two renderings of the 3D surface structure of the Homunculus model that emphasises the small-scale structure (adopted from Steffen et al., 2014). The view from Earth is shown in the upper image, whereas the lower one is a view from the opposite direction. The lobes are denoted according to their actual red or blue spectral line shift as viewed from Earth. (A 3D version is available in the online *Messenger*.)

al. (2008) from maps of the near-infrared [Fe II] 1.257 µm line. Looking more closely, these "holes" are off-centre by roughly eight degrees. Each polar cap is gouged by a trench, each of which is positioned with approximate point-symmetry, not mirror-imaged with respect to the central star. There are also red and blue protrusions extending from the lobes near the mid-plane of the nebula. One protrusion is seen on the near lobe to the right (west) and another on the far lobe pointing to the top (north). Added to Figure 3 are three lines that lie in the equatorial plane: projections of the red and blue protrusions onto the equatorial surface and the apastron direction of the binary. The latter was derived by Madura et al. (2013) based on 3D models of the extended winds mapped deep within the Homunculus by the Space Telescope Imaging Spectrograph (STIS) on board HST (Gull et al., 2009).

We initially thought that the protrusions near the equatorial region, at latitudes between about 10 degrees to 20 degrees might be due to a ring-like structure, but the modelling showed that they are quite localised, one on each lobe. Their projected separation is about 110 degrees, very close to the apparent opening angle of the wind–wind bowshock produced by the massive interacting winds of η Car when the stars are at apastron (Madura et al., 2012). The two trenches (Figure 4) have never before been identified and are similar in angular extent and position relative to the central binary.

Independently obtained and apparently disconnected results that turn out to have a strong correlation hint towards a causal relation between the interacting winds and the features of the Homunculus we have identified in our analysis. We note that the 3D reconstruction of the Homunculus Nebula was obtained without assuming the orientation of the orbit of the central binary. The apastron direction derived by Madura et al. (2013) projects between the two protrusions. Furthermore, the angular size of the trenches in the polar regions is very similar to the angular extent of the protrusions, and their orientations are also centred on the apastron direction.

In Figure 5 we compare the orientation of the two projections to 3D models of the massive interacting wind derived by Madura et al. (2013). The model is derived from the spatial structure seen in [Fe III] from detailed maps made with STIS (Gull et al., 2009). Multiple distorted shells have been created by wind–wind interaction during the current and previous orbits of the binary system; because of the high eccentricity ($e \approx 0.9$) the stars spend most of their orbits near apastron. The net result is a large cavity carved out in the apastron direction of the secondary star; the opening angle of this wind–wind interaction cone is strikingly similar to the azimuthal distance between the protrusions (see Figure 5). Obtained from a completely independent investigation, this comparison suggests a causal relation between the wind–wind interaction and the protrusions.

Based on this evidence for a direct influence of the interacting stellar winds on the small-scale structure of the Homunculus, we speculate that the line connecting the two protrusions defines the direction of the orbital plane, as illustrated in Figure 6. We therefore tentatively predict that the orbital plane might be tilted with respect to the equatorial plane of the Homunculus Nebula by 20 degrees. Such a misalignment between the orbital plane and axis of the Homunculus has been suggested earlier, based on the analysis of spectroscopic observations and hydrodynamical simulations (Groh et al., 2010, and references therein). However the models by Madura et al. (2013) suggest that the orbital plane appears to be closely aligned, within 10 degrees, of the Homunculus axis of symmetry. The two lobes of the Homunculus appear to be about 8 degrees out of alignment.

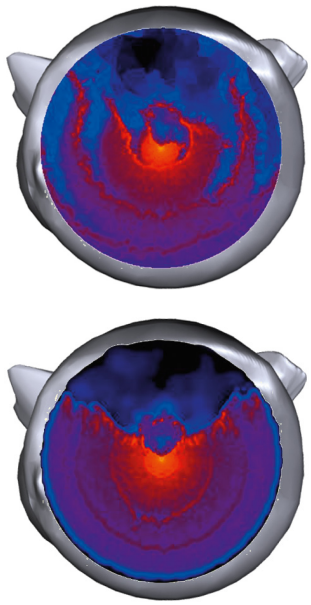

Figure 5. A comparison is shown between the opening angle of the wind–wind interaction region of the central binary star (red–blue) and the angular distance between the newly found protrusions in the Homunculus (grey). The red–blue colours depict density structures as derived by hydrodynamic simulations in the orbital plane of the binary (upper) and perpendicular to it (lower), from Madura et al. (2013). The diameter of the (grey) Homunculus section is about 6 arcseconds, while the interacting winds extend to only about 1.5 arcseconds in these images.

Based on the kinematics derived from molecular hydrogen lines observed with X-shooter and using the Shape software, several features have been revealed that are highly aligned with the orientation of the line of centres of the η Car binary system. The azimuthal angular extent and location of the features coincides with

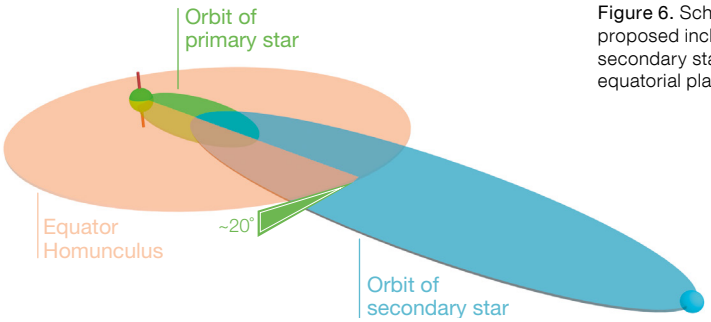

Figure 6. Schematic diagram of the proposed inclination of the orbit of the secondary star with respect to the equatorial plane of the Homunculus.

the opening angle of the conical cavity produced by the interaction of the stellar winds of the primary and secondary, previously derived by independent hydrodynamic modelling (Madura et al., 2013). We have therefore shown that the interacting winds of the central binary have had a direct impact on the surrounding Homunculus Nebulae, either briefly during the 1840's eruption, or slowly during the many orbital periods that have passed since the eruption.

Interactive and 3D printable model

We have created an interactive version of the 3D model of the Homunculus that can be accessed via Figure 5 of the original publication in Steffen et al. (2014) in PDF format. This 3D graphic is also available, as Figure 4, in this article. Furthermore, a 3D printable version in STL format is available as supplementary material to the publication[2].

Acknowledgements

W. S. acknowledges support for this project by UNAM-PAPIIT grant 101014.

References

Damineli, A. et al. 2008, MNRAS, 386, 2330
Davidson, K. & Humphreys, R. M. (eds.) 2012, *Eta Carinae and the Supernova Impostors*, Astrophysics and Space Science Library, (New York: Springer), 384
Groh, J. H. et al. 2010, A&A, 517, A9
Gull, T. R. et al. 2009, MNRAS, 396, 1308
Ishibashi, K. et al. 2003, AJ, 125, 3222
Madura, T. I. 2012, MNRAS, 420, 2064
Madura, T. I. et al. 2013, MNRAS, 436, 3820
Steffen, W. et al. 2011, IEEE Transactions on Visualization and Computer Graphics, 17, 4, 454
Steffen, W. et al. 2014, MNRAS, 442, 3316
Teodoro, M. et al. 2008, MNRAS, 287, 564

Links

[1] SHAPE software package: http://www.astrosen.unam.mx/shape
[2] Access to file for 3D printer version: http://mnras.oxfordjournals.org/content/suppl/2014/06/30/stu1088.DC1/supp.zip

Colour composite image of the star-forming complex NGC 3372, including η Carinae (lower left of centre). This image was made with the MPG/ESO 2.2-metre telescope and the Wide Field Imager by combining images in broad bands (*U, B, V* and *R*) and narrow bands (Hα and [S II]). The field of view is 33 arcminutes square (north up, east left) and the clusters Trumpler 14 and Collinder 229 can be seen to the northwest and southeast of η Car respectively. See eso0905 for more details.

The X-shooter Spectral Library (XSL) and its First Data Release

Yan-Ping Chen[1,2]
Scott C. Trager[2]
Reynier F. Peletier[2]
Ariane Lançon[3]
Alejandro Vazdekis[4,5]
Philippe Prugniel[6]
David Silva[7]
Anaïs Gonneau[3,2]
Mariya Lyubenova[2]
Mina Koleva[8]
Jesús Falcón Barroso[4]
Patricia Sánchez Blázquez[9]
C. Jakob Walcher[10]
Omar S. Choudhury[10]
Sofia Meneses-Goytia[2]

[1] NYU Abu Dhabi, Abu Dhabi, United Arab Emirates
[2] Kapteyn Astronomical Institute, University of Groningen, the Netherlands
[3] Observatoire Astronomique de Strasbourg, UMR 7550, Université de Strasbourg, CNRS, France
[4] Instituto de Astrofísica de Canarias (IAC), La Laguna, Tenerife, Spain
[5] Departamento de Astrofísica, Universidad de La Laguna, Tenerife, Spain
[6] CRAL, Observatoire de Lyon, UMR 5574, Université Lyon 1, CNRS, France
[7] National Optical Astronomy Observatory, Tucson, USA
[8] Sterrenkundig Observatorium, Ghent University, Belgium
[9] Departamento de Física Teórica, Universidad Autónoma de Madrid, Cantoblanco, Spain
[10] Leibniz-Institut für Astrophysik Potsdam (AIP), Potsdam, Germany

Stellar spectral libraries play a pivotal role in astrophysics, helping us to understand the physics of stars and build models of stellar populations in order to study distant star clusters and galaxies. Aspects of current stellar spectral libraries that require improvement are: better calibrations, more stars, higher spectral resolution and broader wavelength coverage. The X-shooter spectrograph is well suited to the task, and we are building the X-shooter Spectral Library (XSL) of more than 700 stars covering the entire Hertzsprung–Russell diagram in the wavelength range 300–2480 nm at a mean resolving power of 10 000. Here we describe the sample, observations and reduction of the data, concentrating on the flux-calibrated, telluric-corrected near-ultraviolet and optical spectra of the first 237 unique stars observed in the first year of the survey. These spectra, the first data release, are now available at http://xsl.u-strasbg.fr/.

Based on measurements of the surface temperatures, compositions, masses, and rotation from the observed depths and widths of the stellar lines, stellar spectral libraries help us to understand the physics of stars and are necessary building block to construct models of stellar populations, without which we could study neither distant star clusters nor galaxies. Trager (2012) reviewed modern stellar spectral libraries designed for stellar population synthesis modelling and identified five desiderata for future libraries:

- Good calibrations — excellent flux and wavelength calibrations and accurate and high-precision stellar atmospheric parameters are required for the best stellar population models;
- Lots of stars — a comprehensive stellar population model requires all stellar evolutionary phases for all conceivable stellar compositions;
- Moderate-to-high spectral resolution — a stellar population model should be able to model both individual stellar clusters and massive galaxies;
- Broad wavelength coverage — no single stellar evolutionary phase contributes to all wavelengths of interest, and multiple evolutionary phases contribute to different wavelengths;
- Simultaneous observations at all wavelengths of interest — stellar spectral variability, particularly in cool stars, can cause serious problems with constructing stellar population models, especially if the number of stars is small.

All of these issues led us to begin the X-shooter Spectral Library (XSL) project in 2010. X-shooter has the required simultaneous wavelength coverage (300–2480 nm in one shot through three arms), resolution ~ 10 000, can be calibrated well in both wavelength and flux (described below), and can target faint stars in a variety of environments (from the nearby Galactic Disc to the Bulge and to the Magellanic Clouds) with a variety of chemical compositions, in order to provide a truly modern stellar spectral library.

Sample selection and observations

XSL's targets were selected to cover as much of the Hertzsprung–Russell diagram (HRD) as possible. In the early semesters (P84–P85) we concentrated on cool stars lacking from current libraries, especially red supergiants and asymptotic giant branch stars in the Milky Way and the Magellanic Clouds. We also included Galactic Bulge giants to cover metal-rich stars with abundances similar to those in giant elliptical galaxies. We show the HRD of these stars as a function of metallicity in Figure 1 and the sky distribution of these stars in Figure 2.

The survey was conducted in two phases: a two-semester pilot survey and a Large Programme. The pilot survey that resulted in XSL Data Release 1 (DR1; Chen et al., 2014) was undertaken in Periods 84 (programme 084.B-0869) and 85 (programme 085.B-0751). DR1 contains X-shooter UVB and VIS arm spectra of a total of 237 unique stars, with multiple observations of some stars, in particular variable cool giants (long-period variables and Mira-type stars) to probe their spectral variability. The XSL Large Programme (programme 189.B-0925) was carried out in Periods 89–92, resulting in spectra of a total of nearly 480 unique stars. Again, a handful of cool giants was observed at multiple epochs to probe spectral variability.

In all periods, the stars were observed with the X-shooter configuration described in Table 1. This X-shooter setup gave a typical resolution ~ 7000–11 000 over the wavelength range 300–2480 nm from

Mode	Arm	Slit	λ (nm)	R
Nod	UVB	0.5″ × 11″	300–600	9100
Nod	VIS	0.7″ × 11″	600–1020	11000
Nod	NIR	0.6″ × 11″	1000–2480	8100
Stare	UVB	5″ × 11″	300–600	
Stare	VIS	5″ × 11″	600–1020	
Stare	NIR	5″ × 11″	1000–2480	

Table 1. X-shooter observing modes for XSL.
Note: Resolution $R = \lambda/\Delta\lambda$ is the nominal spectral resolution given by the X-shooter manual; the actual resolution in the UVB arm ranges from 7000–9500.

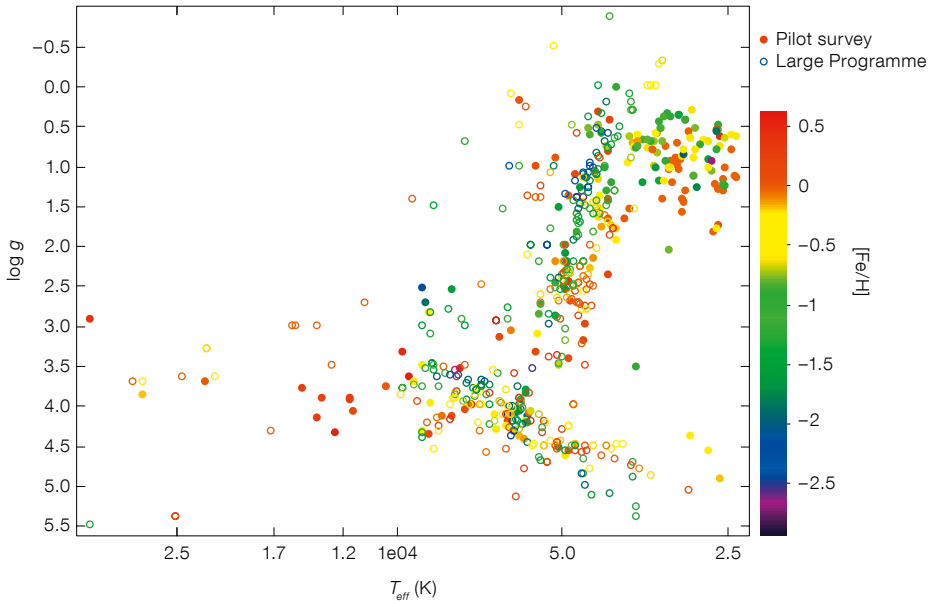

Figure 1. (Above) The Hertzsprung–Russell diagram of XSL stars (surface gravity log *g* as a function of effective temperature T_{eff}), colour-coded by metallicity [Fe/H]. The stars of the first data release (Chen et al., 2014) are indicated by filled circles. The remaining stars are indicated by open circles.

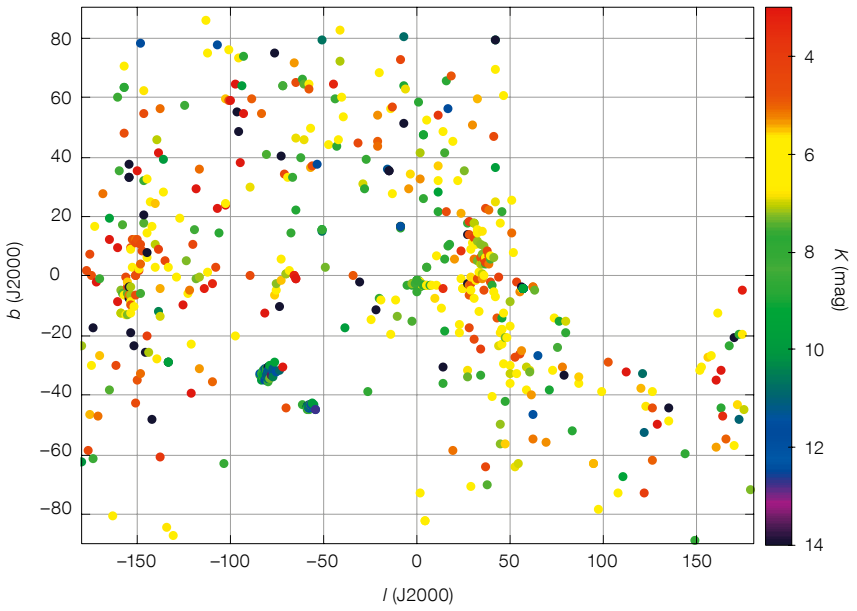

Figure 2. (Below)The sky distribution of XSL stars in Galactic coordinates. Points are coloured by their 2MASS *K*-band magnitudes.

the narrow-slit "nodding" observations and good flux calibration from the wide-slit "staring" observations. The programme was designed to fill any gaps in the observing queue, and therefore the observations were typically taken during poor seeing and thick cloud conditions; this however did not affect the relative flux calibration precision (see below).

Data reduction

The data reduction of the near-ultraviolet and optical spectra from the pilot survey was performed with the public release of the X-Shooter pipeline version 1.5.0, following the standard steps described in the X-shooter pipeline manual[1] up to the production of two-dimensional spectra, including bias and/or dark correction, flat-fielding, geometric correction, wavelength calibration and (when necessary) sky subtraction. A number of issues were discovered during the pipeline reduction process, which required further processing steps. We give details about two of the most significant of these steps here; more details can be found in Chen et al. (2014).

Telluric correction

Ground-based observations are always subject to contamination from the Earth's atmosphere. In the visible and near-infrared portions of the spectrum, water vapour, molecular oxygen, carbon dioxide and methane generate strong absorption features that originate in the Earth's atmosphere and are referred to as telluric features. Corrections for telluric contamination therefore are important for the XSL spectra in the VIS and NIR arms.

We used "telluric standard star" observations taken as part of the standard X-shooter calibration plan directly after each of our science observations as a basis for telluric correction of our optical data. These stars are typically B2–A0 dwarfs, whose intrinsic spectra contain only H and He absorption lines on top of nearly pure blackbody spectra. We determined the telluric absorption spectrum at the time of observation of each of these stars by dividing the observed spectrum by a model of the star's intrinsic spectrum. We found that the telluric absorption lines changed strength on timescales shorter than the "long" exposure time (> 90 seconds) of faint XSL stars and the total overhead time of ~ 900 seconds, resulting in an imperfect telluric correction. In addition, small changes in spectral resolution and wavelength zero-point occurred even between successive observations. To optimise the telluric correction, we therefore built a library of telluric spectra, in which 152 telluric standard stars were carefully wavelength-calibrated and had their intrinsic spectra modelled and removed.

We developed a principal-component-analysis- (PCA) based method that can quickly and precisely perform telluric corrections for warm stars in XSL. Figure 3 shows the first six principal components from the bottom to top. We

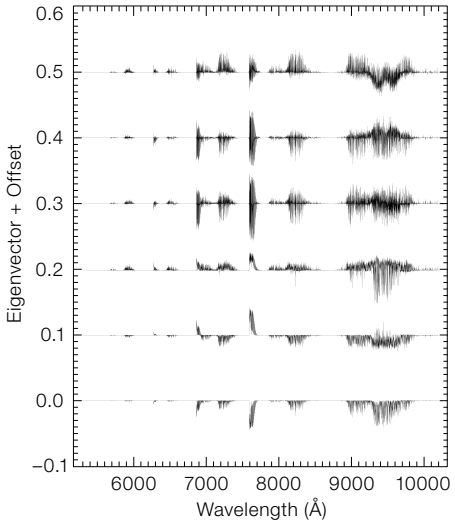

Figure 3. The first six principal components of the telluric library. The eigenvalues decrease from the bottom to the top of this figure (i.e., the first and largest eigenvector is the lowest). The eigenvectors have been offset for display purposes.

found that the first two primary components of our telluric library have a clear physical meaning: the first component presents the mean telluric spectrum of the library; the second component separates the contribution of most of the water vapour features from the O_2 features. We used the first 40 principal components to reconstruct the transmission of each star.

First the science spectrum was normalised, then the reconstructed transmission spectrum was built by projecting the mean-subtracted, normalised science spectrum onto the modified principal components and summing these projections. Telluric correction was finally performed by dividing the spectrum of the programme star by the reconstructed transmission. Figure 4 shows an example of the telluric correction of the K7IV star HD 79349. We found that telluric correction by PCA reconstruction does a good job for both early-type stars and some late-type stars, as this method works better for stars with simpler continua and high signal-to-noise ratios. Cool stars, such as carbon stars, have strong and sharp molecular bands. Tracing each absorption bandhead to apply the PCA method is therefore difficult for these stars, because some molecular bands occur exactly at the same wavelengths as the telluric absorption regions. Therefore we used the transmission spectrum taken from the telluric library closest in time to the programme star to correct the telluric absorption for all carbon stars, long period variable (LPV) stars and most of the M stars.

Flux and wavelength calibration

Knowledge of the spectral energy distribution of stars allows us to compute synthetic photometry, an important ingredient to compare with catalogues of stellar photometry and to combine stellar spectra together with the correct weights as a function of wavelength in stellar population models. Flux calibration is therefore critical for a spectral library in order to recover the overall spectral energy distribution of each star. Nearly all XSL stars, except the brightest ($K < 5$ mag), have both narrow-slit observations, to achieve high resolution, and a wide-slit observation, to preserve the total flux. The brightest stars would have saturated the detectors much too quickly in wide-slit mode and therefore were not observed in this mode.

We derived the atmospheric extinction curve of X-shooter in the pilot survey in the UVB and VIS arm using a number of flux-standard stars (BD+17 4708, GD 71, GD 153, EG 274, Feige 110, LTT 3218, and LTT 7987). Response curves for individual stars were generated from the chosen flux-standard star observed closest in time. A final flux calibration was carried out on the narrow-slit observations using the shape of wide-slit observations to avoid flux losses. We used

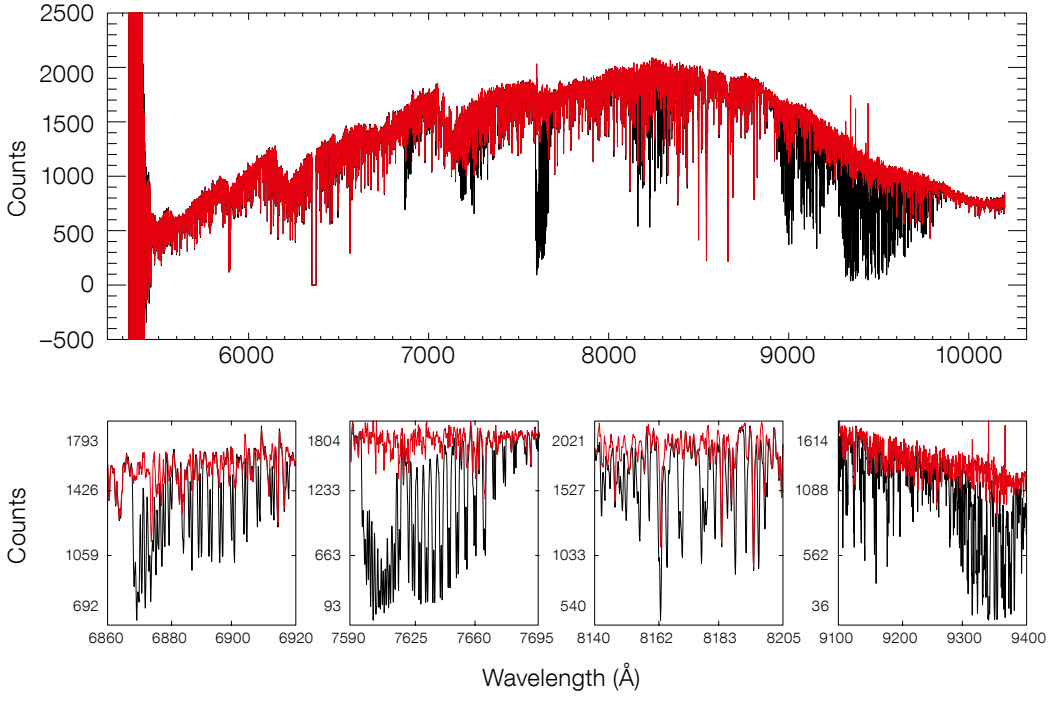

Figure 4. Spectrum of HD 79349 (K7IV) before (black) and after (red) telluric correction in the VIS arm, using the PCA reconstruction method described in the text. The lower panels show four zoomed-in regions to demonstrate the corrections in detail. The spikes around 935 nm are residuals after telluric correction.

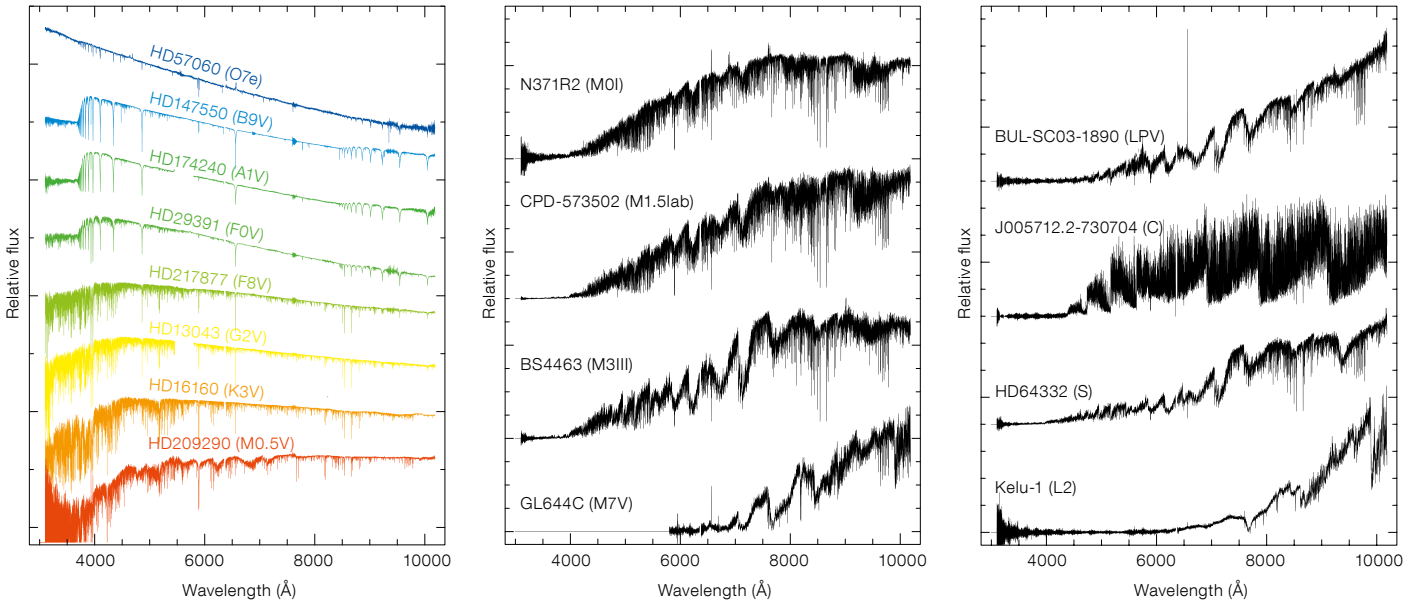

Figure 5. Left: The classic OBAFGKM temperature sequence as represented in XSL, shown in (relative) log F_λ flux units. Gaps around 570 nm indicate strong dichroic features between the X-shooter UVB and VIS arms. Middle: A sequence of M stars from XSL sorted by spectral type. The flat region in the star GL644C indicates a region with a very low signal-to-noise ratio. Right: A sample of LPV, C, S, and L stars in XSL.

the wide-slit exposure paired with each flux-calibrated, narrow-slit spectrum to achieve this. Typical flux-calibrated XSL spectra are shown in Figure 5.

We measured the spectral resolution and line shifts of our X-shooter spectra to check the wavelength calibration of our observations. We fitted 212 spectra of F, G, K stars with the synthetic library of Coelho et al. (2005) using the ULySS package[2] (Koleva et al., 2009) to determine the above properties. As shown in Figure 6, the instrumental (velocity) resolution in the UVB arm ranged from 13.3 to 18.1 km s^{-1} (velocity dispersion, σ), corresponding to a resolution of 9500–7000. We have corrected our XSL data in the UVB arm to the (air) restframes using the line-shift relation shown in Figure 6. In the VIS arm, the instrumental resolution was constant at 11.6 km s^{-1} (i.e., R = 10 986), very close to the resolution of 11 000 given by the X-shooter manuals.

Synthetic photometry comparison

We calculated synthetic colours on the Johnson–Cousins *UVBRI* and Sloan Digital Sky Survey (SDSS) photometric systems for the XSL stars and compared these colours with published values to check the reliability of our flux calibration. By comparing the calculated synthetic *B–V*, *U–B*, *R–I*, and *V–I* colours of the XSL-sample with the NGSL library[3] (Gregg et al., 2006) and observed colours from the Bright Star Catalogue (Hoffleit et al., 1983; Hoffleit & Jaschek, 1991) we found good agreement between XSL sample and literature stars, with offsets < 0.02 mag in all colours and scatters ranging from 0.07 mag in *U–B* to 0.02 mag in *R–I*. Since there are few literature stars that have the SDSS colours in common with our sample, we used the model colours computed by Lenz et al. (1998) as a rough check. In general, the agreement between the models and data was very good.

Comparison with literature spectra

As a further check, we made a direct comparison of the final XSL spectra with other libraries. The first year of XSL (DR1) had 77 stars in common with NGSL, 40 stars in common with the MILES (Sánchez-Blázquez et al., 2006) stellar spectral library[4], 34 stars in common with the ELODIE (Prugniel & Soubiran, 2001, 2004; Prugniel et al., 2007) spectral library[5], 26 stars in common with the IRTF (Rayner et al., 2009) spectral library[6] and 25 stars in common with the CaT (Cenarro et al., 2001) spectral library[7]. For each comparison, we convolved the comparison spectrum and XSL to the same intrinsic resolution, matched the continua, and measured the fractional difference between these spectra in telluric-free regions.

Comparing the XSL spectra with two higher-resolution spectral libraries, UVES POP (Bagnulo et al., 2003)[8] and ELODIE, we found that the typical residual between XSL and UVES POP is 2–4 % in relative flux after convolving the UVES POP spectra to the XSL resolution, and the typical residual between XSL and ELODIE is 2–6 % in relative flux after similarly convolving ELODIE to the XSL resolution. We found very good agreement in the line shapes and depths between XSL and the two higher-resolution libraries for both warm and cool stars. Comparison of XSL with the intermediate-resolution spectral library MIUSCAT (a combination of MILES, Indo–U.S.[9] and CaT; Vazdekis et al., 2012) showed a typical flux residual between XSL and MIUSCAT of 2 %. Comparison of XSL with the lower-resolution spectral library NGSL also showed good agreement: the typical relative flux residual between XSL and NGSL was 1 % over the common wavelength 320–1000 nm after removing the continuum shapes.

Applications of XSL

XSL is currently being applied to a number of studies, from the study of individual

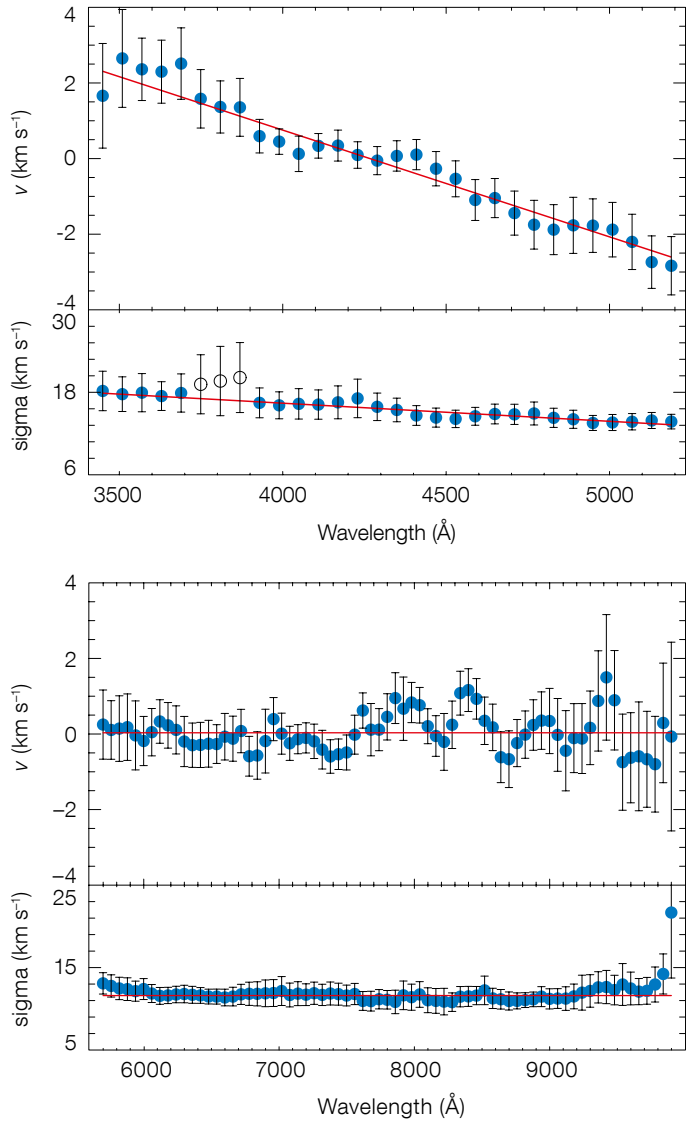

Figure 6. Average line-spread functions for the XSL DR1 FGK stars (212 spectra) in the X-shooter UVB (upper panel) and VIS (lower panel) arms. In each arm, the top panel shows the residual shift of the spectra (blue dots). The bottom panel shows the measured instrumental resolution (in velocity units). The error bars are the standard deviation in each wavelength bin. A simple first-order polynomial fit (red lines) of the line-spread function is given in each panel. The three open circles show the region where two different flat-field lamps are used simultaneously in the UVB arm, which may result in larger uncertainties.

stars (e.g., Davies et al., 2013), to use as spectral templates in determining the stellar velocity dispersions of intermediate-redshift early-type galaxy lenses for gravitational lensing studies (e.g., Spiniello et al., 2011) and to stellar population models. Chen (2013) made the first XSL stellar population models with the XSL DR1 spectra, which demonstrate a rich set of spectral features at a spectral resolution of 7000 over the spectra range 320–1000 nm. Gonneau et al. (2013) compared stellar atmosphere models of carbon stars to XSL VIS–NIR spectra to estimate effective temperatures, surface gravities, C/O ratios and extinctions of such stars.

Future perspectives

XSL will provide a benchmark library for stellar population studies in the near-ultraviolet, optical, and near-infrared in the era of James Webb Space Telescope and the Extremely Large Telescopes; for stellar atmosphere studies, especially for cool (super)giants; telluric corrections; and many other topics. XSL is, however, incomplete in a few critical areas, and these will be the topic of coming work by our team and others. In particular, XSL contains only a handful of M dwarf stars, critical for studies of the low-mass region of the initial mass function in integrated stellar populations. The X-shooter archive contains a reasonable number of M (and cooler) dwarfs, which our team will analyse after the XSL data reduction is complete. Furthermore, XSL is missing hot, very massive (young) stars, hotter than about B0 or O9. The lack of these stars compromises our ability to make stellar population models of very young populations. This lack will be addressed in the coming years, partly through our own efforts and partly through the efforts of others who specialise in observing such stars.

References

Bagnulo, S. et al. 2003, The Messenger, 114, 10
Cenarro, A. J. et al. 2001, MNRAS, 326, 959
Chen, Y. P. 2013, PhD Thesis, University of Groningen
Chen, Y. P. et al. 2014, A&A, 565A, 117
Coelho, P. et al. 2005, A&A, 443, 735
Davies, B. et al. 2013, ApJ, 767, 3
Gonneau, A. et al. 2013, in SF2A-2013, Proceedings of the Annual Meeting of the French Society of Astronomy and Astrophysics, eds. Cambresy, L. et al., 233
Gregg, M. D. et al. 2006, in *The 2005 HST Calibration Workshop: Hubble After the Transition to Two-GyroMode*, eds. Koekemoer, A. M., Goudfrooij, P. & Dressel, L. L., 209
Koleva, M. et al. 2009, A&A, 501, 1269
Lenz, D. D. et al. 1998, ApJS, 119, 121
Prugniel, P. & Soubiran, C. 2001, A&A, 369, 1048
Prugniel, P. & Soubiran, C. 2004, arXiv: Astrophysics e-prints
Prugniel, P. et al. 2007, arXiv: Astrophysics e-prints
Rayner, J. T., Cushing, M. C. & Vacca, W. D. 2009, ApJS, 185, 289
Sánchez-Blázquez, P. et al. 2006, MNRAS, 371, 703
Spiniello, C. et al. 2011, MNRAS, 417, 3000
Trager, S. C. 2012, in *International Workshop on Stellar Libraries*, eds. Prugniel, P. & Singh, H. P., Astr. Soc. India Conf. Ser., 6, 1
Vazdekis, A. et al. 2012, MNRAS, 424, 157
Vernet, J. et al. 2011, A&A, 536, A105

Links

[1] X-shooter pipeline manual: http://www.eso.org/sci/software/pipelines/
[2] ULySS spectroscopic analysis package: http://ulyss.univ-lyon1.fr/
[3] Next Generation Stellar Library (NGSL): http://archive.stsci.edu/prepds/stisngsl/
[4] MILES stellar library: http://miles.iac.es/
[5] ELODIE spectral library: http://www.obs.u-bordeaux1.fr/m2a/soubiran/elodie_library.html
[6] IRTF spectral library: http://irtfweb.ifa.hawaii.edu/~spex/IRTF_Spectral_Library/
[7] CaT stellar library: http://miles.iac.es/pages/stellar-libraries/cat-library.php
[8] UVES POP library: http://www.eso.org/sci/observing/tools/uvespop.html
[9] Indo–U.S. library: http://www.noao.edu/cflib/

Catching Stellar Mergers at Work with the Very Large Telescope Interferometer

Florentin Millour[1]
Eric Lagadec[1]
Orsola de Marco[2]
Dipankar P. K. Banerjee[3]
Djamel Mékarnia[1]
Alain Spang[1]
Olivier Chesneau[1†]

[1] Laboratoire Lagrange, UMR 7293, Univ. Nice Sophia-Antipolis, CNRS, Observatoire de la Côte d'Azur, Nice, France
[2] Department of Physics & Astronomy, Macquarie University, Sydney, Australia
[3] Astronomy & Astrophysics Division, Physical Research Laboratory, Navrangpura, India

The two Very Large Telescope Interferometer (VLTI) instruments AMBER and MIDI were used to study the close environment of two post-merger stellar systems: the R Coronae Borealis star V854 Cen and the red nova V838 Mon. The observations reveal the presence of flattened dusty structures in the core of both objects, which are very likely discs. This finding confirms that the merger of two stars can lead to the formation of a disc.

With the advent of optical interferometry, the close environments around many evolved stars have been resolved (see Chesneau, 2011). Companions encompassing a large range of mass, from stellar objects to Jovian-mass planets, are suspected to strongly influence the ejecta when a low- to intermediate-mass star reaches the asymptotic giant branch, or even as early as the red giant branch (de Marco, 2009). This interaction can potentially influence dramatically the fate of the star, leading to poorly known evolutionary paths, affecting the timescales of the different stellar evolutionary stages, to the extent that the product bears little similarity to, for example, the timescale and chemistry involved for the evolution of a single, naked star (Frankowski & Jorissen, 2007).

Interferometry in the near- and mid-infrared is the best tool with which to probe the close environment of evolved stars. Indeed, ultra-sharp images of these environments can be made, probing the inner hundreds of astronomical units, exactly where discs and companions occur and are intimately related to the evolution of the stars. Interferometry is ideally suited to resolve discs in the core of nebulae around stars of a range of masses from low to high. Here we present a snapshot of two such objects — the R Coronae Borealis (RCB) star V838 Cen and the eruptive variable V838 Mon — highlighting the seminal contribution of the astronomer Olivier Chesneau, who passed away earlier this year.

The R Coronae Borealis stars are hydrogen-deficient carbon-rich supergiants, best known for their spectacular declines in brightness at irregular intervals (De Marco et al., 2002). Two evolutionary scenarios have been suggested for producing an RCB star: a double-degenerate merger of two white dwarfs (WD) or a final helium-shell flash in a planetary nebula central star. V854 Cen has a large hydrogen content and polycyclic aromatic hydrocarbons (PAHs) detected in the mid-infrared, making it an unusual member of its class. This star also has a fast wind which reaches several hundreds of km s^{-1} (Clayton et al., 2013; Kameswara Rao & Lambert, 1993). Kameswara Rao & Lambert (1993) provided strong arguments that V854 Cen may be surrounded by a bipolar nebula, extending up to about 2 arcseconds, as revealed by its C II extended emission (Clayton & Ayres, 2001).

V838 Mon is a nova-like object that erupted in 2002 (reaching $V = 6.8$; Bond et al., 2003). The eruption was unlike classical novae because the effective temperature of the object dropped and the spectral type evolved to that of a very late L-type supergiant (Loebman et al., 2014). The mid-infrared flux of V838 Mon increased by a factor of two between 2004 and 2007, suggesting that new dust was forming in the expanding ejecta of the outbursts (Wisniewski et al., 2008). The expanding ejecta engulfed a companion close to the central source (Bond, 2006), seen as a faint, blue component in the spectrum, and Tylenda et al. (2005) argued that the pre-outburst spectral energy distribution (SED) is well matched by a pair of early main-sequence stars (B3V + B1.5V or B4V + A0.5V), making V838 Mon a triple system (main star + subsolar merging star + B3V companion).

The 2002 eruption has been interpreted as the merger of a star of ~ 8 $M_{\odot}$ with a subsolar mass star (Tylenda & Soker, 2006).

V838 Mon is embedded in a dense, large-scale environment that was lit up by the light echoes resulting from the 2002 eruption (Bond et al., 2003), and potentially contaminates observations of the central star. High angular resolution studies with a small field of view of a few arcseconds are an asset in isolating the central regions from the extended dusty cloud. A great advantage of optical interferometry studies is thus to isolate the measurements from the extended environment.

Observations

VLTI observations of both targets were obtained with the low spectral resolution mode of AMBER ($R = 35$), the three-telescope combiner (Petrov et al., 2007). The observations were performed with the 1.8-metre Auxiliary Telescopes (ATs) using the compact (baseline, B ≤ 35 m) and long configurations (B ≤ 140 m). Full details can be found in Chesneau et al. (2014a) for V854 Cen and Chesneau et al. (2014b) for V838 Mon. Near-infrared observations were obtained with AMBER, similar to those for R Corona Borealis, using three ATs and the compact baselines. Mid-infrared interferometric data were also obtained for V838 Mon with the two-telescope recombiner MIDI (Leinert et al., 2004), which had a field of view ~ 0.3 arcseconds, identical to the near-infrared field of view, thanks to the use of the Unit Telescopes.

V854 Cen was also observed with the mid-infrared imager VISIR (Lagage et al., 2004) with a pixel scale of 0.075 arcseconds and field of view of 19.2 by 19.2 arcseconds through the SiC filter ($\lambda = 11.65$ µm, width 2.34 µm). Figure 1 displays the VISIR image, showing a clearly extended nebulosity around the central star.

Modelling the visibilities

The interferometer data do not directly provide an image of the sources, and we used an in-house tool called fitOmatic

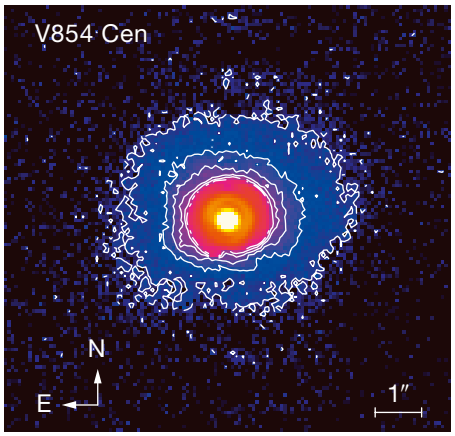

Figure 1. A VISIR 11.65 µm image is shown of V854 Cen with enhanced contours of the outer regions. The extended nebulosity can be seen in blue and purple.

(Millour et al., 2009) to fit simple geometric components. These fits provide the poor man's images displayed in this article (Figures 2 and 3), at an unmatched spatial resolution. The fitOmatic tool uses a set of simple (uniform disc, Gaussian, etc.) and less simple ("pinwheel", rotating and expanding disc, etc.) chromatic models that can be combined together to form more complex objects. The model is matched to the data using least squares, with special care taken for the phases (closure phase and differential phases). In order to fit the interferometric data (i.e. minimise the least squares), it uses a simulated annealing algorithm, leading to the best-match solutions shown in this paper.

V854 Cen

The best-match model for the compact array data has two components: an unresolved uniform disc ($\Theta < 2.5$ milliarcseconds [mas], star component), and a flattened Gaussian (shell component) with a full width at half maximum (FWHM) of the minor axis of 8 ± 1 mas, and major axis 11 ± 3 mas. The orientation of the major axis is 126 ± 29° (Chesneau et al., 2014a). The long-array data shows that the star is unresolved ($\Theta < 1.0$ mas). Figure 2 shows the fit of the AMBER data by the geometrical model.

Given that the closure phase signal observed on V854 Cen is null within the error bars, a companion star, if any, would not have a flux exceeding 3 % of the total flux, i.e. well below the detection limit down to a typical spatial resolution of 10 mas. A model with a fully clumped uniform shell that contained up to 30 clumps was used to determine whether the high *H*-band visibilities could be explained this way, and indeed it does. However, such a model contains too many components and can only be loosely constrained. The position angle (PA) of the outer contours of the VISIR 11.65 µm images is only marginally consistent with that derived with AMBER, so it is possible that the spatial structure of the mass loss of V853 Cen is inhomogeneous and randomly variable.

V838 Mon

The MIDI dispersed visibilities were translated into the simplest possible geometrical *ad hoc* model — a Gaussian brightness distribution, as described in Leinert et al. (2004). The resulting fits shown in Figure 3 depict the general appearance of the mid-infrared structure. The semimajor and semiminor axes of the drawn ellipses represent the half-width at half maximum of the Gaussian. The extent of that structure increases from a FWHM of 25 mas at 8 µm to 70 mas at 13 µm, with a high flattening ratio. The major axis is oriented at a PA close to 10 ± 30°. The 2013 short-baseline AMBER visibilities are all very close to unity in the band centres at 1.7 µm and 2.2 µm and are consistent with a completely unresolved object. The

Figure 2. Bellow: Geometrical models from fitOmatic of the environment of V854 Cen at 2.5 µm. Upper right panel: Combined *H*- (blue) and *K*- (red) band interferometric visibilities obtained with AMBER compared with the signal from the polychromatic geometrical modelling. Lower right panel: Closure phases in the *H*- and *K*-bands plotted with the same colours.

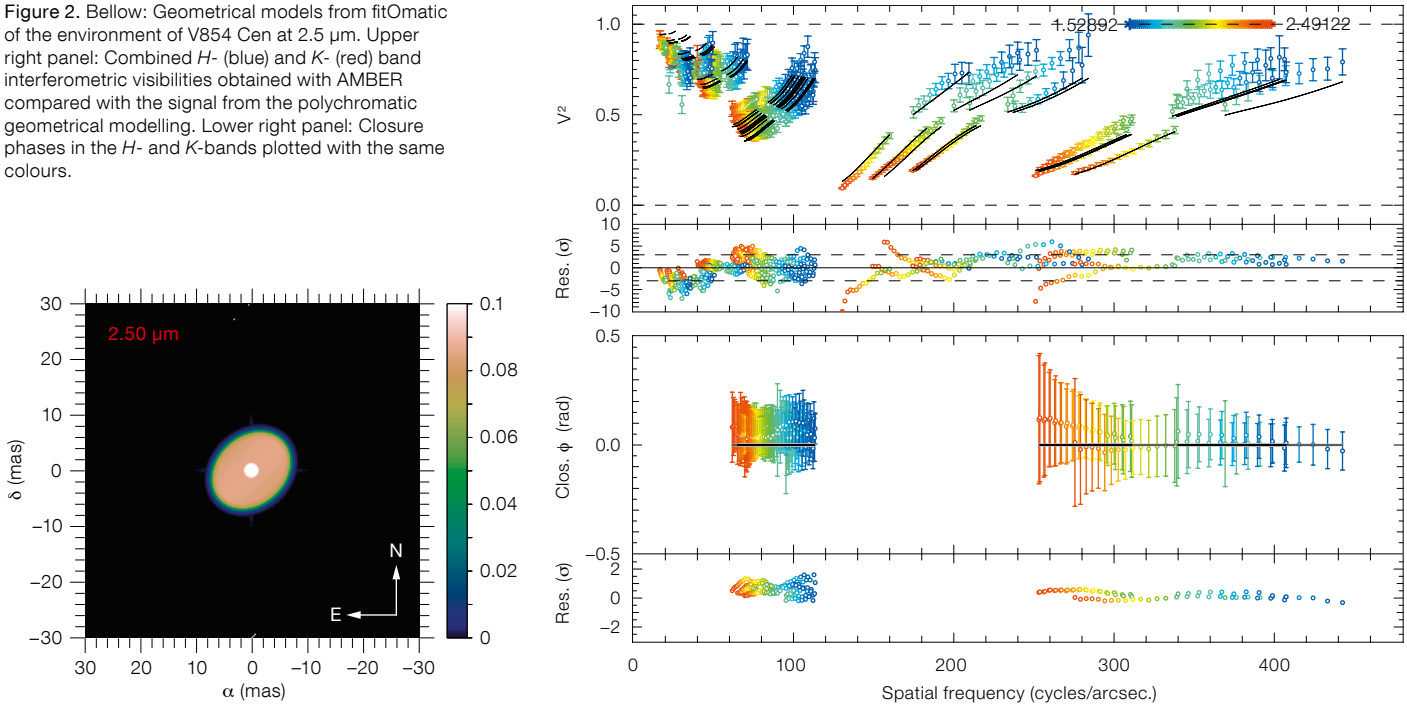

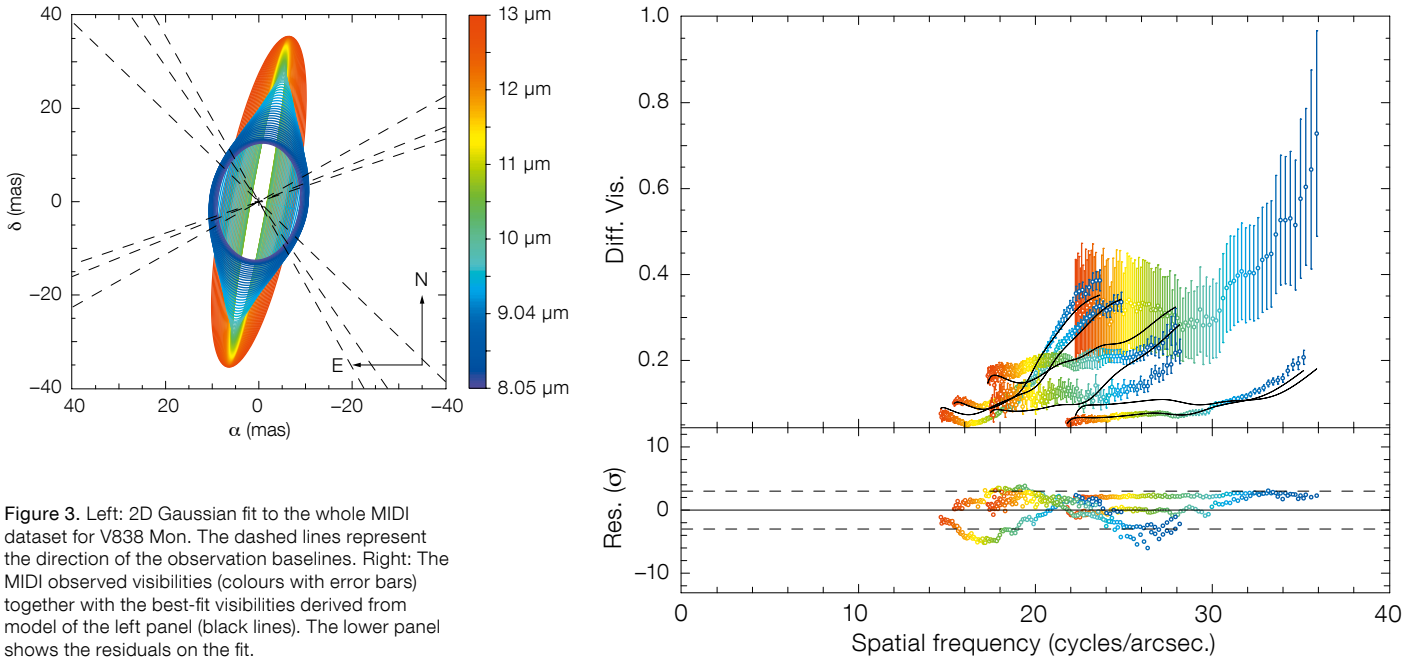

Figure 3. Left: 2D Gaussian fit to the whole MIDI dataset for V838 Mon. The dashed lines represent the direction of the observation baselines. Right: The MIDI observed visibilities (colours with error bars) together with the best-fit visibilities derived from model of the left panel (black lines). The lower panel shows the residuals on the fit.

visibilities as a function of wavelength of the *H*- and *K*-bands decrease relative to the band centres (1.7 μm and 2.2 μm) indicative of an object whose shape changes as a function of wavelength.

We again used the fitOmatic package to derive an angular diameter assuming a uniform-disc model around 2.2 μm. A diameter of 1.15 ± 0.20 mas was found, significantly smaller than that published by Lane et al. (2005). Since the AMBER closure phases are all equal to zero within the error bars, we can constrain the flux of a hypothetical companion star in addition to the central merger. Our conclusion was that there is a difference of at least 4 mag between the primary and the companion. The AMBER observations do not exclude the presence of the companion, but place important constraints on its near-infrared contribution to the spectral energy distribution.

Implications

V854 Cen

A moderately flattened dusty environment around V854 Cen was discovered from the VLTI AMBER observations. This sheds new light on the evolutionary scenarios that have been suggested for the production of RCB stars: the double-degenerate merger of two white dwarfs, which may lead to an axis of symmetry that promotes equatorially enhanced mass-loss and discs, or the final helium-shell flash in a planetary nebula central star, which may retain a central symmetry and promote no disc (Clayton et al., 2011).

The evidence for distributed dust emission suggests a disc that is possibly the relic of a past event, or that the observed spatial distribution reflects a field of randomly launched clumps in free fall around the central star, perhaps constantly replenished by the central star. Comparison can be made with the Be stars (Rivinius et al., 2013), for which the fast rotation of the central star together with its pulsational properties triggers the formation of a dense circumstellar disc. The RCB stars are known to be slow rotators, and the emission lines of V854 Cen are unresolved ($\lesssim$ 20 km s^{-1}; Kameswara Rao & Lambert, 1993). V854 Cen has a well-known single-pulsation period (43.2 days) whose phase is related to the formation of the dust (Crause et al., 2007). Convection may also contribute to the launching process of the dust clumps, as in cool supergiant stars.

The polarisation properties of V854 Cen are similar to (albeit weaker than) those of the intermediate-luminosity red transient (ILOT) V4332 Sgr (Kaminski & Tylenda 2013). ILOTs are outbursts with energies intermediate between those of novae and supernovae, examples of which are V838 Mon. If the merger scenario for the RCBs applies, then they too may be in the ILOT range if observed at the time of the merger. Two 0.5 $M_{\odot}$ WDs will deliver quite a substantial amount of gravitational energy ($\lesssim 5 \times 10^{49}$ ergs), more than would be the case for a main-sequence star merger, therefore they may cluster in the upper region of the ILOT locus on the energy–time diagram. The stellar expansion that results would make the object a giant, as is the case for ILOTs.

V838 Mon

The size of the dusty flattened structure discovered by MIDI around V838 Mon is distributed between 150 and 400 au from the star. This is also in fair agreement with the spectropolarimetric measurements reported by Wisniewski et al. (2003) interpreted as scattering by a disc with a major axis at a PA of 37°. The supergiant has decreased in angular size by ~ 40 % in around ten years since the measurements of Lane et al. (2005). The linear radius is now estimated to be 750 ± 200 $R_{\odot}$ (3.5 ± 1.0 au) and the diameter decrease means the star's photosphere

has shrunk during the intervening period at an approximate rate of 1 km s^{-1}.

The most likely hypothesis is that the flattened structure is simply the relic of the large dust formation event that was a consequence of the merging of the two stars (Wisniewski et al., 2008). The ejecta velocity was low at the time of outburst — less than 200 km s^{-1} — as derived from P-Cygni profiles by Lynch et al. (2004). In the ten years since the outburst, ejected material would not have travelled beyond 400 au. The picture revealed by interferometry of V838 Mon as of today is the following: it is now slowly becoming an anonymous red supergiant, surrounded by a flattened, probably transitory, dusty environment extending up to several hundreds of au.

Conclusions

The VLTI is the ideal tool with which to study such objects, thanks to its very high angular resolution. These observations have enabled us to study the close circumstellar environment of post-merger stellar systems. The observations of V838 Mon and V854 Cen confirm, for the first time directly, that the merger of two stars can lead to the formation of a disc.

This work has implications for the formations of bipolar nebulae. Indeed the presence of dense material close to the equatorial plane of the systems decelerates a wind or a fireball in these directions, leading to a bipolar outflow. These disc-like structures could also affect dust evolution, as dust evolves differently in a cooler and denser environment (disc) than the surroundings.

Remembering Olivier Chesneau

The work described here forms the final published work of Olivier before he passed away. He wrote the two papers describing the VLTI observations of V854 Cen and V838 Mon while he was in hospital.

Olivier Chesneau made wide-ranging contributions to the VLTI and high resolution astronomy. His results were widely publicised and he was awarded the 2012 Michelson Prize of the International Astronomical Union and the Mount Wilson Institute for major contributions in stellar astrophysics made with long-baseline interferometry. He was directly involved in the MIDI instrument and, through many observing programmes, with AMBER. He was part of the VLT SPHERE Guaranteed Time Observing programme and was involved with the second generation VLTI MATISSE instrument consortium. He also worked in the Jean-Mariotti Center (JMMC) as Principal Investigator of the Calibration Group. Olivier organised the VLTI school in Porquerolles in April 2010 and was a co-organiser of the interferometry school in Barcelonnette in the autumn of 2013. His enthusiasm, curiosity, and passion will be missed by many.

References

Bond, H. E. et al. 2003, Nature, 422, 405
Bond, H. E. 2006, ATel, 966, 1
Chesneau, O. 2011, in *Asymmetric Planetary Nebulae 5 Conference*, arXiv: 1010:1081
Chesneau, O. et al. 2014a, A&A, 569, 4
Chesneau, O. et al. 2014b, A&A, 569, L3
Clayton, G. C. & Ayres, T. R. 2001, ApJ, 560, 986
Clayton, G. C. et al. 2011, ApJ, 743, 44
Clayton, G. C., Geballe, T. R. & Zhang, W. 2013, AJ, 146, 23
Crause, L. A., Lawson, W. A. & Henden, A. A. 2007, MNRAS, 375, 301
De Marco, O. et al. 2002, AJ, 123, 3387
De Marco, O. 2009, PASP, 121, 316
Frankowski, A. & Jorissen, A. 2007, Baltic Astron., 16, 104
Kameswara Rao, N. & Lambert, D. L. 1993, AJ, 105, 1915
Kaminski, T. & Tylenda, R. 2013, A&A, 558, A82
Lagage, P. O. et al. 2004, The Messenger, 117, 12
Lane, B. F. et al. 2005, ApJ, 622, L137
Leinert, C. et al. 2004, A&A, 423, 537
Loebman, S. R. et al. 2014, ApJ, submitted
Lynch, D. K. et al. 2004, ApJ, 607, 460
Millour, F. et al. 2009, A&A, 507, 317
Petrov, R. G. et al. 2007, A&A, 464, 1
Rivinius, T., Carciofi, A. C. & Martayan, C. 2013, A&A Rev., 21, 69
Tylenda, R. & Soker, N. 2006, A&A, 451, 223
Wisniewski, J. P. et al. 2003b, ApJ, 588, 486
Wisniewski, J. P. et al. 2008, ApJ, 683, L171

NASA and The Hubble Heritage Team (AURA/STScI)

Hubble Space Telescope Advanced Camera for Surveys (ACS) image of the light echoes around V838 Mon observed in 2004, two years after the outburst. Broadband ACS images in F435W (*B*), F606W (*V*), F814W (*I*) were combined for this colour composite. See heic0405a for details.

STREGA: STRucture and Evolution of the GAlaxy with the VST

Marcella Marconi[1]
Ilaria Musella[1]
Marcella Di Criscienzo[1,2]
Michele Cignoni[3]
Massimo Dall'Ora[1]
Giuseppe Bono[4]
Vincenzo Ripepi[1]
Enzo Brocato[2]
Gabriella Raimondo[5]
Aniello Grado[1]
Luca Limatola[1]
Giuseppina Coppola[1]
Maria Ida Moretti[1,6]
Peter B. Stetson[7]
Annalisa Calamida[2,3]
Michele Cantiello[5]
Massimo Capaccioli[8]
Enrico Cappellaro[9]
Maria-Rosa L. Cioni[10,11]
Scilla Degl'Innocenti[12]
Domitilla De Martino[1]
Alessandra Di Cecco[2,13]
Ivan Ferraro[2]
Giacinto Iannicola[2]
Pier Giorgio Prada Moroni[12]
Roberto Silvotti[14]
Roberto Buonanno[4,5]
Fedor Getman[1]
Nicola R. Napolitano[1]
Luigi Pulone[2]
Pietro Schipani[1]

[1] INAF-Osservatorio Astronomico di Capodimonte, Naples, Italy
[2] INAF-Osservatorio Astronomico di Roma, Italy
[3] Space Telescope Science Institute, Baltimore, USA
[4] Dipartimento di Fisica, Università degli Studi di Roma-Tor Vergata, Italy
[5] INAF-Osservatorio Astronomico di Teramo, Italy
[6] INAF-Osservatorio Astronomico di Bologna, Italy
[7] NRC-Herzberg, Dominion Astrophysical Observatory, Victoria, Canada
[8] Università "Federico II", Naples, Italy
[9] INAF-Osservatorio Astronomico di Padova, Italy
[10] University of Hertfordshire, Hatfield, UK
[11] Leibnitz-Institut für Astrophysik Potsdam, Germany
[12] Università "E. Fermi", Pisa, Italy
[13] Agenzia Spaziale Italiana Science Data Center (ASDC), Frascati, Italy
[14] INAF-Osservatorio Astrofisico di Torino, Pino Torinese, Italy

STREGA (STRucture and Evolution of the Galaxy) is an ongoing VLT Survey Telescope Guaranteed Time survey, covering an area of about 150 square degrees, aimed at investigating the mechanisms of formation and evolution of the Galactic Halo. The project is organised into two parts: a core programme to search for the signatures of interaction between selected stellar systems and the Galactic Halo and a complementary part focussed on the southern portion of the Fornax Stream. The basis is the use of variable stars (RR Lyrae and long period variables) and main sequence turn-off stars as tracers of stellar overdensities. Observations in *g,r,i* bands, with additional filters, *u*, Strömgren *v* and Hα for selected fields, will allow investigation of the properties of Halo white dwarfs and interacting binaries. We present an overview of the survey and some first results, in particular for the region centred on Omega Centauri.

Scientific context

The study of the Milky Way (MW) and its satellite galaxies is crucial for our understanding of the formation and evolution of galaxies through their interaction with the environment. Several authors (Marconi et al. [2014] and references therein) have shown that the outer regions of the Galactic Halo appear quite clumpy, with a number of observed stellar overdensities, supporting theories based on the hierarchical formation of structures in a cold dark matter cosmological scenario. The most spectacular example of these phenomena is the observed merging of the Sagittarius dwarf spheroidal galaxy with the MW Halo and its associated stream (see e.g., Deg & Widrow [2013] and references therein).

In the Galactic Halo, several other streams have been hypothesised since the pioneering suggestion by Lynden-Bell (1976) that the dwarf spheroidal galaxies (dSphs) orbiting around the MW and a number of Galactic globular clusters (GGCs) are distributed along planar alignments. These are usually interpreted as orbital planes resulting from the disruption of galaxies through the interaction with the Galactic Halo. The location of these systems seems to define a vast polar structure in the MW (see e.g., Pawlowski & Kroupa, 2013). Evidence of a similar plane has recently been claimed for M31 by Conn et al. (2013) and Ibata et al. (2013). The Fornax Stream (Majewski, 1994) is an example of these alignments and includes both dSphs (Fornax, Leo I, Leo II, Sculptor and possibly Sextans and Phoenix) and GGCs (Pal 3, Pal 4 and Pal 12). Extra-tidal stellar populations have been detected around several stellar systems, including both GGCs and dSphs. They define either elongated tidal tails or spheroidal shells formed by material tidally stripped in the interaction of these small systems with the MW (see Marconi et al. [2014] for details).

In this scenario, the VLT Survey Telescope (VST) STREGA survey aims at investigating the formation mechanisms for the Galactic Halo, by tracing tidal tails and haloes around stellar clusters and galaxies and mapping the southern portion of the Fornax Stream.

The STREGA survey

The STREGA survey uses part of the VST Guaranteed Time Observation (GTO) allocated by ESO to the Italian Istituto Nazionale di Astrofisica (INAF) in return for the building of the telescope.

The core programme of STREGA (P.I.: M. Marconi/I. Musella; see also Marconi et al., 2014) is the search for stellar overdensities (tidal tails and/or haloes) through detection of variable and main sequence stars around selected dSphs and GGCs up to 2–3 tidal radii. The investigated systems include: Fornax and Sculptor (38 fields), Sextans (13 fields), Phoenix (3 fields), ω Cen and NGC 6752 (37 and 36 fields, respectively), Pal 3 (3 fields) and Pal 12 (2 fields). The location of the selected targets for the STREGA core programme is shown in Figure 1 (by blue and magenta symbols for dSphs and GGCs, respectively). Variable stars, such as RR Lyrae, are easily detectable thanks to their intrinsic luminosity and characteristic light curves, whereas main sequence turn-off (MSTO) stars are about 3.5 mag fainter than RR Lyrae stars but at least 100 times more abundant. The second part of the survey complements the core programme with additional fields

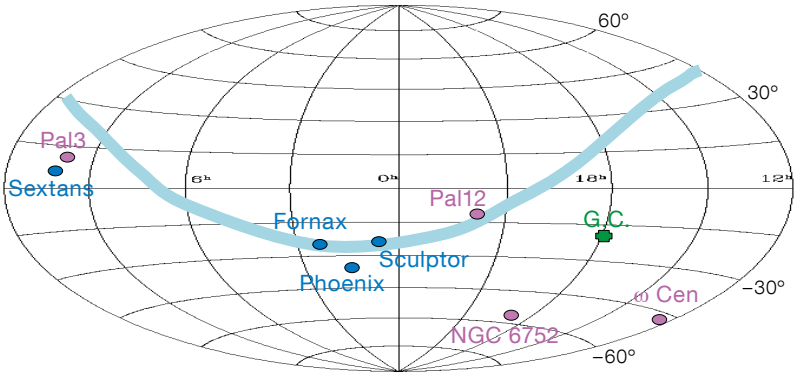

Figure 1. The dSphs (blue symbols) and GGCs (magenta symbols) observed by the STREGA survey. The cyan line represents the orbit of Fornax in equatorial coordinates. The Galactic Centre is marked with a green symbol.

(when needed) and maps the southern portion of the Fornax Stream along strips distributed transverse to the Fornax orbit.

Finally, the STREGA survey has the additional objective of sampling, at various Galactic latitudes, single white dwarfs and interacting binaries in the fields (see Marconi et al. [2014] for further details).

STREGA observing strategy

Owing to its wide field of view and high spatial resolution, OmegaCAM on the VST is the ideal instrument with which to investigate extra-tidal stellar populations or extended haloes around dSphs and GGCs. In our survey, the observations are performed in the SDSS filters *g*, *r* and *i*. We adopt three bands to characterise variable and MSTO stars and provide colour–magnitude and colour–colour diagrams for the investigated stellar populations. In particular, the light curves of the variable stars are accurately sampled by means of time-series observations (about 20 phase points in *g*-band and 10 in *r*- and *i*-bands). The MSTO magnitude is reached by co-addition of single epoch observations or through direct deeper exposures for close systems such as ω Cen, NGC 6752 and Pal 12. Indeed, the exposure times of a few seconds needed to reach the RR Lyrae magnitude level in these clusters are dramatically shorter than telescope overheads. In these cases variability could be investigated with follow-up observations, at other telescopes, on selected fields.

Observations and data reduction

The 2.6-metre VST optical survey telescope (Capaccioli & Schipani, 2011), built by INAF–Osservatorio Astronomico di Capodimonte, Naples, Italy, is equipped with OmegaCAM (Kuijken, 2011), a wide field (1 by 1 degree) camera provided by a consortium of European institutes. It is a 32-CCD, 16k by 16k detector mosaic with a pixel scale of 0.214 arcseconds.

Observations for the VST INAF GTO started at the end of 2011. STREGA proposals have been approved for Periods 88–94. Due to technical and scheduling problems, only a minor part (about 25 %) of the STREGA core programme has been observed so far. In particular, observations have been completed for the fields around ω Cen (observed in ESO Period 88 and in the compensating visitor time in March 2013), NGC 6752 (Periods 89, 93) and Pal 12 (Periods 91, 93).

The data reduction is performed by means of the newly developed VST–Tube imaging pipeline (Grado et al., 2012), specifically conceived for the data from the VST telescope, but adaptable to other single or multi-CCD cameras. The pipeline includes the over-scan, bias and flat-field correction, CCD gain harmonisation and illumination correction. For the individual exposures, relative and absolute astrometric and photometric calibration is applied (see Marconi et al. [2014] for details).

In order to obtain accurate stellar photometry in the crowded stellar clusters, we need to use a package that performs a point spread function (PSF) fitting method (e.g., Stetson, 1987), while for uncrowded fields, we can also adopt aperture photometry. In particular, we use DAOPHOT/ALLSTAR (Stetson, 1987) for the crowded fields, and SExtractor (Bertin & Arnouts, 1996) for the uncrowded ones. The latter package, usually adopted for extragalactic studies, gives accurate results for stellar photometry in uncrowded fields and has the advantage of being fast and fully automated. We have checked the consistency of the two kinds of photometry by comparing the SExtractor measurements with the DAOPHOT/ALLSTAR ones for selected images (Marconi et al., 2014).

Concerning the completed observational runs, the photometry on the four fields including the central part of ω Cen and on the two fields centred on Pal 12, was obtained using the DAOPHOT/ALLSTAR packages. To calibrate the photometry of the four central pointings on ω Cen, observed in non-photometric conditions, we used deep and accurate *UBVRI* photometry by Castellani et al. (2007), transformed to the SDSS *ugriz* photometric system by adopting the transformations by Jordi et al. (2006) computed for Population II stars[1]. Similarly for Pal 12, we checked the photometric calibration using independent and very accurate unpublished *BVI* photometry by Peter Stetson. In the case of NGC 6752, due to the very recent observations of the central region, the calibration procedure is still in progress and so far we have only qualitatively verified the agreement between our colour–magnitude diagrams (CMDs) for the external fields and the central one obtained from unpublished photometry by Stetson (see Marconi et al., 2014 for details). In the following, we show the first results obtained for the fields centred on ω Cen.

The total CMD for the ω Cen sky area

Among the stellar systems that we are currently investigating in the context of the STREGA core programme, a particularly interesting target is ω Cen. This globular cluster is considered to be a tidally disrupted galaxy due to: i) the presence of multi-populations with different chemical compositions (and probably

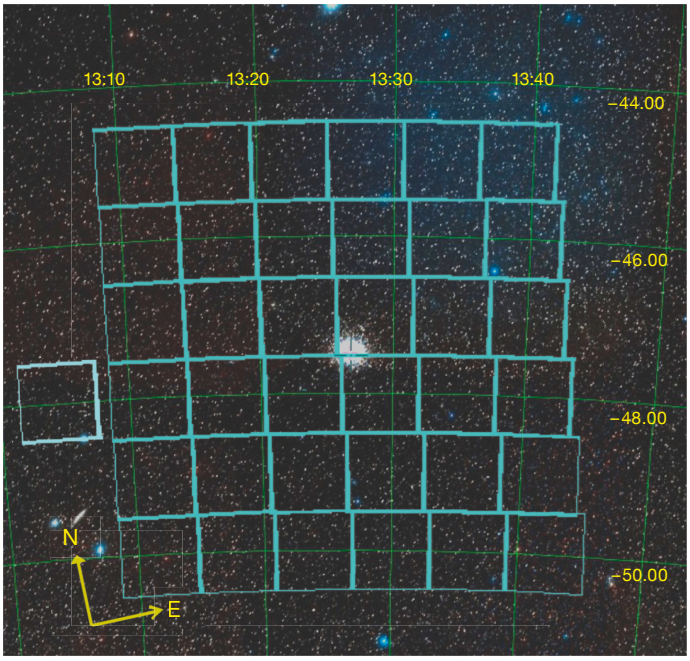

Figure 2. Observed STREGA fields around ω Cen shown in equatorial coordinates.

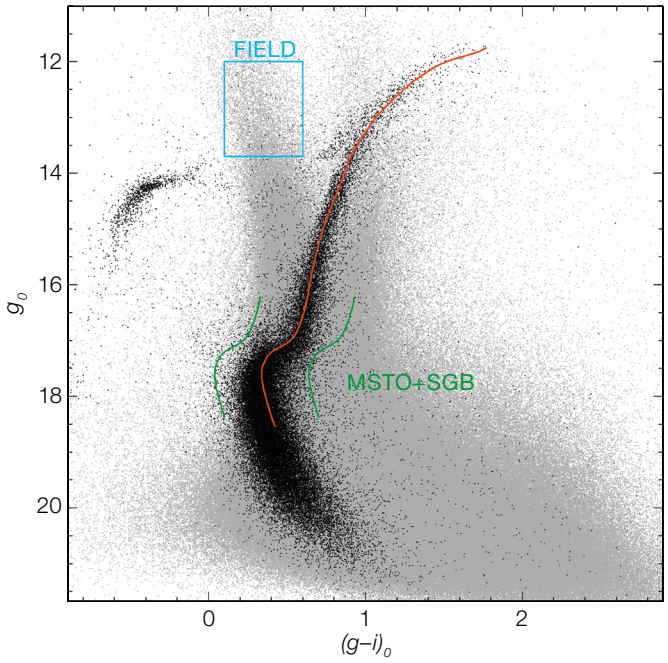

Figure 3. Cumulative CMD (grey dots) compared with the central CMD (black dots) for ω Cen. The red line represents the obtained ridgeline.

different ages); ii) the retrograde orbit combined with an unusually low inclination; iii) the similarity with M54, a globular cluster that is the remnant core of the disrupted Sagittarius galaxy. The presence of tidally stripped stars for ω Cen has been modelled, but only very recently have Majewski et al. (2012) reported empirical evidence for these tidal tails. We have observed, with the VST, the 37 fields shown in Figure 2, centred on ω Cen and reaching about three tidal radii.

Each field is observed in *gri*-bands with a single exposure reaching at least 2 mag below the turn-off. Combining the *g*, *r* and *i* catalogues for all the covered fields, we built the total CMDs *g,g-i* and *g,g-r*. To search for overdensities associated with various evolutionary phases in the CMD, we needed to take into proper account the differential reddening contribution as well as the contamination from the various Galactic components. In order to correct for the reddening in the observed fields, we used the extinction maps of Schlegel et al. (1998), recalibrated by Schlafly & Finkbeiner (2011)[2]. The de-reddened *g,g-i* diagram is shown in Figure 3 (see the following section for details).

In order to model the contribution of the different MW components to the CMD, we used an updated version of the code by Castellani et al. (2002), including three Galactic components, namely the thin and thick Disc and a stellar Halo, with specific spatial structures and star formation laws (see Marconi et al. [2014] for details). Due to the low Galactic latitude, we expect that our CMD is mainly contaminated by thin and thick Disc stars with a smaller fraction of Halo stars. The result of this Galactic simulation for one of the investigated fields is shown in Figure 4 (blue, cyan and grey dots) compared with the synthetic CMD of ω Cen (red symbols) obtained with the SPOT code (Teramo Stellar POpulation Tools; Raimondo et al., 2005). We note that, according to these simulations, it is possible to distinguish the bluest MSTO from the Galactic Disc population.

Extra-tidal stars of ω Cen

We performed star counts on the area observed around ω Cen in order to detect extra-tidal stars. First, we evaluated the photometric completeness to find, in each band, the range of magnitudes where star counts are significant (see Marconi et al. [2014] for details). We considered the central CMD (black dots in Figure 3) obtained on the one square degree field centred on ω Cen to identify the expected location of the various evolutionary phases, namely the horizontal branch, the MSTO and the red giant branch. The red line in Figure 3 represents the empirical ridgeline obtained from the observed central CMD. All the sources lying within ± 0.3 mag (between the green lines), consistent with the dispersion of the MSTO region and with possible residual differential reddening and/or photometric errors and in the magnitude range $16.2 < g_0 < 18.5$ mag, are assumed to belong to the MSTO and sub-giant branch phase (MSTO+SGB). We also identified a region (called FIELD, see blue rectangle in Figure 3) without cluster contamination, corresponding to the ranges $12.0 < g_0 < 13.7$ mag and $0.1 < (g\text{-}i)_0 < 0.6$ mag.

In the left-hand panels of Figure 5 we show the radial profiles of the normalised star densities in the MSTO+SGB region, compared to those in the FIELD region where we expect a negligible contribution of cluster stars. The error bars are the result of the individual count Poisson error.

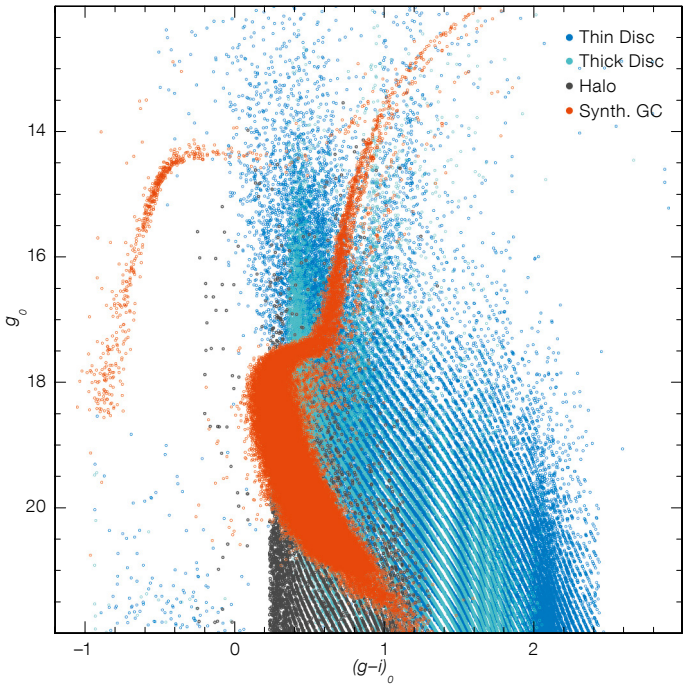

Figure 4. Galactic simulations (blue, cyan and grey dots) compared with the synthetic CMD of ω Cen (red dots).

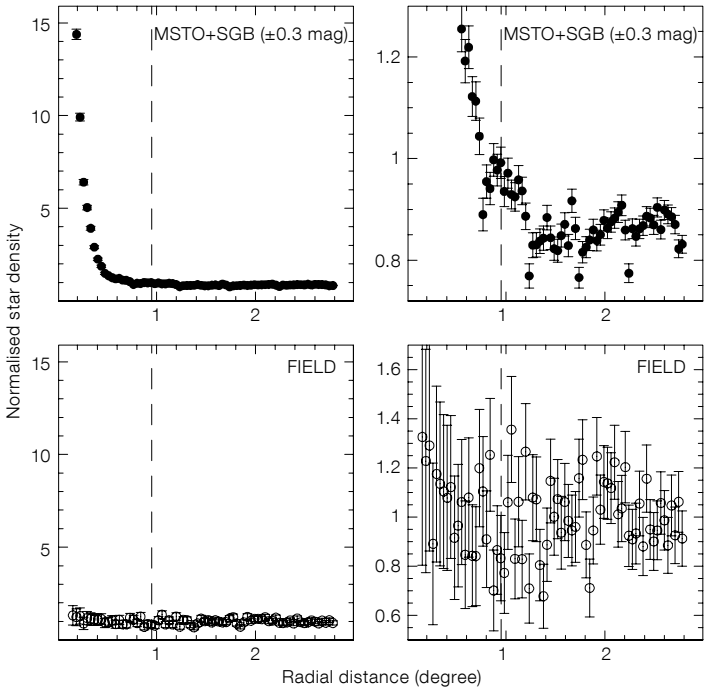

Figure 5. Left-hand panels: Radial profiles of the normalised star densities for ω Cen for objects in the MSTO+SGB and FIELD regions of the CMD (upper and lower respectively). Right hand panels: Zoom-in of the left panels around the nominal tidal radius.

We covered the region from the centre to 2.8 degrees (about three nominal tidal radii) with 75 equally spaced annuli. The star density in the i^{th} annulus is normalised to the corresponding total count in the circle with the radius of 2.8 degrees. The nominal tidal radius (0.95 degrees, corresponding to the vertical dashed line in Figure 5; see Harris, 1996; Da Costa & Coleman, 2008) is intermediate between the two values provided by McLaughlin & van der Marel (2005), adopting a King model (0.80 degrees; King, 1966) and a Wilson model (1.2 degrees; Wilson 1975),

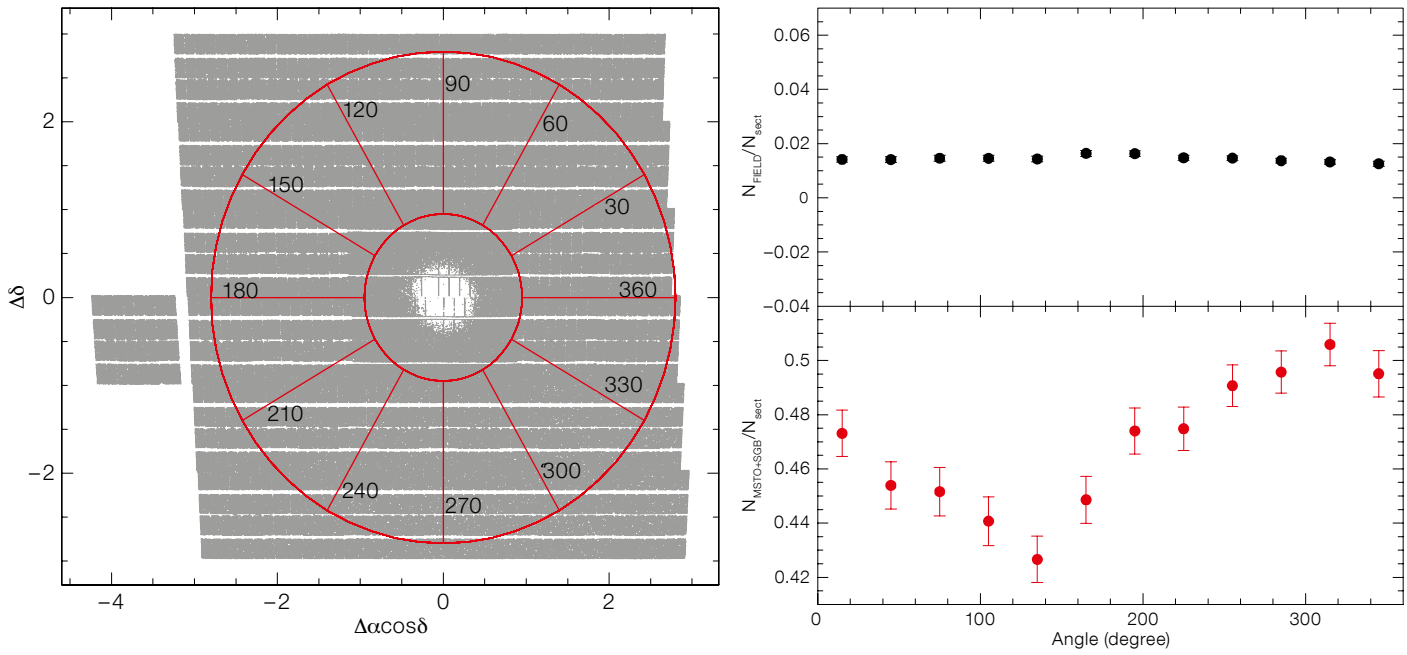

Figure 6. Left panel: Circular sectors used for the angular star counts around ω Cen. Right panel: Normalised star counts for MSTO+SGB (red dots) and FIELD stars (black dots) in the angular sectors shown in the left panel.

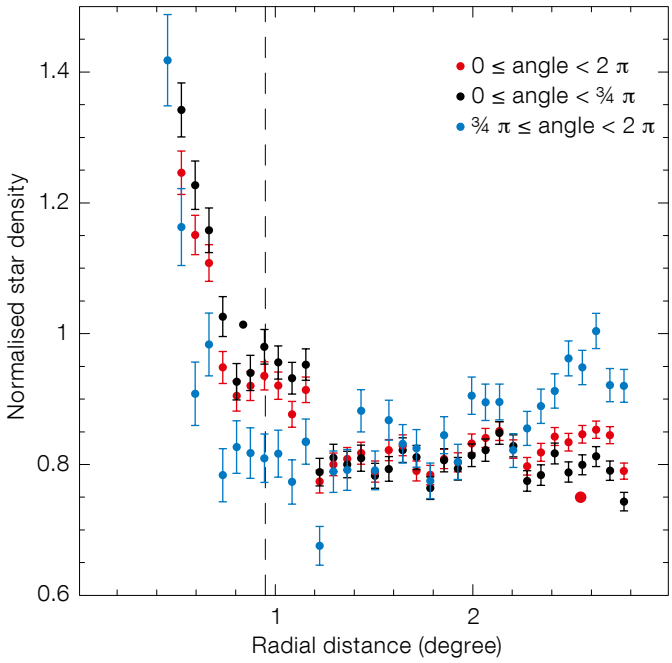

Figure 7. Radial profile of the normalised star densities for the ω Cen MSTO+SGB stars in the different labelled angular regions.

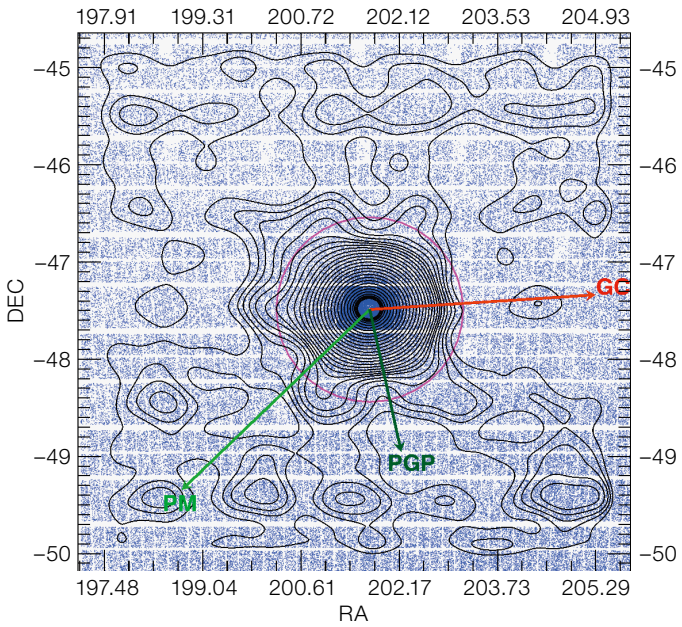

Figure 8. Contour level of the stars around ω Cen projected on the sky. Orientation is the same as in Figure 2. The long light green arrow shows the direction of proper motion (PM); see text for details.

respectively. We recall that the evaluation of the tidal radius is not only model-dependent (McLaughlin & van der Marel, 2005) but also difficult to obtain on account of the possible contribution of tidal tails or other kinds of extra-tidal stellar population (see e.g., Di Cecco et al. [2013] and references therein).

The right-hand panels of Figure 5 show a zoom of these plots to highlight the behaviour around the tidal radius. While, as expected, the FIELD stars do not show any specific trend, the MSTO+SGB stars follow the typical globular cluster profile (see e.g., King, 1966; Wilson, 1975). Inspection of this plot suggests that the nominal tidal radius is slightly underestimated. According to the observed MSTO+SGB star counts, the value based on the Wilson model (1.2 degrees; McLaughlin & van der Marel, 2005) seems to be more in agreement with the data, with an additional non-negligible density increase around and beyond two nominal tidal radii. The latter evidence could be the signature of the presence of tidal tails.

To verify this hypothesis we decided to consider the MSTO+SGB star counts also as a function of the direction, by dividing the total explored area into twelve 30-degree circular sectors (see left-hand panel of Figure 6), with a radial distance ranging from one to three tidal radii. The MSTO+SGB star counts in the sectors are normalised to the total number of stars in the same area, in order to reduce spurious effects due to the variation of the disc contribution with Galactic latitude.

The MSTO+SGB star counts as a function of angle are shown in the lower right-hand panel of Figure 6, where a clear peak is observed around 300 degrees (the south-east direction). This corresponds to the predicted orientation of the cluster ellipticity (see e.g., Table 5 in Anderson & van der Marel, 2010). It is also significant that FIELD star counts (upper right-hand panel) do not follow the same trend.

In Figure 7, the MSTO+SGB star count radial profile in the direction corresponding to the overdensity (blue filled circles) is compared with the total one (red filled circles) and with the one in the complement to 2π (black filled circles). This comparison shows how the radial profile varies with the angle: the star overdensity detected beyond the tidal radius is more evident to the southeast. Moreover, even excluding this overdensity direction and looking at the radial profile in the opposite direction (black filled circles), we find an excess of stars at about 1 degree from the centre, corresponding to an effective tidal radius of about 1.2 degrees.

Similar behaviour can also be noted in the contour level map, again for the MSTO+SGB candidate cluster stars, shown in Figure 8 (see Marconi et al. [2014] for details). The excess of stars beyond the nominal tidal radius (0.95 degrees, magenta circles) is evident in the second, third and fourth quadrants (usual clockwise definition) where it extends up to about 2 degrees, confirming the evidence of extra- tidal stars inferred from Figure 5.

Inspection of Figure 8 also suggests that the asymmetry of the contour levels increases when moving from the innermost to the outermost cluster regions. This result agrees with the evaluation of ω Cen eccentricity in the literature (e.g., Bianchini et al., 2013). Finally we note that the detected overdensity orientation in Figure 8 appears to be orthogonal

to ω Cen's proper motion direction (PM, green arrow) and intermediate between the direction of the Galactic Centre (GC, red arrow) and the projection on the sky of the direction perpendicular to the Galactic Plane (PGP, dark green arrow). The position angle of the major axis indicated by these star counts, measured east from north, is about 140 degrees and agrees quite well with the one based on Hubble Space Telescope Advanced Camera for Surveys photometry of the innermost cluster regions (Anderson & van der Marel, 2010). Even though to understand the nature of the detected extra-tidal stars, the information on their proper motion and radial velocity is needed, the presence of an asymmetric, elongated extra-tidal structure is evident and consistent with current measurements and predictions in the literature for the cluster ellipticity profile and orientation.

The preliminary results shown here clearly demonstrate the wealth of information that can be extracted from the VST observations. On this basis, when the STREGA survey is complete we will be able to significantly improve our knowledge of Galactic structure and evolution, providing useful constraints complementary to the geometric information that will be inferred with the Gaia satellite.

References

Anderson, J. & van der Marel, R. P. 2010, ApJ, 710, 1032
Bertin, E. & Arnouts, S. 1996, A&AS, 117, 393
Bianchini, P. et al. 2013, ApJ, 772, 67
Capaccioli, M. & Schipani, P. 2011, The Messenger, 146, 2
Castellani, V. et al. 2002, MNRAS, 334, 69
Castellani, V. et al. 2007, ApJ, 663, 1021
Conn, A. R. et al. 2013, ApJ, 766, 120
Da Costa, G. S. & Coleman, M. G. 2008, AJ, 136, 506
Deg, N. & Widrow, L. 2013, MNRAS, 428, 912
Di Cecco, A. et al. 2013, AJ, 145, 103
Grado, A. et al. 2012, Mem. Soc. Astron. Ital. Suppl., 19, 362
Harris, W. E. 1996, AJ, 112, 148
Ibata, R. A. et al. 2013, Nature, 493, 62
King, I. R. 1966, AJ, 71, 64
Kuijken, K. 2011, The Messenger, 146, 8
Lynden-Bell, D. 1976, MNRAS, 174, 695
Majewski, S. R. et al. 2012, ApJ, 747, L37
Marconi, M. et al. 2014, MNRAS, in press, arXiv:1406.4375
McLaughlin, D. E. & van der Marel, R. P. 2005, ApJS, 161, 304
Pawlowski, M. S. & Kroupa, P. 2013, MNRAS, 435, 2116
Raimondo, G. et al. 2005, AJ, 130, 2625
Schlegel, D. J., Finkbeiner, D. P. & Davis, M. 1998, ApJ, 500, 525
Stetson, P. 1987, PASP, 99, 191
Wilson, C. P. 1975, AJ, 80, 175

Links

[1] *UBVRI* to SDSS *griz* transformations: http://classic.sdss.org/dr7/algorithms/sdssUBVRITransform.html#Jordi2006
[2] Recalibrated Schlegel extinction: http://irsa.ipac.caltech.edu/applications/DUST/

ESO/INAF-VST/OmegaCAM. Acknowledgement: A. Grado/INAF-Capodimonte Observatory

Large-field (51 arcminute square) image of the globular cluster ω Cen taken with the VLT Survey Telescope by combining *g*-, *r*- and *i*-band images.

The Abundance of Lithium Measured for the First Time Beyond Our Galaxy

Alessio Mucciarelli[1]
Maurizio Salaris[2]
Piercarlo Bonifacio[3]
Lorenzo Monaco[4]
Sandro Villanova[5]

[1] Dipartimento di Fisica & Astronomia, Universitá degli Studi di Bologna, Italy
[2] Astrophysics Research Institute, Liverpool John Moores University, Liverpool, United Kingdom
[3] GEPI, Observatoire de Paris, CNRS, Univ. Paris Diderot, Meudon, France
[4] ESO
[5] Universidad de Concepcion, Casilla, Concepcion, Chile

The discrepancy between the primordial lithium abundance derived from Population II dwarf stars and from the predictions of standard Big Bang nucleosynthesis is one of the most intriguing and challenging open questions in modern astrophysics. The use of lower red giant branch stars, instead of the usual method of observing dwarf stars, represents a new approach to attacking the problem. Lithium in distant, extragalactic stellar systems, for which observations of dwarf stars are precluded because of their faintness, becomes open for investigation. From observations with FLAMES at the VLT, we have been able to derive for the first time the initial lithium abundance in an extragalactic globular cluster, namely M54 in the Sagittarius galaxy.

Lithium, together with hydrogen and helium, is synthesised during the early phase of the Universe, in the first few minutes after the Big Bang. All the elements heavier than lithium are produced later, mainly during the nucleosynthesis occurring in the stellar interiors. In particular, the primordial lithium abundance is strictly linked to the baryonic density (Ω_B), a cosmological parameter that quantifies the amount of ordinary matter. Hence, the study of the lithium abundance in the oldest stars is crucial for several different astrophysical topics, i.e., cosmology, stellar evolution and globular cluster formation.

In a seminal paper, Spite & Spite (1982) first noted that dwarf Population II stars in the Solar Neighbourhood (with [Fe/H] < –1.5 and effective temperatures > 5800 K) share the same lithium abundance, regardless of their metallicity and temperature, a feature known as the Spite Plateau. The derived lithium abundance turns out to be in the range A(Li) = 2.1–2.4 dex, depending on the adopted temperature scale. The existence of a narrow lithium plateau has been confirmed by three decades of observations, both in halo field stars and in globular cluster stars.

The results obtained with the Wilkinson Microwave Anisotropy Probe (WMAP; Spergel et al., 2007) and Planck (Planck collaboration, 2013) satellites have provided an alternative route to inferring Ω_B. In fact, these high precision measurements of the cosmic microwave background (CMB) have allowed Ω_B to be estimated with unprecedented accuracy. The derived value of Ω_B, coupled with the standard Big Bang nucleosynthesis (SBBN) model, provided a lithium abundance of 2.72 ± 0.06 dex (Coc et al., 2013). This value is significantly higher, by at least a factor of three, than the lithium abundance derived from dwarf stars. Such a discrepancy is referred to as the cosmological lithium problem.

At present, the discrepancy between the Spite Plateau and the CMB + SBBN results is still unexplained. Three possible explanations appear to be especially promising:

1) the effect of atomic diffusion and some competing additional mixing, the combined effect of which decreases the lithium abundances in the atmospheres of dwarf stars (see e.g., Korn et al., 2006);
2) inadequacies in the SBBN models used to calculate the lithium abundance (Iocco et al., 2009);
3) lithium depletion driven by Population II stars during early Galaxy evolution (Piau et al., 2006).

Whatever the solution of the lithium problem is, the investigation of this discrepancy (and its solution) is a formidable chance to understand SBBN in greater depth and refine our description of the processes occurring in the first few minutes after the Big Bang. In fact, if the primordial lithium abundance derived from the CMB results is incorrect, the current SBBN model would have to be drastically re-thought, introducing "new physics", e.g., the inclusion of "new" high-energy, non-thermal particles and the annihilation/decay of dark matter particles. On the other hand, if the initial lithium content in Population II stars is depleted by transport processes, the measurement of the lithium abundance in these stars could provide robust constraints on the efficiency of turbulent mechanisms occurring at the bottom of the stellar convective envelope (which is a free parameter in the stellar models).

An alternative route: The lower RGB stars

Mucciarelli, Salaris & Bonifacio (2012) proposed an alternative/complementary route to investigate the initial lithium abundance in Population II stars (with respect to the observations of dwarf stars), by measuring the surface lithium abundance in lower red giant branch (RGB) stars. These stars are defined as the giants evolving between the first dredge-up and the luminosity level of the RGB Bump. When a star evolves off the main sequence, the convection propagates inward (first dredge-up) reaching hot regions where lithium has been burned. Lithium-free material is dredged up to the surface, with the main effect of reducing the surface lithium abundance. When the convective envelope attains its maximum penetration, depletion of the surface lithium abundance ends. Afterwards the lithium abundance remains constant until the star reaches the luminosity level of the RGB Bump; then, an additional mixing episode occurs, further reducing the surface lithium abundance down to virtually zero, or to effectively non-measurable values (see Figure 1).

The lower RGB stars (both in the Galactic field and globular clusters) display a constant lithium abundance, defining a plateau that mirrors the Spite Plateau, but at a lower abundance (A(Li) ~ 0.9–1.0 dex). Since the amount of lithium depletion after the first dredge-up can be predicted easily from stellar models, the lithium abundance measured among the lower RGB stars can be used to infer or

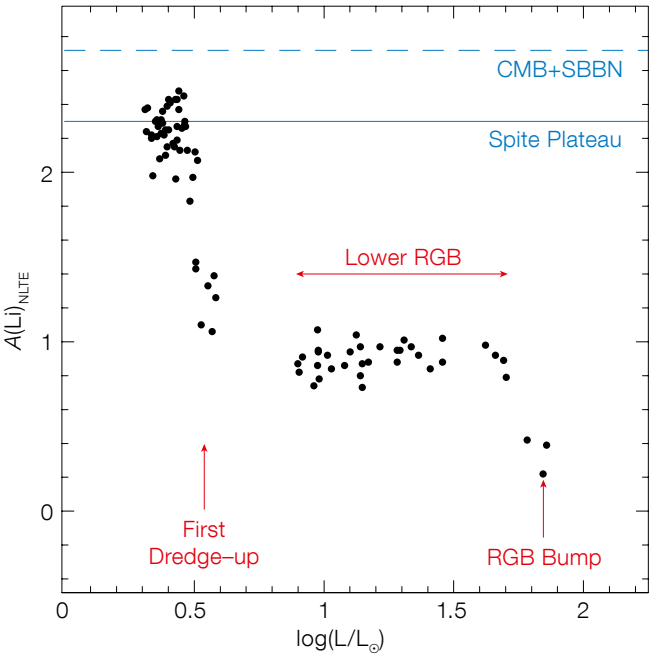

Figure 1. Behaviour of the surface lithium abundance as a function of luminosity for the stars in the globular cluster M4 (from Mucciarelli et al., 2011). The value of the initial lithium abundance as derived by the CMB + SBBN is marked as a blue dashed line. The value of the lithium abundance as derived from dwarf stars (the Spite Plateau) is marked by the blue solid line.

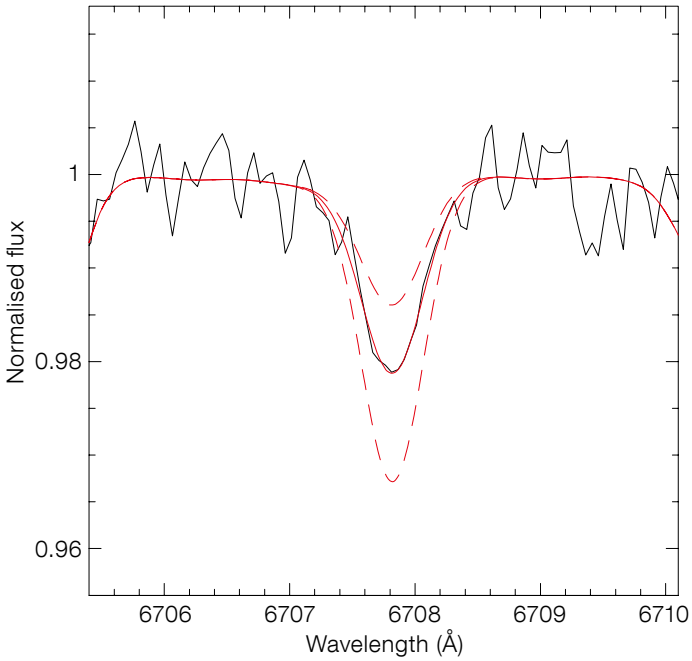

Figure 2. The observed lithium doublet of the average spectrum obtained by combining 51 member stars of M54 observed with FLAMES GIRAFFE. Superimposed are the best-fit synthetic spectrum and two synthetic spectra calculated with lithium abundance variations of ± 0.2 dex.

constrain the initial lithium abundance of those stars.

This new diagnostic has extraordinary potential and advantages. In particular:

1) The derived abundance of lithium is totally independent of the abundances obtained from dwarf stars and therefore does not suffer from the large uncertainties on the turbulent mixing affecting that evolutionary stage. Note that the uncertainties related to the efficiency of diffusion processes amount to 0.4 dex or more for the lithium abundance in dwarf stars, while they are smaller than 0.07 dex for lower RGB stars;
2) The use of lower RGB stars will allow estimates of the lithium content in stellar populations more distant than those usually observed to investigate the Spite Plateau. The obvious benefits are not only to enlarge the sample of Galactic field and cluster stars to study the primordial lithium abundance, but also to offer the formidable opportunities to investigate the initial lithium abundance in extragalactic systems where the observation of dwarf stars is precluded because of their distance.

Lithium abundance in M54

We have recently approached the lithium problem by adopting this new diagnostic. We used the lower RGB stars to investigate for the first time the lithium abundance outside the Milky Way (Mucciarelli et al., 2014). We obtained high-resolution spectra of 51 member stars of the globular cluster M54, with the FLAMES facility mounted at the Kueyen Unit Telescope of the Very Large Telescope (VLT) and the GIRAFFE spectrometer. M54 is a massive globular cluster located at ~ 25 kpc from the Sun and immersed in the nucleus of the Sagittarius dwarf galaxy. The dwarf stars in M54 and the Sagittarius galaxy are too faint (at V ~ 22 mag) to measure their lithium abundance, even with the VLT, hence the study of lower RGB stars currently represents the only possible route to infer the lithium abundance in this galaxy.

Figure 2 shows the lithium doublet at 6707 Å observed in an average spectrum, obtained by combining together the spectra of the 51 stars, in order to enhance the spectral quality. Superimposed are the best-fit synthetic spectrum and two synthetic spectra calculated with lithium abundance variations of ± 0.2 dex.

We measured A(Li) = 0.93 ± 0.11 dex, in agreement with measurements in lower RGB stars of the Galactic Halo. By considering the dilution due to the first dredge-up, we established that the initial lithium abundance of this stellar system (in the range A(Li) = 2.29–2.35 dex) was compatible with those derived in dwarf stars. This is the most distant measurement of the initial lithium abundance in old, metal-poor stars obtained so far. In fact, all the previous studies of the lithium abundance in dwarf stars are restricted to distances within ~ 8 kpc from the Sun.

Figure 3 summarises the state of the art of our current knowledge of the lithium abundance. The initial lithium abundance obtained in M54 matches

the Spite Plateau well but is lower than the CMB + SBBN value by ~ 0.3 dex. This demonstrates that old stars, regardless of their birthplace, were born with the same initial lithium abundance.

Also, an important question can be addressed by our study: is the lithium problem a local problem, limited to our Galaxy, or is it independent of the environment? The analysis of M54 confirms the findings in ω Centauri (Monaco et al., 2010) considered as the remnant of an accreted dwarf galaxy: the lithium problem seems to be a universal problem, regardless of the parent galaxy.

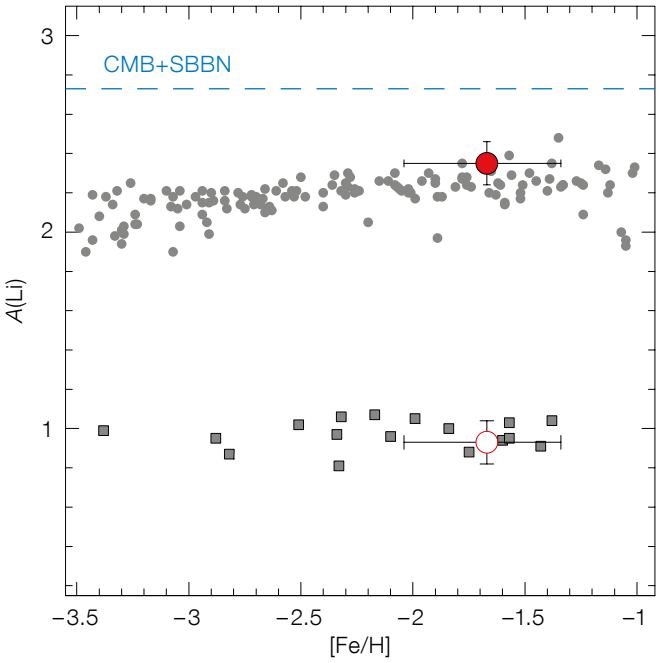

Figure 3. Abundance of lithium as a function of [Fe/H] for the Spite Plateau (grey circles) and lower RGB stars (grey squares) of the Galactic field. The empty red circle denotes the surface lithium abundance measured in the lower RGB stars of M54, while the filled red circle shows the initial lithium abundance of M54. The blue dashed line is the initial lithium abundance from CMB + SBBN.

A new tool for new instruments

The result obtained for M54 demonstrates the potential of lower RGB stars in the investigation of the initial lithium abundance in stellar systems for which the observation of dwarf stars is precluded. This study has allowed a giant leap in this kind of study, pushing our view to ~ 25 kpc from the Sun. Besides the natural impact on the theoretical SBBN model and stellar evolutionary models, the accurate investigation of the lithium abundance in lower RGB stars also has an important benefit in terms of the definition of science cases for the next generation of spectroscopic instrumentation. In fact, the proper calibration of this diagnostic using a wide sample of Galactic stars is a fundamental step in the process of observing very distant lower RGB stars with the next generation of 30–40-metre-class telescopes (such as the European Extremely Large Telescope or the Giant Magellan Telescope).

The current generation of high-resolution spectrographs mounted on 8–10-metre-class telescopes (like the VLT, Keck and Subaru) allows us to reach lower RGB stars in stellar systems out to ~ 25 kpc from the Sun, with a typical magnitude of V ~ 18.5. The advent of the 30–40-metre-class telescopes will allow observation of lower RGB stars out to the closest dwarf spheroidal galaxies (~ 80 kpc), while dwarf stars will be observed out to the Magellanic Clouds (~ 50–60 kpc). Thus, this new diagnostic represents a powerful science case for the future giant telescopes.

References

Coc, A., Uzan, J.-P. & Vangioni, E. 2013, arXiv1307.6955
Korn, A. J. et al. 2006, Nature, 442, 657
Iocco, F. et al. 2009, Phys. Rev., 472, 1
Monaco, L. et al. 2010, A&A, 519L, 3
Mucciarelli, A. et al. 2011, MNRAS, 412, 81
Mucciarelli, A., Salaris, M. & Bonifacio, P. 2012, MNRAS, 419, 2195
Mucciarelli, A. et al. 2014, MNRAS, 444, 1812
Piau, L. et al. 2006, ApJ, 653, 300
Planck Collaboration, 2013, arXiv1203.5076
Spergel, D. N. et al. 2007, ApJS, 170, 377
Spite, M. & Spite, F. 1982, Nature, 297, 483

VLT Survey Telescope *u*-, *g*- and *r*-band colour image of the globular cluster M54 situated at the core of the Sagittarius Dwarf Galaxy. See eso1428 for details.

CLASH-VLT: A VIMOS Large Programme to Map the Dark Matter Mass Distribution in Galaxy Clusters and Probe Distant Lensed Galaxies

Piero Rosati[1]
Italo Balestra[2]
Claudio Grillo[3]
Amata Mercurio[4]
Mario Nonino[2]
Andrea Biviano[2]
Marisa Girardi[5]
Eros Vanzella[6]
and the CLASH-VLT Team*

[1] Università degli Studi di Ferrara, Italy
[2] INAF–Osservatorio Astronomico di Trieste, Italy
[3] Dark Cosmology Centre, Copenhagen, Denmark
[4] INAF-Osservatorio Astronomico di Capodimonte, Napoli, Italy
[5] Università degli Studi di Trieste, Italy
[6] INAF-Osservatorio Astronomico di Bologna, Italy

The CLASH-VLT VIMOS Large Programme builds on the CLASH Hubble Space Telescope multi-cycle treasury programme to carry out a comprehensive spectroscopic campaign on 13 massive galaxy clusters in the southern sky, at a median redshift of 0.4. Observations are 95 % complete and provide spectroscopic identification for 500 to 1000 members per cluster, and over 200 background lensed galaxies at $z < 7$. When combined with a homogeneous set of multi-wavelength ancillary observations, this project will allow a determination of cluster mass density profiles with dynamical and lensing methods and a characterisation of the inner structure of cluster dark matter halos with unprecedented accuracy. The final spectroscopic CLASH-VLT dataset will contain ~ 30 000 spectra and redshifts, of which ~ 7000 are cluster members, providing a long-lasting legacy for studies of galaxy evolution in different environments.

*The CLASH-VLT Team:
Piero Rosati[1](P.I.), Marianna Annunziatella[2], Italo Balestra[3], Matthias Bartelmann[4], Gabriel Bartosch Caminha[1], Narciso Benitez[5], Andrea Biviano[3], Stefano Borgani[2], Tom Broadhurst[6], Dan Coe[7], Oliver Czoske[8], Gabriella De Lucia[3], Camilo Delgado Correal[1], Ricardo Demarco[9], Stefano Ettori[10], Holland C. Ford[11], Alexander Fritz[12], Brenda Frye[13], Marisa Girardi[2], Raphael Gobat[14], Genevieve Graves[15], Claudio Grillo[16], Anton M. Koekemoer[7], Ulrike Kuchner[8], Doron Lemze[11], Marco Lombardi[17], Elinor Medezinski[11], Simona Mei[18], Christian Maier[8], Massimo Meneghetti[10], Amata Mercurio[19], Anna Monna[20], Mario Nonino[3], Marc Postman[7], Eniko Regoes[21], Alessandro Rettura[22], Barbara Sartoris[2], Joana Santos[23], Marco Scodeggio[12], Stella Seitz[20], Veronica Strazzullo[24], Paolo Tozzi[23], Keiichi Umetsu[25], Eros Vanzella[10], Miguel Verdugo[8], Wei Zheng[11], Bodo Ziegler[8], Adi Zitrin[26]

[1]Università degli Studi di Ferrara; [2]Università degli Studi di Trieste; [3]INAF–Osservatorio Astronomico di Trieste; [4]Institut für Theoretische Astrophysik, Heidelberg; [5]IAA, Granada; [6]University of the Basque Country; [7]STScI; [8]University of Vienna; [9]Universidad de Concepcion; [10]INAF–Osservatorio Astronomico di Bologna; [11]Johns Hopkins University; [12]INAF–IASF Milan; [13]University of Arizona; [14]Korea Institute for Advanced Study; [15]University of California, Berkeley; [16]Dark Cosmology Centre; [17]Università degli Studi di Milano; [18]University of Paris; [19]INAF–Osservatorio Astronomico di Capodimonte; [20]University Observatory Munich; [21]CERN; [22]JPL-Caltech; [23]INAF–Osservatorio Astronomico di Arcetri; [24]CEA Saclay; [25]Institute of Astronomy and Astrophysics, Taiwan; [26]California Institute of Technology.

Galaxy clusters have long served as a bridge between astrophysics and cosmology. Their distribution at varying masses, across space and time, is an important tool with which to constrain cosmological models, since their abundance as a function of redshift is very sensitive to both the underlying geometry of the Universe and the growth of structure on large scales. The mass budget of massive clusters consists of 85–90 % dark matter and 10–15 % baryons, primarily hot X-ray-emitting plasma, and only ~ 1 % in stars. Basically the whole baryon budget is observable in galaxy clusters, unlike in the field. Multi-wavelength studies of meaningful samples of clusters thus lead to a better understanding of the physical mechanisms driving galaxy evolution over a range of environmental densities, and how galaxy formation and black-hole accretion processes modulate the cycle of hot and cold baryons.

The first evidence of dark matter (DM) was found in the 1930s by Fritz Zwicky in the Coma cluster, when he noted a large discrepancy between its virial and luminous mass. Remarkably, he also anticipated the effective use of gravitational lensing to measure the total mass of massive clusters and study distant galaxies. In modern cosmology, clusters pinpoint the largest (gravitationally bound) dark matter halos. As a result, the study of their inner mass distribution offers an important method to test the currently favoured Lambda Cold Dark Matter (ΛCDM) structure formation scenario.

Cold dark matter drives the dynamical evolution of structure shown in cosmological simulations and leads to specific predictions for the mass density profiles of DM halos, from galaxy to cluster scale. Significant deviations from these theoretical expectations would imply that the dynamical history of hierarchical formation of clusters does not proceed according to the ΛCDM paradigm: examples are a non-standard contribution to the mass–energy density of the Universe at the epoch of cluster formation, or a different nature for dark matter. The latter could be revealed particularly in the inner, high-density cluster cores, where a non-collisionless behaviour of DM particles might well modify the inner slope of the mass distribution.

These tests however require very accurate determination of the mass density profile of a representative sample of clusters over a wide radial range, from kpc to Mpc scales. This can be achieved only if all methodologies available to measure the mass distribution of clusters are employed, namely gravitational lensing, galaxy dynamics and X-ray hydrostatic equilibrium. (Sunyaev–Zeldovich-based mass profiles are also becoming important in these studies, but will not be dealt with here.) The reason is that each method is most sensitive to a different radial range and is prone to different inherent systematic effects: e.g., structure along the line of sight for lensing, substructure and velocity anisotropy of orbits for dynamical masses, deviations from hydrostatic equilibrium for X-ray masses. Only by combining and cross-checking mass determinations from all these methods can cluster density profiles be recovered with the required accuracy, provided that a high quality and homogeneous dataset is available for a representative sample of clusters, with a known selection function.

Until a few years ago, the observational framework was far from this ideal status. Measured mass profiles with gravitational lensing techniques of a handful of clusters seemed to suggest mass concentrations significantly higher than theoretical expectations; other studies found that the mass distribution in the cores ($R < 100$ kpc)

was significantly flatter than in simulated clusters. It was not uncommon to find a lack of consistency in the literature for the measured mass profiles of the same clusters or between different methods (e.g., X-ray *vs*. lensing). Many suspected that poor sample selection, heterogeneous datasets and the presence of several systematics prevented robust analyses and an effective test of ΛCDM models.

Among the mass probes, strong gravitational lensing, which has produced so many spectacular images of cluster cores with the Hubble Space Telescope (HST), has the unique ability to resolve the inner structure of dark matter halos down to galaxy scale, provided that a sufficient number of multiple images with distance information is available. In addition, close to the critical lines, lensing can magnify background galaxies by a factor of ten or more. Massive clusters can thus be used as gravitational telescopes, albeit on small (~ 1 square arcminute) fields, for serendipitous discoveries of very faint distant galaxies, which would otherwise escape detection. The advantage of this technique was already demonstrated more than a decade ago by the detection of a handful of lensed galaxies out to $z \sim 7$ and by high signal-to-noise (S/N) spectra of a few highly-magnified Lyman-break galaxies at $z \sim 2$–3.

The CLASH project

In order to enable landmark progress in the measurement of the mass distribution of massive clusters, and carry out a systematic search for distant magnified galaxies, the Cluster Lensing And Supernova survey with Hubble (CLASH) project was approved in 2011. It is one of the three Multi-Cycle Treasury Programmes with Hubble (Principal Investigator: M. Postman; see Postman et al., 2012). A total of 524 orbits were allocated to obtain panchromatic 16-filter (with the Advanced Camera for Surveys [ACS] and Wide Field Camera 3 [WFC3], from the near-ultraviolet to the near-infrared) imaging for 25 massive clusters. Observations were spread over several epochs to enable the search for Type-Ia supernovae at $z > 1$ to improve constraints on cosmological parameters; in this article we will not cover this aspect of the CLASH programme.

The CLASH[1] sample was carefully chosen to be representative of 20 relaxed clusters, on the basis of their symmetric and smooth X-ray emission, spanning a wide redshift range (0.18–0.90, median = 0.4). The limiting X-ray temperature is 5 keV, approximately corresponding to a mass limit of $M > 5 \times 10^{14}\ M_{\odot}$. Five additional clusters were included as known powerful lenses to maximise the chance of finding magnified galaxies at $z > 7$. Observations were completed in 2013 and their analysis has produced a very rich variety of new results. They range from a definite determination of the degree of concentration of the mass profiles as a function of cluster mass (Merten et al., 2014), to a census of star-forming galaxies at $z \sim 9$–10, some 500 million years after the Big Bang (Coe et al., 2013; Bouwens et al., 2014).

The CLASH-VLT project

Building on the CLASH HST panchromatic imaging project, and a wealth of multi-wavelength data covering a much larger area for each cluster, a VIMOS Large Programme (LP), hereafter CLASH-VLT[2], was approved in Period 86 (P86) to carry out an unprecedented spectroscopic campaign on the 14 CLASH clusters accessible from the Very Large Telescope (VLT). The project was conceived to literally provide the third dimension to the CLASH survey, with the spectroscopic identification of large samples of cluster members and background lensed galaxies, such as giant arcs and multiple images.

Specifically, the CLASH-VLT LP had 225 hours allocated (200 hours of multi-object spectroscopy [MOS] and 25 hours of pre-imaging), initially distributed over P86–P89, with the following objectives:

1) Obtain spectroscopic confirmation of ~ 500 cluster members in each cluster out to at least twice their virial radius. This goal was set, with the aid of kinematic data from cosmological simulations, to recover the dynamical mass profile with the same accuracy as the strong + weak lensing profiles.
2) Measure redshifts for over 200 lensed galaxies in the cluster cores, including several highly magnified galaxies out to $z \approx 7$ (when Ly-α moves out of the VIMOS optical window). This provides confirmation of multiply imaged systems detected in the HST images and the angular diameter distances of lensed sources, which are crucial inputs for accurate strong lensing models. Additional targets include optical counterparts of Chandra X-ray sources in the cluster fields and host galaxies identified in the supernova programme, if they are bright enough.
3) Provide an unprecedented legacy dataset to investigate galaxy populations in a range of environments with the full set of multi-wavelength data.

At the time of writing the data acquisition is nearly complete with only 5% (10 hours) remaining to be executed.

The VIMOS low-resolution LR-blue grism was primarily used. When lensed sources with high photometric redshifts were present, the medium-resolution (MR) grism was selected instead. VIMOS multiplexing capabilities and field of view, covering approximately 10 Mpc at the median redshift (~ 0.4) of the sample, are very well suited for this project. Additional key observations for this programme are archival imaging data obtained with the Subaru Suprime-Cam for most clusters, with ESO Wide Field Imager (WFI) images for the southernmost target RXJ2248. Subaru multi-colour imaging is ideal for weak lensing studies, owing to its image quality, field of view and depth. In fact, this has formed the basis for the CLASH weak lensing mass density profiles (e.g., Umetsu et al., 2012). Subaru data are however also excellent for spectroscopic target selection, providing photometric catalogues for slit-mask design, after their coordinates are registered to the VIMOS pre-imaging astrometric system.

Eight to twelve VIMOS pointings are used for each cluster, spanning an area of 15–20 square arcminutes, while keeping one quadrant locked onto the cluster core to increase the total exposure time on faint lensed sources. Data are reduced with the VIMOS Interactive Pipeline and Graphical Interface (VIPGI) software developed in Milan, with important contributions from Marco Scodeggio and Alexander Fritz. This pipeline is also used for other VIMOS LPs (e.g., COSMOS and VIPERS). Significant time had to be invested to recover the correct sky positions associated with each spectrum

in an automated fashion, because the chances of misidentification with the standard VIPGI algorithm are not negligible in crowded cluster fields. To date, 75 % of the data are fully reduced with measured redshifts and positions.

First results

A summary of the success rate in identifying cluster members is shown in Figure 1. This shows that the goal of 500 members was achieved in most cases and often exceeded. For three clusters, the number of confirmed cluster members is around 1000 or more, which is unprecedented at these redshifts. Note that observations for MACSJ2129-0741 were interrupted early on due to significant Galactic cirrus contamination and that MACSJ0429-0253 was dropped from the original sample to compensate for the relatively slow observational progress in the highly oversubscribed 1 to 5 hours right ascension range.

Thousands of these spectroscopic redshifts, mostly confined to the z = 0.1–1.2 range, but also extending to z ~ 5, have been used to calibrate and check the accuracy of the CLASH HST-based photometric redshifts (Jouvel et al., 2014), which are an important first ingredient for strong lensing models. Using the 16-band HST photometry, an accuracy of $\Delta z/(1+z)$ = 0.03 can be achieved.

An example of the results from the spectroscopic campaign of MACSJ0416-2403 is shown in Figure 2. The completion of observations of this target, which is also part of the recently launched Frontier Fields campaign with HST, will yield almost a thousand cluster members. Significant large-scale structure along the line of sight is visible in the 3D cone diagram, whose impact on lensing mass reconstruction will have to be carefully evaluated.

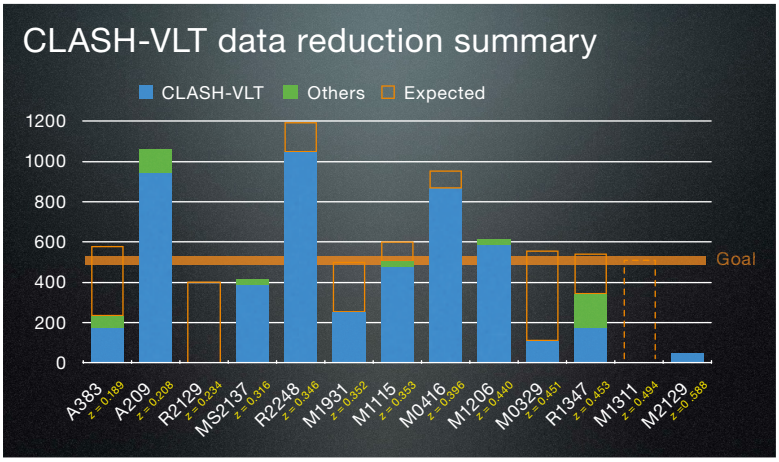

Figure 1. The number of spectroscopically confirmed cluster members for each target of the CLASH-VLT Large Programme is shown. The small fraction of redshifts from the literature is shown in green and the orange histograms indicate the expected number of members from data still under reduction, extrapolating from the measured success rate. Observations for MACSJ1311-0310 are still ongoing. Observations for MACSJ2129-0741 were suspended due to significant Galactic cirrus contamination.

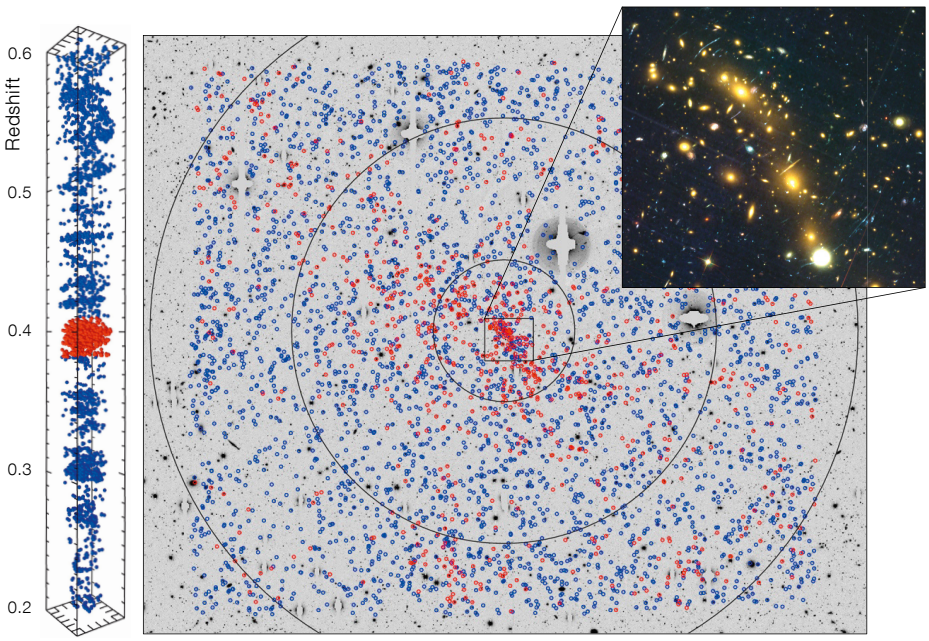

Figure 2. Spatial distribution of galaxies with reliable redshifts on a Subaru/Sup-Cam R-band field of MACSJ0416.1-2403 (29 by 25 arcminutes). Red symbols indicate 880 cluster members confirmed to date (galaxies with restframe velocities within ± 3000 km s^{-1} from the median z of 0.396), blue symbols are the other 3307 galaxies over the z range 0.02–4.15. Large circles with 1, 3, 5 Mpc radii centred on the northern brightest cluster galaxy (BCG) are indicated. The HST image (ACS-WFC3 colour composite) is a magnified view of the core (2 by 1.8 arcminutes). To the left, the corresponding 3D distribution in redshift space (only over the redshift range 0.2–0.6) is shown.

Matter distribution

By combining such a large spectroscopic dataset with the HST Treasury data, deep multicolour wide-field imaging and existing Chandra/XMM data, CLASH-VLT was designed to produce a major advance in our ability to measure DM and baryonic mass profiles over the radial range of 10 kpc to ~ 5 Mpc by combining lensing, dynamical and X-ray methods. An example of such an accurate determination of the mass density profiles from different probes is shown in Figure 3 for MACSJ1206.2-0847 (see Biviano et al., 2013 for details). Note the excellent agreement between the dynamical mass

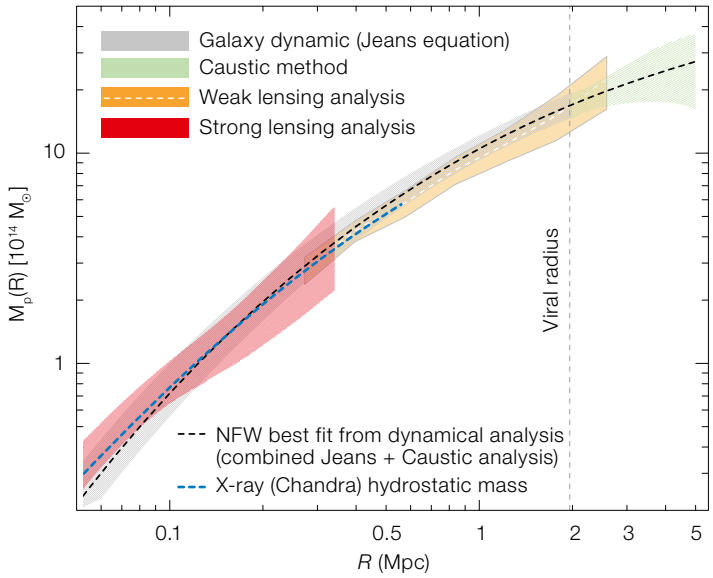

Figure 3. Projected mass density profiles of MACSJ1206.2-0847 at z = 0.44 obtained from dynamical analysis from CLASH-VLT data (from Biviano et al., 2013), compared with those from strong lensing (Zitrin et al., 2012), weak lensing (Umetsu et al., 2012) and Chandra X-ray data. The overall agreement is very good despite completely independent data and methodologies. The kinematical analysis allows the mass to be measured out to 5 Mpc (~ 15 arcminutes), corresponding to 2.5 times the virial radius.

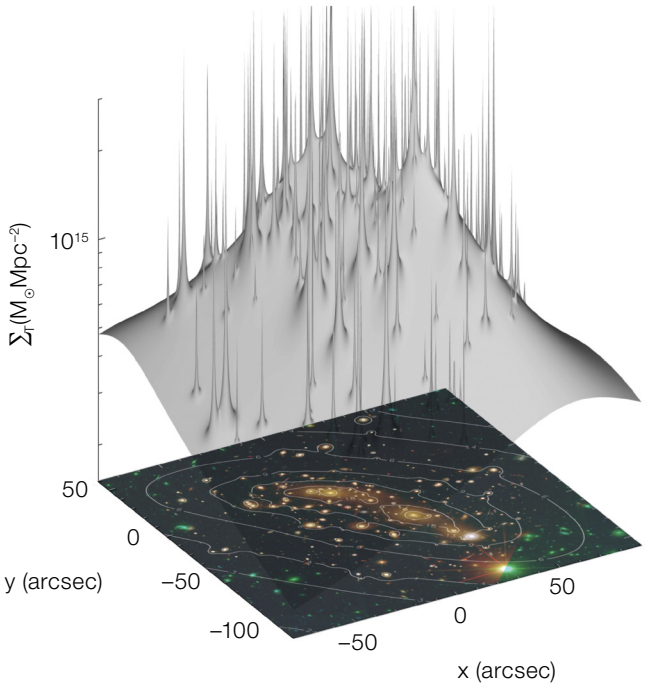

Figure 4. The total surface mass density distribution in the inner regions of MACSJ0416.1-2403 reconstructed from the best-fitting strong lensing model. It is based on spectroscopy of ten multiply imaged systems and over 100 spectroscopic members in the cluster core. The two extended dark matter halos, and many sub-halos corresponding to cluster members, are visible in the overlaid iso-mass contour map (from Grillo et al., 2014).

and other measurements, although completely independent data and methodologies are used. This shows that a number of systematic uncertainties inherent in these methods are well under control in this case.

The overall shape of the mass profile is found to be in very good agreement with cosmological ΛCDM simulations. However, by subtracting the baryonic contributions (stars + gas) and extending the analysis to the inner core (radius < 50 kpc), a DM profile significantly flatter compared to DM-only simulations is found. The reason for this tension with ΛCDM structure formation scenarios is currently not fully understood. It might well be due to dynamical effects of the baryons near the cluster centre of the DM distribution. Alternatively, it might be caused by a non-negligible self-interaction cross-section of DM particles which can make the core "puffier". A careful mass reconstruction of the cores of the entire CLASH sample should shed more light on this important issue. Also note in Figure 3 that by using the caustic method (Diaferio & Geller, 1997), where the escape velocity of galaxies is measured from the distribution of restframe radial velocities at varying radii, the cluster mass estimate can be extended well beyond the virial radius.

In Sartoris et al. (2014), we have shown that this accurate determination of the kinematics and lensing mass profiles can be used to directly confirm the pressureless assumption for the DM equation of state. This test exploits an effect of general relativity for which photons (lensing) and galaxies (kinematics) behave differently as test particles of the gravitational potential, whose shape depends on both density and pressure profiles.

One can anticipate that such accurately determined cluster masses for the full sample of CLASH clusters will be very useful to calibrate scaling relations. These are used to estimate cluster masses from other proxies (e.g., X-ray observables, galaxy velocity dispersions, luminosities) for the upcoming new generation of large cluster surveys for cosmological applications (e.g., Dark Energy Survey [DES], eROSITA and Euclid space missions).

The availability of large redshift catalogues in cluster fields significantly improves lensing-based reconstructions of the cluster mass distribution. For example, to obtain an unbiased estimate of the weak lensing shear map, it is crucial to isolate a pure sample of background galaxies. For this aim, spectroscopic redshifts are needed to calibrate photometric redshifts or colour selection criteria. In addition, strong lensing modelling, and hence an accurate determination of the mass distribution in cluster cores, heavily relies on the redshift measurement for a large number of multiple images and arcs over the widest redshift range. It is also very important to have a large sample of spectroscopic members in order to achieve an unbiased accounting of galaxy-sized halos. This was demonstrated in the detailed modelling of the inner mass distribution of MACSJ0416.1-2403 (see Figure 4 and Grillo et al., 2014). From this high-resolution mass map, we can measure for the first time the sub-halo mass function, i.e., characterise the inner structure of large DM halos, and compare it with cosmological simulations.

Lensed and high-*z* galaxies

With exposure times ranging between 2 and 6 hours, we have secured redshifts for the main multiply imaged lensed systems in each cluster, which is a key input for strong lensing models. Models and magnification maps using a subsample of these redshifts have been made publicly available, as part of the CLASH survey ancillary data products. A diagram summarising this effort is shown in Figure 5, which gives the magnitude–redshift distribution of lensed sources with measured redshift to date. Galaxies with Ly-α in emission as faint as 26 AB magnitude have been identified.

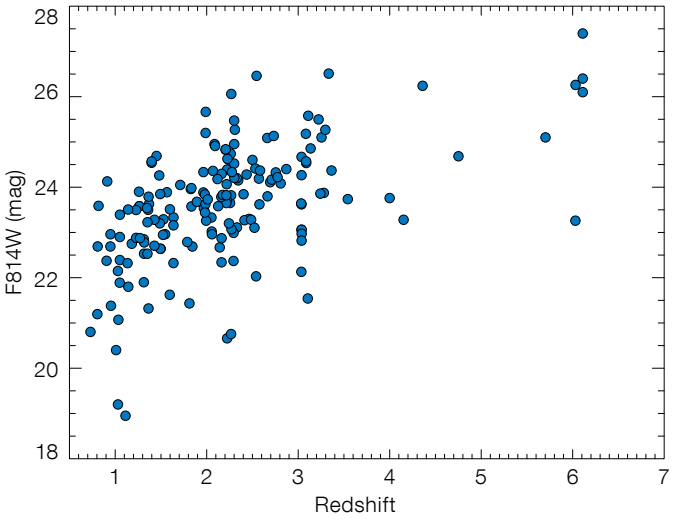

Figure 5. Magnitude–redshift distribution of the spectroscopically confirmed lensed galaxies obtained so far from the CLASH-VLT programme (184 redshifts corresponding to approximately 80% of the final sample).

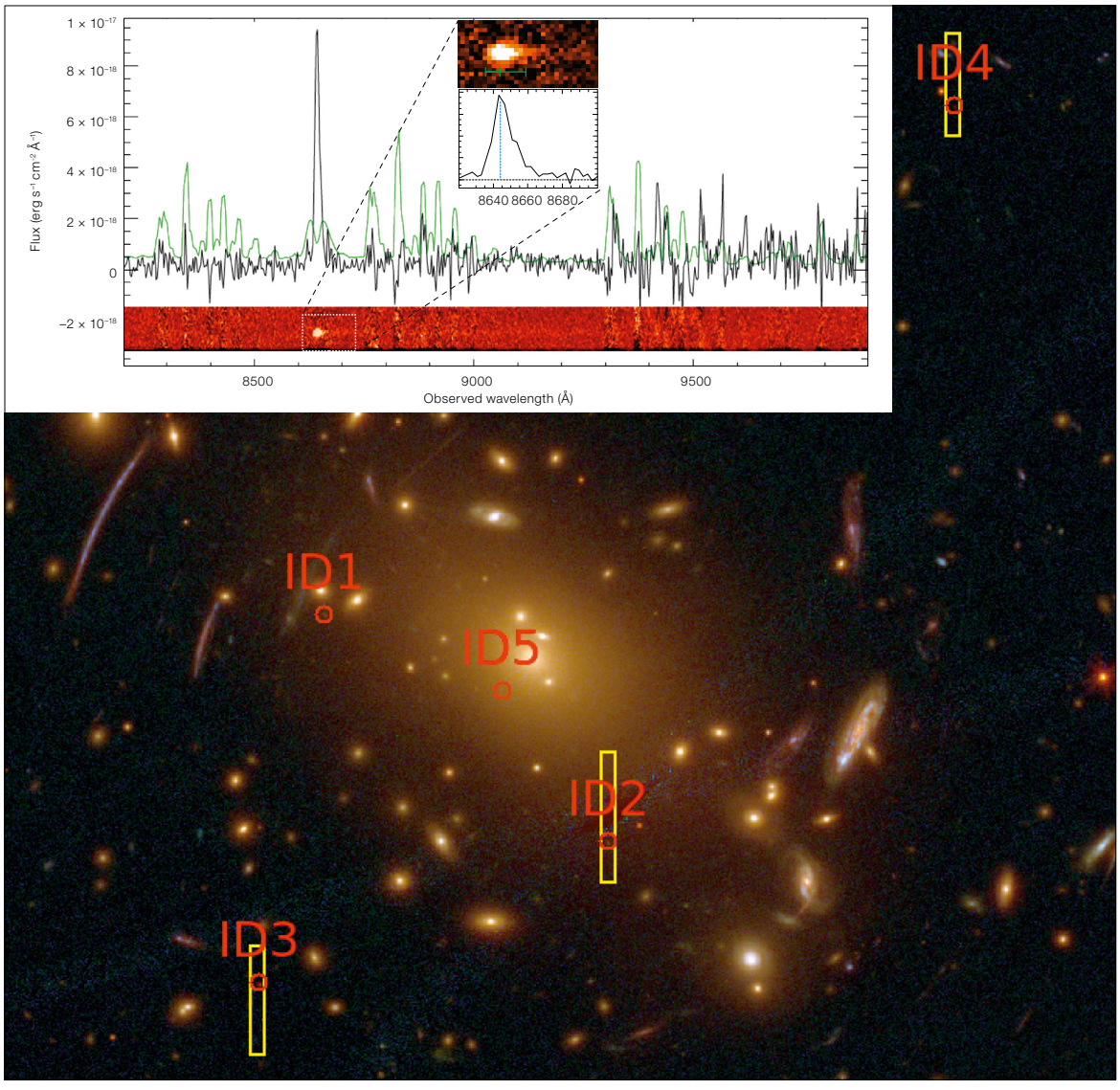

Figure 6. The quintuply lensed galaxy at $z = 6.11$ in the cluster RXC J2248.7-4431 (from Balestra et al., 2013; see also Monna et al., 2014). The image is an HST colour composite and the five locations of the lensed galaxy are shown as ID1–5. The inset shows a spectrum of ID3 (F814 AB mag = 26.1) obtained with VIMOS + MR grism, with 2 hours integration. The Ly-α line has a flux of 1.6×10^{-16} erg cm^{-2} s^{-1}, and a continuum signal is also clearly detected.

The most distant example is part of the quintuply lensed galaxy at z = 6.11 in the cluster RXC J2248.7-4431 (Balestra et al., 2013 [see Figure 6]; Monna et al., 2014). After correcting for magnification (μ ~ 6), modelling of the spectrophotometric properties suggests that this is a young (< 300 Myr), compact, sub L^* galaxy with little dust content and a star formation rate of ~ 10 $M_\odot$/yr. Since the magnification typically ranges between 3 and 10 in CLASH clusters, one can probe sub-L^* systems at z ~ 6–9, in a complementary fashion to field studies which are sensitive to $L \gtrsim L^*$ galaxies. This faint galaxy population is thought to play an important role in reionising the Universe, owing to its relatively high space density and possibly high escape fraction of ionising radiation.

Prospects

The final spectroscopic dataset from the CLASH-VLT survey will contain ~ 30 000 spectra and associated redshifts, of which ~ 7000 are cluster members. It is therefore easy to anticipate that the overall CLASH-VLT spectrophotometric database will have a broad legacy value in studies of the evolution and transformation of galaxies in a range of environments. A full characterisation of the underlying stellar populations of cluster galaxies and structural properties can be obtained from our homogeneous imaging data (HST in the core, Subaru on the entire cluster volume) and spectroscopic classification.

As an example, a snapshot of the spectral properties of the galaxy population in the MACSJ1206.2-0847 cluster is given in Figure 7. The stacked galaxy spectra in increasing radial bins show the typical gradient of the underlying stellar populations, from high to low density regions. The baryonic stellar content also includes the contribution from the intracluster light, which is clearly visible in both the Subaru and HST images. The exploitation of the CLASH-VLT dataset in this direction has just started (Presotto et al., 2014; Annunziatella et al., 2014; Kuchner et al., 2014).

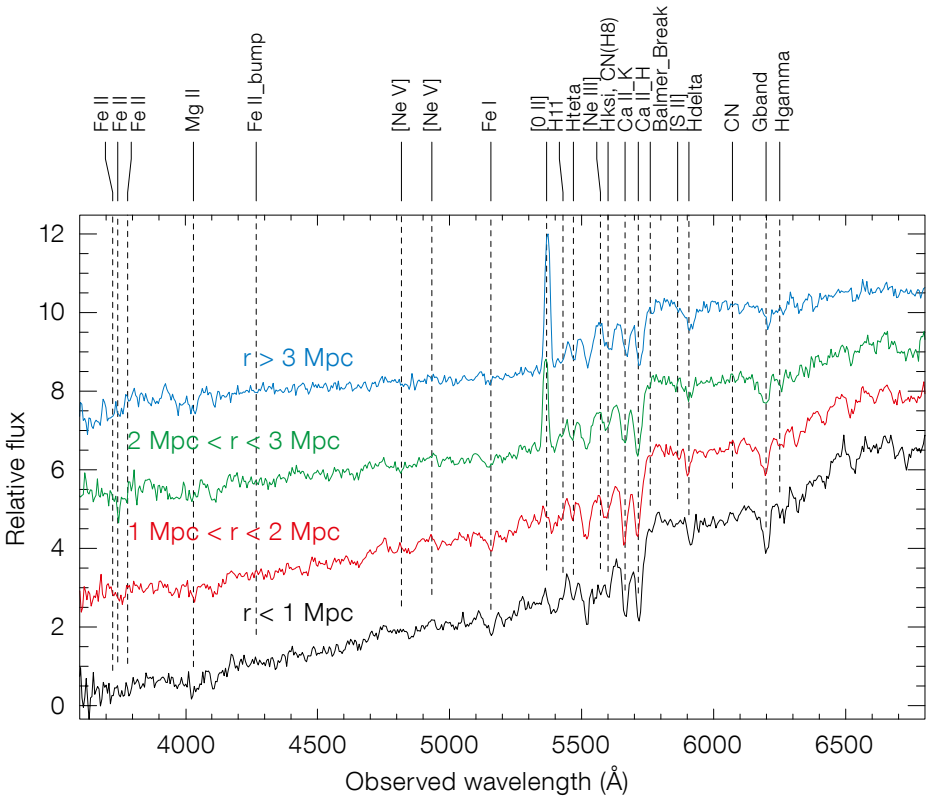

Figure 7. Co-added spectra of cluster galaxies in different radial bins of the cluster MACSJ1206.2-0847 (z = 0.44, ~ 70 spectra per bin), showing the typical stellar population gradient in clusters, from high densities in the core to low densities in the outskirts.

Updated information on the CLASH-VLT survey can be found at the public CLASH-VLT page[2], which includes a list of publications and the public release of a number of redshift catalogues including the MACSJ1206.2-0847 and two Frontier Field clusters. Redshift catalogues and spectra will gradually be ingested into the ESO advanced data products archive, similar to some other LPs. This will facilitate the scientific exploitation well beyond the envelope envisaged in the original proposal and consolidate its legacy for the future.

Acknowledgements

We acknowledge the continuous help of the ESO User Support Department for the implementation of this LP. We especially thank our project support astronomer, Vincenzo Mainieri, for his excellent support and advice.

References

Annunziatella, M. et al. 2014, A&A, 571, 80
Balestra, I. et al. 2013, A&A, 559, 9
Biviano, A. et al. 2013, A&A, 558, 1
Bouwens, R. et al. 2014, ApJ, 795, 126
Coe, D. et al. 2013, ApJ, 762, 32
Diaferio, A. & Geller, M. J. 1997, ApJ, 481, 633
Grillo, C. et al. 2014, ApJ, submitted, arXiv:1407.7866
Jouvel, S. et al. 2014, A&A, 562, 86
Kuchner, U. et al. 2014, Procs. of IAU Symp. 309, Vienna, arXiv:1409.4999
Merten, J. et al. 2014, ApJ, in press, arXiv:1404.1376
Monna, A. 2014, MNRAS, 438, 1417
Postman, M. et al. 2012, ApJS, 199, 25
Presotto, V. et al. 2014, A&A, 565, 126
Sartoris, B. et al. 2014, ApJ, 783, 11
Umetsu, K. et al. 2012, ApJ, 755, 56
Zitrin, A. et al. 2012, ApJ, 749, 97

Links

[1] CLASH page at STScI: http://www.stsci.edu/~postman/CLASH/
[2] Public CLASH-VLT page: https://sites.google.com/site/vltclashpublic/home

Open House day at ESO Headquarters was held this year on 11 October 2014, together with many other institutes on the Garching research campus. The doors were open for seven hours and about 3300 people visited, including many children, some of whom are shown here listening to a story of the Space Rock Pedro in the ESO library. Details can be found in Picture of the Week for 20 October 2014.

The set of three temporary office buildings at the Headquarters site were removed during November 2014. The vacated area is allocated for the site of the ESO Supernova Planetarium & Visitor Centre, for which construction will begin early next year. See Picture of the Week for 10 November 2014.

ESO/Luis Calçada

Report on the Workshop

Resolved and Unresolved Stellar PopUlaTIoNs (RASPUTIN)

held at ESO Headquarters, Garching, Germany, 13–17 October 2014

Giuseppe Bono[1]
Elena Valenti[2]

[1] Dipartimento di Fisica, Università degli Studi di Roma-Tor Vergata, Italy
[2] ESO

The workshop aimed at sharing and discussing observations and diagnostics, together with models and simulations, of the resolved and unresolved stellar populations in galaxies from the Milky Way to the distant Universe. Special attention was paid to recent results concerning galaxy formation and evolution, fostering the exchange of ideas and techniques in dealing with nearby stellar populations. There will be no published proceedings, but presentations are available for download from the workshop web page (www.eso.org/sci/meetings/2014/rasputin2014).

Stellar populations are among the most important observables required to constrain galaxy formation and evolution. Quantitative analyses of the stellar content of stellar systems pave the way to converting the information carried by starlight into physical quantities, such as stellar masses, chemical abundances and star formation rates, and to trace back in time the evolution and chemical enrichment history of galaxies.

Historically, stellar population studies have followed two parallel paths. Observations and analyses of individual stars belonging to **resolved** stellar populations have enabled us to understand the fundamental physics of stellar evolution, through a detailed comparison between theory (isochrones, luminosity functions) and observations (photometry, spectroscopy); a path that has also allowed us to reconstruct the star formation history of the Milky Way and nearby Local Group galaxies. Secondly, knowledge of the evolutionary properties of nearby stellar populations has, in turn, helped to constrain the nature of **unresolved** stellar populations and galaxy evolution back to the dawn of time.

Strangely enough, despite their tight connection, the resolved and the unresolved approaches have made progress almost independently, with a marginal overlap between the two communities. We felt that the time was ripe for a new synergy between these two communities. The advent of the latest generation of ground- and space-based telescopes has had a profound impact on the field of stellar populations. For instance, multiple populations have been recently observed in globular clusters, which used to be considered as the template for simple stellar populations (same age, same chemical composition). On the other hand, secondary kinematic features have been recently discovered in nearby dwarf spheroidal galaxies, which used to be considered relaxed stellar systems, indicating that they experienced multiple star formation events with no evidence of rotation.

Moreover, the wealth of information on the metallicity (α-, *r*- and *s*-elements, CNO) and kinematics of thousands of stars in the Milky Way are enabling us to compare our own Galaxy with external systems, thus providing a unique opportunity for understanding the mechanisms of galaxy evolution. Finally, unresolved studies of nearby and high-redshift objects can now provide unprecedented constraints on resolved stellar population studies, as clearly indicated by the recent claims of a non-universal initial mass function (IMF) in external galaxies.

Thus, with the era of the Extremely Large Telescopes (ELTs) approaching, it is more important than ever to ensure that both resolved and unresolved stellar population studies share similar ingredients, compare and validate homogeneously their specific tools. The workshop was therefore organised with the goal of reviewing the state of the art in both fields, as well as in the framework of future ELT facilities, and to foster synergies between the two stellar communities.

More than a hundred participants from Europe, North and South America and Asia gathered for the RASPUTIN meeting held at ESO Headquarters. The five-day workshop featured 63 talks, 18 of which were invited reviews, and two panel discussions. Additionally, on the second and the fourth days of the meeting, we held poster pop-up sessions, giving a chance to those who had applied for a poster to present their most important results in five minutes (37 poster presentations). The formula was broadly appreciated, and it fostered very lively discussions, both among the younger and the more senior researchers.

Science sessions

Forty-five contributed talks were selected by the Scientific Organising Committee (SOC), out of a pool of nearly a hundred proposals received during workshop registration. The selected talks, as well as the invited reviews, covered quite large research areas, from star formation in the nearby Universe, stellar populations (observations and theory) in the Galaxy and in the Local Universe, to stellar populations in late-type galaxies and into the European Extremely Large Telescope (E-ELT) era. In order to promote and develop new collaborations, the exchange of ideas and plans between the two communities, the talks in the different sessions were intentionally mixed, rather than scheduled according to their research topic.

In the following paragraphs, we only mention the content of relatively few contributions. The summary mirrors our opinions and attitudes. We urge the reader to check the remaining presentations posted on the web page of the meeting[1].

A review talk on the Galactic Bulge (by M. Zoccali) summarised the latest results in this field. A very complex picture is emerging of its stellar populations from detailed spectroscopic and photometric observation. The Bulge of the Milky Way is a boxy/peanut structure, traced by red clump stars. However, several independent observations suggest the presence of two stellar components: the oldest ($\gtrsim$ 10 Gyr) and metal-poor component, traced by RR Lyrae stars, is a spheroidal component; whereas the younger (8–10 Gyr) metal-rich component, traced by red clump stars, is a boxy/peanut bar. The presence of a significantly younger component (1–6 Gyr), as suggested by the spectroscopic campaign of microlensed dwarfs, is still an open question. The presence in the outer Bulge of a metallicity gradient

following the boxy/peanut structure, but with lack of significant evidence for this metallicity gradient in the inner Bulge, represents a real challenge for dynamical models.

Additional results on the Galactic Bulge stellar population were presented in several other talks, such as the first detection of the white dwarf cooling sequence (A. Calamida), the largest photometric infrared database collected through the ESO Public Survey VISTA Variables in the *Via Lactea* (VVV; talk by D. Minniti), and the cylindrical rotation confirmed by the recent spectroscopic survey — the GIRAFFE Inner Bulge Survey (GIBS: presentation by E. Valenti).

Preliminary results of the Gaia–ESO survey on the iron and α-element distribution across the Galactic spheroid (Halo, thick and thin Disc) were also widely discussed. In particular the role which the different approaches to data reduction and analysis play in constraining the systematics affecting individual abundance measurements, was discussed. Interestingly enough, we also discussed the role which the sociology of large collaborations plays in planning and running large surveys (G. Gilmore).

The properties of the stellar component in the innermost Galactic region (within ~ 300 pc of the Centre) were reviewed by N. Matsunaga, using variable stars, in particular Cepheids, as tracers. In this context, infrared spectra represent a unique diagnostic for studying the kinematics and chemical content of this hidden population in the Galaxy. Since they are good distance indicators and tracers of old and young populations, different types of variables stars can be used to construct 3D maps and the star formation history of various Galactic structures. As a tracer of old stellar populations, RR Lyrae variables have also been used to explore and discuss the role of ultra-faint dwarf spheroidal galaxies in the formation of the Galactic Halo (G. Fiorentino). The comparison of RR Lyrae properties in the Halo and in dwarf galaxies suggests that — under very extreme assumptions — no more than 50 % of the Halo population can be made from dwarfs. Additionally, it has been suggested that high-amplitude, short-period, fundamental RR Lyrae stars could represent a powerful tool with which to constrain the metallicity of the old stellar population in much more distant galaxies.

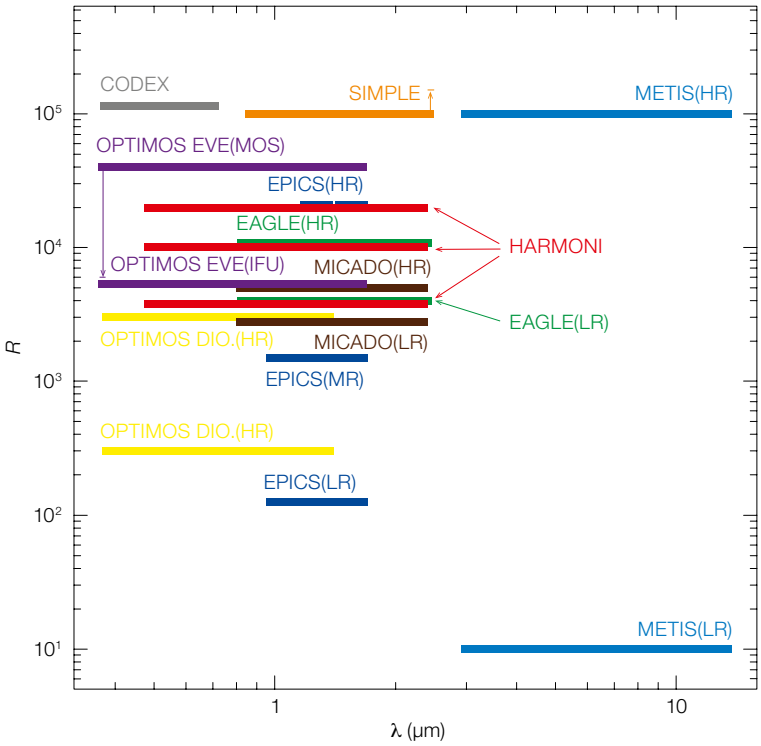

Figure 1. Spectral resolution and wavelength coverage of the proposed/planned new instrumentation at E-ELT.

Finally, a nice example of the tight interplay between the study of resolved and unresolved stellar populations was shown by E. D’Alessandro’s results on the ultraviolet colours of Galactic and extragalactic globular clusters. He presented a new approach to the analysis of the horizontal branch (HB) stars in globular clusters, based on a detailed comparison between the observed and synthetic HB, which takes into account the strong impact of the He content in shaping the HB of old stellar populations. By using a combination of Hubble Space Telescope (HST) ultraviolet (UV) and the GALaxy Evolution eXplorer (GALEX) data, they have observed a general correlation between the UV colours of globular clusters and the mass of the host galaxies: the UV colours of the globulars get bluer with increasing host galaxy mass.

There were extensive reviews of the different aspects of the spectroscopic diagnostics of giants and supergiants, including advances of atomic data, model atmospheres and synthetic spectra, as well as their consequences for the science of Galactic and extragalactic observations. In particular, the impact which non-local thermodynamic equilibrium effects have in providing precise heavy element abundances was discussed (M. Bergemann). We also discussed the potential of the planned instruments at the E-ELT (see Figure 1) to provide different stellar information with a new generations of models, such as the quality of chemical abundances in stars.

The metallicity of red supergiants can be obtained from quantitative spectroscopy down to a resolution of ~ 3000 in the *J*-band, where several α-elements (Ti, Mg, Si) and Fe lines can be used for abundance analysis (see Figure 2). Red supergiants, the brightest stars at infrared wavelengths, are therefore the ideal targets for measuring the metallicity of star-forming galaxies out to 7–10 Mpc and up to ten times further by observing the integrated light of unresolved super star-clusters. By using the *K*-band Multi

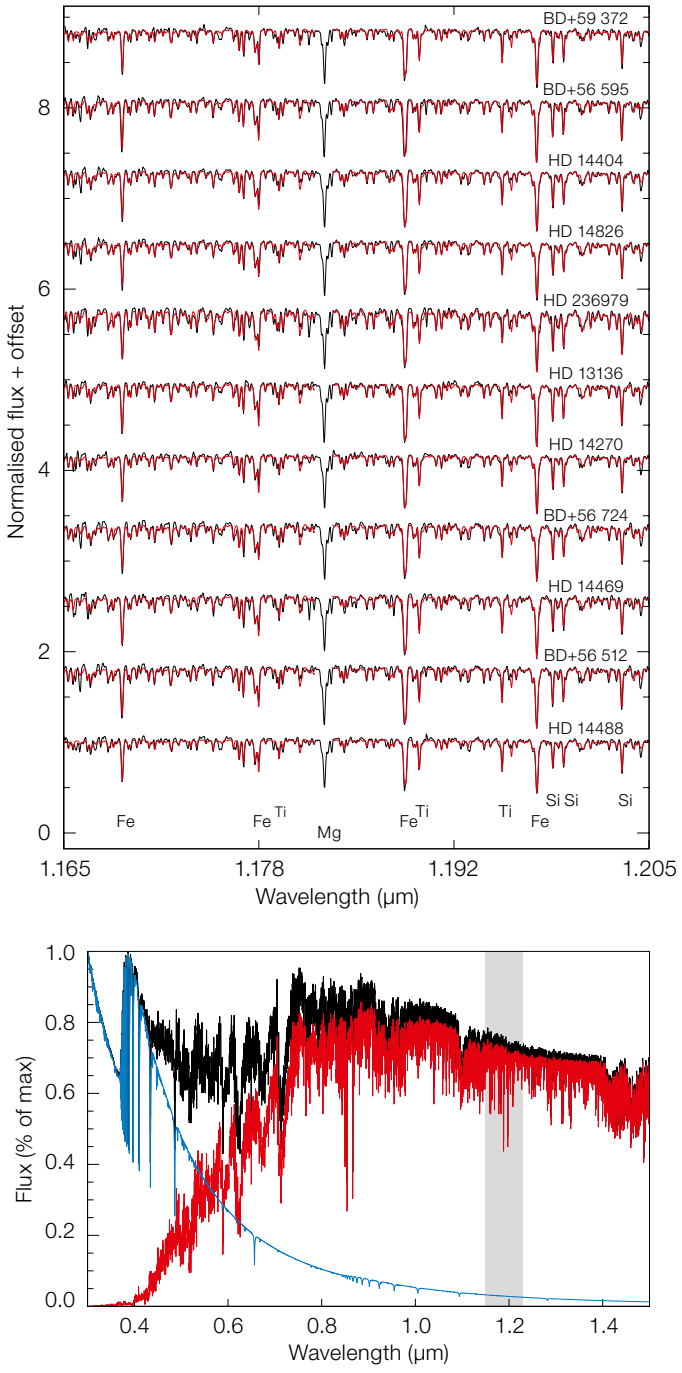

Figure 2. Upper: Spectral library of red supergiants observed at high resolution and then degraded to R = 3000. The main diagnostic atomic lines are labelled. Red lines refer to the best fitting non-local thermodynamic equilibrium models (Gazak et al., 2014a).

Lower: Theoretical spectra for a $10^5\ M_\odot$ super star-cluster after 15 Myr. The spectrum representing the full super star-cluster spectral energy distribution is shown in black, the main sequence and blue supergiants stars in blue, and the flux due to red supergiant members is plotted in red. The grey shaded region represents the J-band (Gazak et al., 2014b).

Object Spectrograph (KMOS) at the Very Large Telescope (VLT) with only a modest amount of time, it is now possible to probe the cosmic chemical evolution in a substantial volume of the local Universe containing hundreds of star-forming galaxies, with the ultimate goal of providing a robust measurement of the mass–metallicity relation for low-redshift galaxies (B. Davies). Low-resolution multi-object optical spectroscopy of individual blue supergiants can also be used in order to constrain the metallicity content in galaxies out to a distance of 8 Mpc, as shown by R. P. Kudritzki.

M. Monelli introduced the astrophysical and cosmological role of nearby dwarf galaxies. The presentation focussed on star formation history in early, late and transition dwarf galaxies in the nearby Universe and their correlation with the total mass. The role which accurate and deep colour–magnitude diagrams play in constraining the age and metallicity distribution of the different populations was also discussed, together with detailed elemental abundances (talks by K. Venn and M. Fabrizio).

Recent developments and findings concerning chemo-dynamical models were broadly reviewed by I. Minchev, with particular emphasis on the role played by stellar migrations and chemo-kinematic relations in constraining disc formation models. The theoretical framework for modelling galaxies, both from the analytical and numerical point of view, was thoroughly presented by J. Binney and L. Mayer. The discussion was focussed on the dynamical modelling of the different galactic components, as well as on the cosmological simulations of isolated dwarf galaxies. Special attention was paid to the implications of core formation on the early evolution of dwarf spheroidals.

Panel discussions

During the first and the third day of the meeting, we had two panel discussions, respectively focussed on Theory and Simulations (chair: R. P. Kudritzki), and Observations and Synergies between VLT and E-ELT (chairs: B. Leibundgut and J. Liske).

The panel discussion on theory and observations was considered a good chance to discuss future developments in the ongoing effort to improve the predictive power of simulations and models currently available in the literature. The discussion touched on several pending issues in the current theoretical framework. In particular, we discussed the limits in microphysics (molecular opacities, gravitational settling, radiative levitation) and in macrophysics (turbulent mixing, mass loss) affecting stellar interior models (M. Salaris, S. degl'Innocenti, P. G. Prada Moroni). We also considered the present limitations of the stellar atmospheric models, e.g., the impact that non-local thermodynamic equilibrium effects have on heavy element abundances

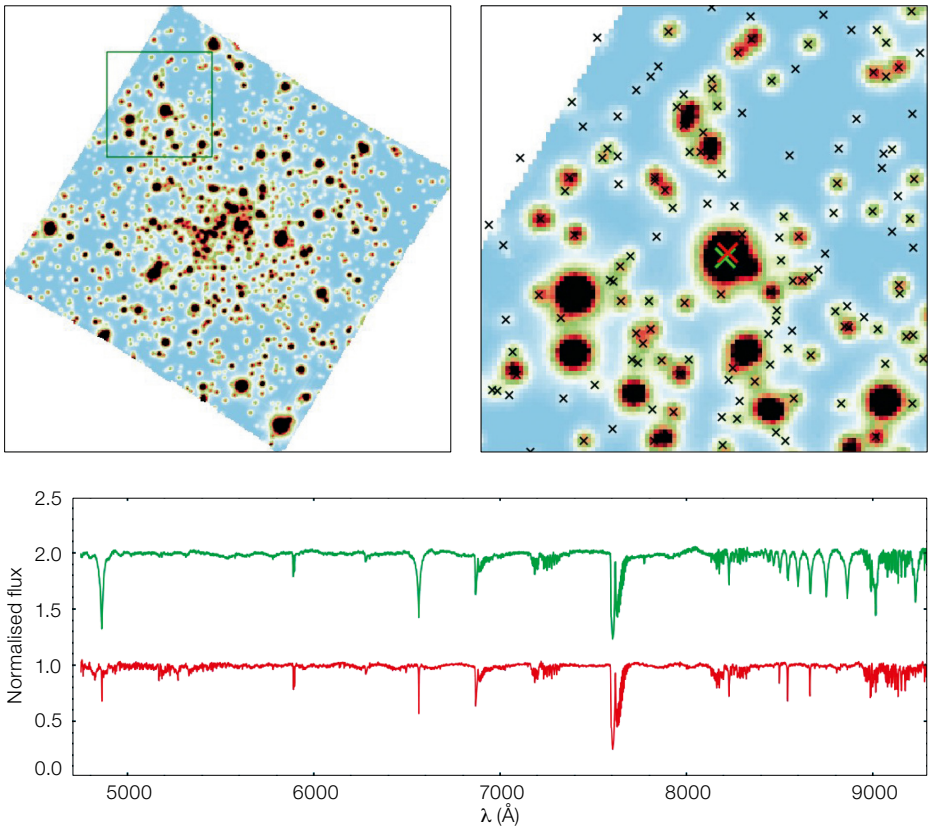

Figure 3. Observations of the central 1 by 1 arcminute region of the globular cluster NGC 6397 taken with MUSE (upper left panel); the area within the green box is shown enlarged in the upper right panel. The spectra of the two blended stars marked with red and green crosses in the upper right panel were successfully extracted using the new algorithm PampelMuse (Kamann et al., 2013). The algorithm has been specifically designed to optimise the deblending and extraction of spectra in very crowded fields by applying point spread function fitting techniques to integral field unit data.

(M. Bergemann). Moreover, we had a thorough discussion about the current limitations in handling molecular opacities (F. Alard), and its impact on late-type stars.

Furthermore, a wide-ranging debate was also devoted to optical and near-infrared (NIR) spectroscopy, and in particular, to the accuracy and precision of CNO, α-, *s*- and *r*-element abundances in the two different regimes (B. Davies, L. Origlia). The discussion concentrated also on the pros and cons of integrated spectroscopy when dealing with abundances of specific elements (Na, Mg, Fe). Participants stressed the key role that new algorithms, using synthetic and spectral libraries, are playing in modelling integrated spectra (R. Schiavon). The same outcome applies to chemo-dynamical models (I Minchev, S. de Riijcke) and to cosmological simulations (L. Mayer).

The panel discussion on observations and synergies between the VLT and the E-ELT touched on many topics. B. Leibundgut introduced the current status and the near future developments of the instrumentation available at the VLT, while J. Liske talked about the first generation of instruments planned for the E-ELT. These introductions were considered as a preamble to a discussion about the instrumentation (imaging and spectroscopy) — either available or planned — for the VLT and the E-ELT. The debate focussed on the instrumentation that is paving the road for the E-ELT. Contributors stressed the key role that low (KMOS), intermediate (X-shooter) and high spectral resolution (CRIRES) spectrographs are playing, with regard to the spectrographs planned for the E-ELT (integral field spectrograph [E-ELT-IFS], high resolution spectrograph [E-ELT-HIRES] and multi-object spectrograph [E-ELT-MOS]). The same considerations apply to NIR imaging instruments (HAWK-I and ERIS) with regard to the NIR camera for the E-ELT (MICADO).

The outcome of the discussion was that the instrumentation currently available at the VLT is much more than a stepping stone to the future. The treatment of data collected with integral field spectrographs does require new insight, not only for the quantity of spectra we are dealing with, but mainly for the algorithms adopted to perform the accurate astrometry and optimal spectral extraction of individual sources — even in very crowded environments (S. Kamann, see Figure 3). Indeed, these instruments play a strategic role, since they provide a suitable playground for training the ESO community. It was also mentioned that the currently available wide-field imagers and optical surveys might not cover the entire parameter space of the target selection for E-ELT (J. Cepa). Finally, there was a thorough analysis of the crucial role that the module(s) of adaptive optics will play for the first-light instruments (M. Tosi).

Acknowledgements

The organisation of this workshop would not have been possible without the very dedicated help of Stella Chasiotis-Klingner, Laura Inno, Anja Feldmeier and Samantha Milligan (the Local Organising Committee). We thank the Scientific Organising Committee chairs and members for their work and relevant contribution, the ESO students Suryashee Aniyan, Florian Niederhofer, Marco De Pascale and Yue Zhang and the ESO IT team for their support during the five days of the workshop. Special thanks go to Eric Siml who, despite all the ongoing activities connected with the ESO Open House Day, ensured that the final logistical arrangements went very easily and smoothly. Finally we are grateful to all participants who travelled to Garching and shared their exciting results.

References

Gazak, J. Z. et al. 2014a, ApJ, 787, 142
Gazak, J. Z. et al. 2014b, ApJ, 788, 58
Kamann, S., Wisotzki, L. & Roth, M. M. 2013, A&A, 549, A71

Links

[1] Workshop web page with contributions: http://http://www.eso.org/sci/meetings/2014/raputin2014/program.html

Jorge Melnick Retires from ESO

Claus Madsen[1]

[1] ESO

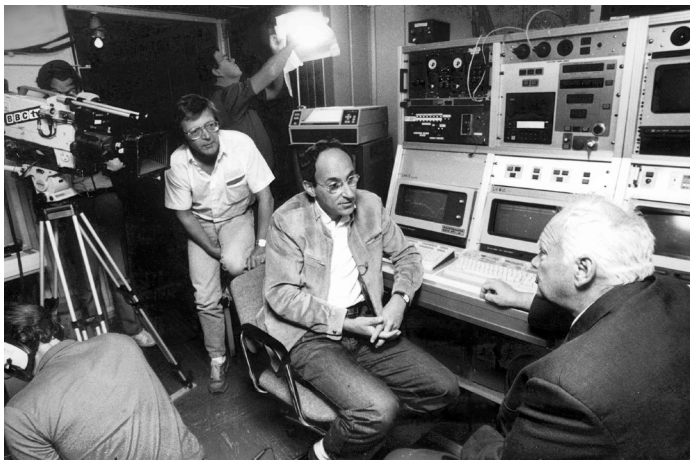

Figure 1. Jorge Melnick (left) being interviewed by Patrick Moore for the BBC Television series *The Sky at Night* in the control room of the ESO Coudé Auxiliary Telescope (CAT) in 1989.

J. I. Duk

Figure 2. Jorge Melnick among colleagues during a farewell meal at La Silla in October 2014.

One of the strongest features of ESO is its organisational framework. This allows it to undertake the long-term planning and implementation of resource-intensive projects. Another is its ability to attract and retain highly qualified staff from all corners of the world; people who are not simply among the best within their respective fields, but who are often able to think outside the box. It is not unreasonable to say that this applies to Jorge Melnick, who retired from ESO on 1 September 2014. Some might even say that Jorge is someone who would only fit into his own, very special box.

Born on 6 August 1946, he studied physics at the University of Chile, before moving on to Caltech, where he was awarded a PhD in 1976. His scientific interests have included general relativity, the astrophysics of starbursts and clusters of galaxies. He has published more than 120 papers in refereed journals.

Jorge joined ESO in 1977 as an ESO Fellow and he was a member of the science group that had just been established at the initiative of ESO's third Director General, Lodewijk Woltjer. "It was a fantastic atmosphere," he recalled. "It was a small group. Everyday, Woltjer would go from office to office to pick us up for lunch!" This was still at a time when the photographic plate was the main detector, and as part of his assignment, Jorge became responsible for the "measuring machines", the Optronics and the PDS photodensitometers located at the ESO offices in Geneva. In 1980, he returned to Chile, only to come back to ESO in 1984, first as an associate and, from 1988, as Head of the Astronomy Department, and member of the La Silla management team. Six years later, he became Director of the observatory. This was the heyday of La Silla, with its full complement of telescopes, including the 3.5-metre New Technology Telescope (NTT) and the 15-metre Swedish ESO Submillimetre Telescope (SEST), in full use. In those days, La Silla was Europe's Southern Observatory.

But rather than resting on his laurels, Jorge began a rigorous campaign to streamline and improve operations, comprising a reorganisation of the observatory, refurbishment of the telescope park and improving staff relations. If anything, the proof of these efforts was in the pudding: in 1998, the year of the first light for the VLT, La Silla had the largest science output of any observatory in the world. That year was also the beginning of the second, challenging phase of Jorge's directorship: managing the future of an observatory that would no longer be at the centre of attention and growth, as this enviable position moved to the Paranal Observatory. This change meant coping with shrinking budgets and staff reductions, while keeping up staff morale and the efficient running of the facility. Among the initiatives he took was to create the La Silla University, to allow for the fast training of new staff (many of whom would move elsewhere) and in general to create an inspiring and creative atmosphere to motivate people. Another initiative was to achieve ISO 9001 certification for the observatory; probably the only time that an observatory has done this anywhere.

Jorge's ability to think outside the box was convincingly put to good use and, thus, it was, with a clearly ticked "job done" box, that he ended his directorship in 2004, as La Silla and Paranal merged to become one observatory. Jorge moved on to become VLT Programme Scientist, while also playing an important role in the installation of the APEX antenna on Llano de Chajnantor. He continues at ESO as an astronomer emeritus and is also a Visiting Scientist at the Observatorio Nacional in Rio de Janeiro. We look forward to his continued contributions to our science and, as a great emeritus ambassador for our organisation.

Fellows at ESO

Maud Galametz

I grew up in the north of France (a region often covered by a rain cloud on the French weather forecast maps). At school, I was interested in many different subjects, from art history to classical literature, from biology to physics. I think I really started to consider being a researcher in science at the end of high school. In France, science undergraduates have two choices, either going to university or entering an engineering school, and I decided for the latter. I entered the National School of Physics of Strasbourg in 2004. While I learned about signal treatment, optics, programming or automation, I realised that it was fundamental physics that I preferred the most. I chose that specialisation for my last year and also followed the masters' programme in astrophysics at the Observatory of Strasbourg in parallel to my engineering studies. I obtained my two diplomas in 2007.

I worked on my first independent research project during my masters' thesis (on cosmic rays as potential source of contamination for the LISA mission) at Imperial College London. London has been my favourite city ever since. I then started a PhD thesis in October 2007 on nearby galaxies in the Nuclear Research Centre of Saclay (close to Paris), working with Dr S. Madden. Nearby galaxies have always fascinated me. They offer an interesting variety of physical conditions and are close enough to allow resolved and complex analysis of their star formation processes. I worked in particular on dwarf galaxies, objects that resemble primordial galaxies in terms of metal enrichment, and studied their cold dust properties using far-infrared and submillimetre observations.

This wavelength range was booming during my PhD because of the advent of new instruments and space telescopes such as the Herschel Space Observatory. Herschel was launched in 2009, during the second year of my PhD, and my host institute was deeply involved in the construction of one of the onboard instruments. I will always remember the excitement of the Saclay teams after the successful launch, and the craziness of the following year while we were analysing the first data. I started my first postdoc at the Institute of Astronomy of Cambridge in November 2010, working with Prof. R. Kennicutt. There, I could not only expand my studies of dust properties to a larger sample of galaxies, but also learned tremendously from my colleagues in fields other than my own during these definitely too short three years.

Maud Galametz

I left Cambridge about a year ago to start my current ESO Fellowship in Garching. The Fellowship allows us to carry out independent research on a scientifically stimulating campus, but it also provides opportunities to take functional responsibilities on the various observing sites of ESO. I chose to be an observer at the APEX antenna. I have used many of the APEX instruments for my research, so my duties are in fact directly related to my science. I have been going to APEX three times a year so far, and enjoy it very much. APEX is like a small family. Through discussions with the astronomers and operators, I am learning a lot about carrying out service mode observations for a world-class telescope, as well as dealing with more specific technical issues.

I enjoy astrophysics because of the scales involved. It is about drawing a global picture, understanding the general physical laws that govern the Universe we live in. New facilities are built on the ground or sent into space every year (despite the dramatic financial cuts that our field has to deal with) to deepen our understanding of galaxy characteristics and get a handle on their past and current history. Astronomy is also one of the scientific domains that fascinate the general public the most (especially the younger audience) and this is always very rewarding. A colleague of mine once said that he felt his computer screen was like a spaceship that allows him to travel through space. That is also how I see astronomy: a way of travelling through time, seeking the unknown beyond our own tiny blue marble.

André Müller

My passion and interest for astronomy and space travel started early. I grew up in Plauen, a small town located in the south of Saxony, Germany. During regular barbecues in summer I would wonder what I was seeing when the stars and the Milky Way became visible at night. Later, when I took physics and astronomy in school, I decided to buy a 114-millimetre Newtonian telescope from a department store, which incidentally ate up all my savings. But discovering our Solar System, clusters of stars, and other galaxies visually was quite rewarding and satisfying — until I needed to have a bigger telescope. I simply couldn't stop! I was in love with my new hobby. I became an active amateur astronomer and participated in a lot of astrophotography and poor man's spectroscopy while still accumulating lots of equipment. Not surprisingly, when it became time to choose a career path I enrolled at the University of Jena to study physics, before I moved to the Max Planck Institute for Astronomy in Heidelberg for my Diploma and PhD.

There I focussed on the exciting search for extrasolar planets around young stars using the radial velocity technique. This is a challenging task because the periodic signal of a potential planet can be well hidden in the data as stellar activity such as mass accretion and stellar spots can mimic a planetary signal. But finding such systems is important in order to set limits on the formation and migration timescales. As this technique requires a large time series of observations on many

potential target stars, I was able to visit La Silla Observatory many times throughout my studies.

During the course of my PhD thesis I additionally spent two years at ESO in Garching working for the PRIMA facility, which was undergoing its commissioning phase at the VLT Interferometer. I worked especially on a new observing mode for the MID-infrared Interferometric instrument (MIDI), where one of the two PRIMA fringe sensor units (FSU) are used to stabilise the interferometric *N*-band signal in MIDI. This observing mode pushes the sensitivity limits of MIDI down by at least a factor of five and allows for simultaneous visibility measurements in *K*- and *N*-bands.

My studentship at ESO Garching included the possibility of visiting Paranal Observatory and working directly with the impressive facility of VLTI. With all the hands-on experience I had gained during the course of my PhD thesis I decided to apply for an ESO Fellowship in Chile in order to regularly work with and operate one of the largest and modern telescopes in the world at the Paranal Observatory. As part of my duties at the observatory, I have supported operations and observations at the VLTI over the last two years. As a MIDI Fellow I have been able to dig deep inside the instrument with respect to hardware and software, while also commissioning the new MIDI + FSU observing mode and characterising it. At the VLTI we mainly use the 1.8-metre Auxiliary Telescopes because they allow us a flexible configuration, as their positions can be adjusted. However, my favourite is still when I have the opportunity to combine the light received by all four 8.2-metre Unit Telescopes. Those are some of the most thrilling moments for me.

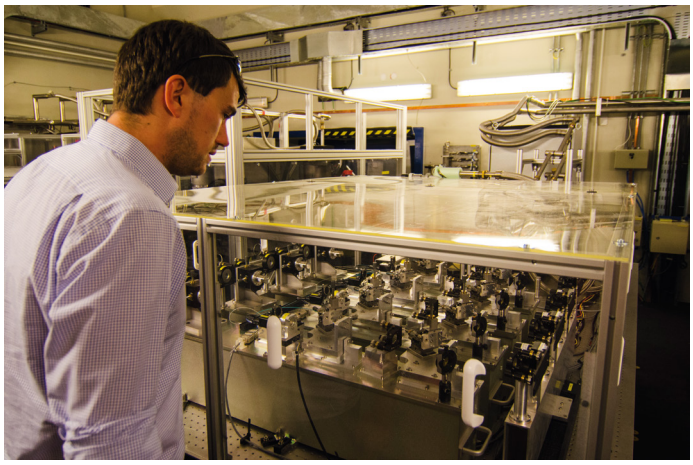

André Müller

When I leave Paranal for my next position next summer, I will remember my time in one of the driest places on Earth, yet only 12 kilometres away from the largest ocean, with gratitude. It is this juxtaposition mixed with the clear night sky of the Atacama which have made my Fellowship here at ESO Chile a truly remarkable experience.

External Fellows at ESO

In addition to the ESO Fellowships, a number of external fellows are hosted at ESO. A profile of one of the current Marie Curie Fellows is presented.

Kate Maguire

I grew up in Dublin, Ireland and had decided from a young age I wanted to be either the president of the United States or an astronaut (perhaps both — I can't quite remember). The first dream was dashed when my Mum told me you couldn't be president of the US unless you're an American citizen, and the second when I found out that they prefer to send medical doctors or fighter pilots into space. Neither of which seemed appealing to me as I had always been fascinated with science.

When applying to universities I couldn't make up my mind which science subject interested me most. Therefore, I chose to study Science at University College Dublin to obtain a broad scientific knowledge. After two years, I decided that I was most interested in physics and chose a major in experimental physics. While I really enjoyed the course and the physics topics it covered, it also involved spending a lot of time in the lab twiddling knobs and adjusting dials.

If that had been my only experience with physics research I think my research career might have ended there. However, during the third year of my undergrad, one of my lecturers offered the class the thrilling prospect to spend a summer working as an intern at NASA Goddard. I applied and was selected — it was this experience that completely changed my opinion of research. During this amazing

summer, I got to experience, first hand, a really exciting scientific working environment at NASA, visit the instrument testing facilities, as well as work on new data from the Solar and Heliospheric Observatory (SOHO), looking at the formation of active regions on the Sun. I discovered that I really enjoyed doing astrophysics research and that this was what I wanted to do as a career.

I began a PhD in Astrophysics in 2007 at Queen's University Belfast under the supervision of Stephen Smartt, working on understanding the properties of core-collapse supernovae. This gave me many great opportunities to travel, to observe at telescopes, and attend conferences around the world. During the first year of my PhD, I got my first chance to observe at the William Herschel Telescope in La Palma. Despite not having great weather, I was immediately hooked by the excitement and thrill of observing at a telescope.

After I finished my PhD in 2010, I took up a postdoc position at the University of Oxford. I continued my work on supernovae, changing fields slightly to focus on Type Ia supernovae and their use as cosmological distance indicators. I worked as part of the Palomar Transient Factory, one of the leading astronomical transient discovery surveys operating at the Palomar Observatory. This came with all the excitement and strange working hours you might expect, when you do research in a field as unpredictable as exploding stars.

Kate Maguire

Oxford was an amazing place to work and a beautiful city. However, at the end of three years, I was ready to move on to the next adventure. I was delighted when I found out that my Marie Curie Intra-European Fellowship application had been successful and I would be moving to work at ESO, Garching.

I started at ESO in October 2013 and from day one, I've loved it here. My research focusses on understanding the stars that explode as Type Ia supernovae and how we can improve the supernova samples obtained with future cosmology missions. ESO is a really special place to work, with its vibrant international staff, loads of interesting talks and events to attend, and the broad range of astrophysical and technical expertise on hand. It has given me great insight into the workings of a world-leading observatory. I'm also fortunate to collaborate with some great researchers working in the field of supernovae at ESO and on the Garching campus. I am looking forward to making the most out of my remaining two years here in Munich and then who knows where my next adventure will take me.

ESO/José Joaquín Pérez

Star trails across the 15-metre dish of the now decommissioned Swedish ESO Submillimetre Telescope (SEST) at La Silla. The SEST was the first submillimetre telescope operated by ESO, from 1987 until 2003. See Picture of the Week for 22 September 2014.

Personnel Movements

Arrivals (1 October–31 December 2014)

Europe	
Kerzendorf, Wolfgang (DE)	Fellow
Molina, Conde Antonio Ignacio (ES)	Electronics Engineer
Noirot, Gaël (FR)	Student
Popping, Gergely (NL)	Fellow
Schulz, Christine (DE)	Student

Chile	
Colleoni, Franco (CL)	Electronic Engineer
Haubois, Xavier (FR)	Fellow
Kaminski, Tomasz (PL)	Fellow
Sedaghati, Elyar (IR)	Student
Stephan, Christian (DE)	System Engineer

Departures (1 October–31 December 2014))

Europe	
Beller, Angelika (DE)	Administrative Assistant
Block, Roland (DE)	Head of HR Department
Dekker, Klaas Johannes (NL)	Instrumentation Physicist
Fedrigo, Enrico (IT)	Software Engineer
Inno, Laura (IT)	Student
Niederhofer, Florian (DE)	Student
Pontoni, Cristian (IT)	Mechanical Engineer
Rodrigues, Myriam (PT)	Fellow
Saulder, Christoph (AT)	Student
Turolla, Stefano (IT)	Software Engineer
Yan, Fei (CN)	Student

Chile	
Diener, Catrina (CH)	Student
Elliott, Paul (GB)	Student
Kabath, Petr (CZ)	Op. Staff Astronomer
Krogager, Jens-Kristian (DK)	Student
Rengaswamy, Sridharan (IN)	VLTI Astronomer
Schuller, Frédéric (FR)	Head of Science APEX
Segovia, Alex (CL)	Software Engineer
Villarroel, Cristian (CL)	Electromechanical Technician
Weilenmann, Ueli (CH)	Deputy Director

Confirmation of *The Messenger* Subscription

We are currently updating our subscriber database for the printed edition of *The Messenger*. If you wish to continue receiving a hard copy, and have not yet confirmed your subscription, please read further.

On the label of the envelope in which you received this edition, you will find a unique web link, written in the format http://eso.org/m/MMMM. Please type this link into a browser and tick the box "Subscribe to receive the ESO Messenger" if you wish to continue receiving the printed version. By pressing the "Submit" button, you will then continue to receive the print version of *The Messenger*. If you wish to check your postal address, click on "Update your profile". *The Messenger* is always available on the ESO web[1].

This is the last chance to confirm your *Messenger* postal subscription. If you do not confirm your subscription by 31 January 2015, we assume that you no longer wish to receive *The Messenger* in print form.

In case you do not currently have internet access, please inform us of your desire to continue with the printed subscription, by letter to:
The Editor
The Messenger
European Southern Observatory
Karl Schwarzschild Straße 2
85748 Garching bei München
Germany

Links

[1] The Messenger: http://www.eso.org/sci/publications/messenger/

ESO, the European Southern Observatory, is the foremost intergovernmental astronomy organisation in Europe. It is supported by 15 countries: Austria, Belgium, Brazil, the Czech Republic, Denmark, France, Finland, Germany, Italy, the Netherlands, Portugal, Spain, Sweden, Switzerland and the United Kingdom. ESO's programme is focused on the design, construction and operation of powerful ground-based observing facilities. ESO operates three observatories in Chile: at La Silla, at Paranal, site of the Very Large Telescope, and at Llano de Chajnantor. ESO is the European partner in the Atacama Large Millimeter/submillimeter Array (ALMA) under construction at Chajnantor. Currently ESO is engaged in the design of the European Extremely Large Telescope.

The Messenger is published, in hardcopy and electronic form, four times a year: in March, June, September and December. ESO produces and distributes a wide variety of media connected to its activities. For further information, including postal subscription to The Messenger, contact the ESO education and Public Outreach Department at the following address:

ESO Headquarters
Karl-Schwarzschild-Straße 2
85748 Garching bei München
Germany
Phone +49 89 320 06-0
information@eso.org

The Messenger:
Editor: Jeremy R. Walsh;
Design, Production: Jutta Boxheimer;
Layout, Typesetting: Mafalda Martins;
Graphics: Lorenzo Benassi.
www.eso.org/messenger/

Printed by G. Peschke Druckerei GmbH,
Taxetstraße 4,
85599 Parsdorf, Germany

ISSN 0722-6691

Contents

Important notice:
Please confirm your subscription!
See page 63

Front-cover: The protoplanetary disc around the pre-main sequence star HL Tauri observed by the Atacama Millimeter/submillimeter Array (ALMA) during the long baseline testing campaign. The image of the dust continuum emission at 1.28 millimetres was obtained using baselines up to 15 kilometres in length; the synthesised beam full width at half maximum is about 35 milliarcseconds (the dusty disc is about 180 au in diameter, corresponding to a major axis full width of approximately 1.3 arcseconds). This classical T Tauri star is situated in the Taurus star-forming complex at 140 pc from the Sun.

Although HL Tau had been extensively observed with radio and millimetre/submillimetre facilities, the complexity of the dust structures in the protoplanetary disk is revealed for the first time by this detailed image. The apparent gaps in the dust emission in the disc may be caused by young planets opening gaps in the disc or by the efficient trapping of millimetre-sized grains by much smaller pressure disturbances in the radial profile of the gas disc, attributable to a variety of physical mechanisms. The ALMA Science Verification dataset for HL Tau will be released on the ALMA Science Portal as soon as fully validated. See Release eso1436 for some more details. Credit: ALMA (ESO/NAOJ/NRAO)